AN INTEGRATIVE APPROACH TO UNDERSTANDING PI(3)P SIGNALING AND AUTOPHAGY

By

Katie Renee Martin

A DISSERTATION

Submitted to
Michigan State University
in partial fulfillment of the requirements
for the degree of

DOCTOR OF PHILOSOPHY

Cell and Molecular Biology

2011

ABSTRACT

AN INTEGRATIVE APPROACH TO UNDERSTANDING PI(3)P SIGNALING AND AUTOPHAGY

By

Katie Renee Martin

Phosphatidylinositol-3-phosphate (PI(3)P) is an intracellular signaling lipid which recruits lipid-binding proteins, tethering them to subcellular compartments where they function (Gaullier, Simonsen et al. 1998). PI(3)P is required for proper endocytosis and autophagy, two membrane trafficking processes pivotal to cellular homeostasis, and as such, its production, maintenance, and turnover must be tightly controlled (Funderburk, Wang et al. 2010). PI(3)P is produced by the class III member of the mammalian phosphoinositide-3-kinase (PI3K) family, Vps34 (vacuolar protein sorting 34) (Funderburk, Wang et al. 2010). Vps34-PI(3)P signaling is antagonized by PI(3)P lipid phosphatases, such as MTMR3 and MTMR14 (hJumpy), which function in autophagy (Vergne, Roberts et al. 2009; Taguchi-Atarashi, Hamasaki et al. 2010). Given the complexity of Vps34 function and the number of proteins essential for its function, we hypothesized that additional protein phosphatases exist to regulate Vps34-PI(3)P signaling.

To investigate this hypothesis, we performed a cell-based RNA interference screen to identify phosphatases whose loss of function alters cellular PI(3)P . We found that reduced expression of a receptor-like protein tyrosine phosphatase, PTPsigma, increased the abundance of PI(3)P-positive vesicles in cells. Intriguingly, the vesicles in these cells mimicked those observed in autophagic cells. Using a variety of cell biology approaches, we confirmed that PI(3)P signaling and autophagy are elevated in the absence of PTPsigma.

As a role for PTPsigma in PI(3)P signaling was unprecedented, much work was required, and still remains, to fully characterize its function in this process. We uncovered that PTPsigma

resides on PI(3)P-positive vesicles during both basal and induced autophagy. Further, its internalization from the cell surface and presence on these vesicles is likely controlled through defined proteolytic processing. Finally, loss of PTPsigma in cells appears to promote Vps34 activity as measured <italic>in vitro</italic> and PTPsigma is capable of interacting with both Vps34 and at least one of its binding partners, Rubicon. We propose a working model where PTPsigma downregulates PI(3)P signaling through control of a phosphotyrosine substrate, yet to be identified, within or closely related to an endocytic Rubicon-containing Vps34 complex. These results are summarized in Chapter 2.

Although still elusive, the function of PTPsigma in PI(3)P signaling and autophagy may prove to have important consequences for cell fate. Autophagy is essential for cell survival during stress and accordingly, we would predict PTPsigma suppression to enhance autophagy-mediated survival (Meijer and Codogno 2004). The ability to increase autophagy could potentially provide therapeutic benefit in the treatment of several diseases, notably those involving neurodegeneration (Hara, Nakamura et al. 2006; Komatsu, Waguri et al. 2006). With this in mind, we utilized an <italic>in silico</italic> screening approach, outlined in Chapter 3, to identify small molecule inhibitors of PTPsigma. If selective, these compounds could prove to be useful molecular probes in the study of autophagy.

Finally, we aimed to capture a comprehensive understanding of autophagy dynamics through mathematical modeling. To this end, we utilized kinetic live-cell microscopy to develop an accurate and predictive model of autophagy vesicle dynamics, detailed in Chapter 4. This model, and its framework for a more large-scale autophagy network, can be used to generate novel hypotheses and be implemented as a tool to test experimentally-derived hypotheses, such as those presented for PTPsigma.

ACKNOWLEDGEMENTS

First, I thank my mentor, Dr. Jeff MacKeigan, for his guidance, encouragement, and support during the course of my graduate studies. He has believed in me and my abilities unconditionally, even during times when I was unsure of myself. The confidence he has instilled in me and the enthusiasm for science he has fostered will remain with me through my future endeavors.

Second, I want to thank my lab-mates for making my time in graduate school enjoyable on a daily basis. Each person that has passed through the lab, whether for a few weeks or years, has impacted me personally and had a positive influence on my project. I extend an especially heartfelt thank-you to my fellow graduate students in the lab – the future Drs. Natalie Niemi, Laura Westrate, Jon Karnes, Megan Goodall, and Dani Burgenske. Together, we have shared both the frustrations and joys of lab life and helped each day pass a bit easier with laughter. I will take with me fond memories of our tissue culture room pow-wows, lunches, cardboard cut-out heists, carbohydrate buffer, iPod Fridays, retreats, British accents, midnights in the lab, and many other experiences. I also thank the rest of my lab-mates for their support and camaraderie - Dr. Brendan Looyenga (my bench-mate for nearly five years), Dr. Nate Lanning, Dr. Vanessa Fogg, Audra Kauffman, and Amy Nelson. I also express my gratitude for student interns who have helped with my project over the years – Joe Church, Ryan Davis, Michael Shaheen, James Hogan, and Anna Plantinga. And finally, I express a very special thank you to my limp-a-long, Dr. Jamie Kopper. We were inseparable from our first days in graduate school, overcame the difficulties of classes and prelims together, and will continue to be friends throughout the rest of life's journeys.

I am also extremely grateful to the members of my guidance committee – Dr. Walt Esselman, Dr. Christina Chan, Dr. John LaPres, and Dr. Cindy Miranti. They have each provided critical insights into my project and supported its vision from the very beginning. Their kind, accommodating, and encouraging nature has made my graduate experience a positive one.

My project was entirely dependent on the expertise and effort of collaborators including Michel L. Tremblay, Yong Xu, H. Eric Xu, Richard Posner, William Hlavacek, Dipak Barua, Edward Stites, Nikolai Sinitsyn, Srabanti Chaudhury, Nathalie Meurice, Joachim Petit, and Pooja Narang. I thank them for their willingness to contribute to my project and for teaching me the value of collaboration.

Last and most importantly, I thank my family for their unwavering support. My mom, dad, grandparents, and siblings have accepted my career pursuits and offered encouragement every step of the way. The work ethic and character of each of my family members motivates and inspires me to do positive and constructive things with my life. Also, I would not be where I am today without the love and support of my husband, Steve Martin. He has been there for me every day, encouraged me when I needed it most, and serves as a constant reminder of what is truly important in life.

TABLE OF CONTENTS

LIST OF TABLES

LIST OF FIGURES

CHAPTER 1

Introduction

INTRODUCTION

Vps34 and phosphatidylinositol-3-phosphate (PI(3)P) signaling in Autophagy

Phosphoinositide-3-kinases (PI3Ks) comprise an important class of enzymes in cellular signaling responsible for generating 3'-phosphorylated phosphoinositides, a group of diverse lipid messengers. Mammalian PI3Ks are categorized into three classes - I, II, and III - based on sequence and function. The class I PI3Ks are comprised of 110 kDa catalytic subunits and regulatory subunits and function primarily in growth factor signaling through generation of $PI(3,4,5)P_3$. Class I PI3Ks are known to control cell survival, growth, and proliferation. As such, the catalytic p110 subunits have been found to be amplified and activated in a number of cancers, making these kinases the focus of intense research (Samuels, Wang et al. 2004; Manning and Cantley 2007). The class II PI3Ks are homomeric enzymes that are quite large multi-domain enzymes compared to class I PI3Ks. The class II PI3Ks enzyme function remains to be elucidated, despite the defining features of a lipid kinase catalytic domain and a defined C-terminal motif (Domin, Pages et al. 1997).

The class III PI3K family is represented by a single enzyme in mammals, hVps34 (encoded by the PIK3C3 gene), which selectively generates PI(3)P on intracellular membranes. This enzyme is considered the primordial PI3K as it is the only member found in yeast, where it was initially identified (Herman and Emr 1990; Schu, Takegawa et al. 1993). Mutant Vps34 strains were characterized by defects in vacuolar protein sorting (Vps) and subsequently, it was discovered that Vps34 harbors lipid kinase activity (Schu, Takegawa et al. 1993). Studies with Vps34 yeast mutants and knockdown in mammalian systems have determined that Vps34-catalyzed PI(3)P is critical for homotypic endosomal fusion, multivesicular body formation, protein sorting, and receptor recycling (Herman and Emr 1990; Stack, Herman et al. 1993; Simonsen, Lippe et al. 1998; Christoforidis, Miaczynska et al. 1999; Futter, Collinson et al. 2001). In support of these functions, a PI(3)P-specific lipid binding module, termed the FYVE domain, has been characterized and found within several effector proteins with known endocytic functions, for example, early endosomal autoantigen 1 (EEA1) (Gaullier, Simonsen et al. 1998).

Vps34 in Autophagy

Following establishment of Vps34 as a critical mediator of endocytosis, additional evidence ignited interest in Vps34 as an integral component of an additional cellular process, termed macroautophagy, which similarly involves dynamic membrane trafficking. Macroautophagy (henceforth, autophagy) is a catabolic process in which portions of the cytosol, including proteins and entire organelles, are encapsulated in double-membrane vesicles (autophagosomes) and subsequently delivered to the lysosome for degradation (Klionsky 2007). Sequestered material is broken down into basic biochemical building blocks, which are then recycled and reused by the cell as an energetically favorable alternative to *do novo* synthesis. Autophagy occurs constitutively in nearly all cells to maintain cellular homeostasis but is dramatically activated in response to cellular stress, namely, nutrient starvation, where it can function as a survival mechanism (Meijer and Codogno 2004).

Autophagy is executed in four stages: initiation, nucleation, maturation, and completion (Figure 1.1). Nutrients and growth signaling activate mTORC1 (mammalian target of rapamycin complex 1), the key controller of autophagy induction. While activating processes which contribute to cell growth, proliferation, and survival during times of low stress and high nutrient content, mTORC1 concurrently down regulates autophagy. This is accomplished through direct inhibitory phosphorylation of an autophagy-initiating complex, ULK1-mAtg13-FIP200 (Ganley, Lam du et al. 2009; Hosokawa, Hara et al. 2009; Jung, Jun et al. 2009). ULK1 (Unc-51-like kinase 1; the mammalian homolog of Atg1) is a serine/threonine kinase required for autophagy. Upon mTORC1 inhibition (i.e. during starvation), dephosphorylated ULK1 is liberated, and functions to permits the nucleation of an isolation membrane, or phagophore (Ganley, Lam du et al. 2009; Hosokawa, Hara et al. 2009; Jung, Jun et al. 2009). The synthesis of this cup-shaped double-membrane structure is promoted in large part by Vps34 and its catalysis of PI(3)P. PI(3)P decorates early autophagic membranes and serves as a subcellular tag, recruiting lipid-binding effectors, such as DCFP1 (double FYVE domain–containing protein 1), and WIPI1 and WIPI2 (WD repeat domain phosphoinositide-interacting proteins 1 and 2) in mammals (Proikas-Cezanne, Ruckerbauer et al. 2007; Axe, Walker et al. 2008; Polson, de Lartigue et al. 2010).Vps34 activity is required for the downstream activation of Atg9 cycling, a process whereby this transmembrane protein cycles from peripheral locations to the site of autophagosome synthesis, putatively bringing lipids or membranes with it to build the vesicle (Young, Chan et al. 2006; Webber and Tooze 2010).

Expansion of the phagophore and eventual closure into a mature autophagosome is executed by two ubiquitin-like conjugation systems. The first conjugation involves covalent binding of Atg12, a ubiquitin-like protein, to Atg5 and subsequent incorporation into a large oligomer with Atg16L at the phagophore (Mizushima, Noda et al. 1998). The second system involves the most well-known autophagy protein and classically used autophagosome-marker, LC3 (Atg8 in yeast), which after processing by the Atg4 protease, becomes covalently attached to phosphatidylethanolamine (PtdEns) on the autophagosome (Ichimura, Kirisako et al. 2000; Kabeya, Mizushima et al. 2000; Kirisako, Ichimura et al. 2000). The location and allowance of

LC3 conjugation to the autophagosome is controlled by Atg5-Atg12-Atg16L, which functions as an E3-like enzyme (Fujita, Itoh et al. 2008). The completion of this process is marked by the fusion of the autophagosome directly with a lysosome (generating an autolysosome), or more frequently, with an endosome destined for the lysosome (generating an amphisome), and eventual degradation of sequestered cargo (Dunn 1990; Berg, Fengsrud et al. 1998; Klionsky 2007).

Vps34 was identified as part of the autophagic machinery in a study discovering that the mechanism of action of the autophagy inhibitor, 3-methyladenine (3MA), was through selective inhibition of class III PI3K activity (Petiot, Ogier-Denis et al. 2000). The 3MA-induced autophagy blockade was rescued by feeding cells with synthetic PI(3)P, demonstrating the importance of this lipid product in autophagy (Petiot, Ogier-Denis et al. 2000). In the years since this observation, several key findings have validated a role for PI(3)P in autophagy: *a)* autophagy is ablated in mutant Vps34 yeast strains and in cells from higher eukaryotes lacking Vps34 (Kihara, Noda et al. 2001; Juhasz, Hill et al. 2008), *b)* PI(3)P localizes to autophagic membranes (Juhasz, Hill et al. 2008; Obara, Noda et al. 2008), and *c)* several autophagy proteins (notably, Atg18) have been shown to bind PI(3)P (Proikas-Cezanne, Ruckerbauer et al. 2007; Axe, Walker et al. 2008; Polson, de Lartigue et al. 2010). Further, defined complexes of Vps34 and its binding partners have been shown to function in early autophagy (Sun, Fan et al. 2008; Matsunaga, Saitoh et al. 2009; Zhong, Wang et al. 2009). While these advances have highlighted an absolute requirement for PI(3)P in autophagy, little is known about the exact function PI(3)P serves in autophagy nor its complex regulation.

Subcellular Complexes of Vps34

In sum, it is apparent that Vps34 serves several distinct roles in cellular functions. This context specificity is controlled, at least in part, by the compartmentalization of Vps34 into several distinct complexes. In yeast, Vps34 resides in two defined complexes: complex I which regulates autophagy and complex II which functions in vacuolar protein sorting (Funderburk, Wang et al. 2010). While both share a common core of Vps34, Vps15, and Atg6, the protein sorting complex includes Vps38 and the autophagic complex includes Atg14 (Funderburk, Wang et al. 2010).

In mammals, Vps34 similarly exists in two or more complexes but its association with binding partners appears to be far more complex. The mammalian Vps34 core complex contains Vps34, Vps15 (p150), and Beclin1 (coiled-coil myosin-like BCL2-interacting protein; Atg6 homolog). This core is recruited to nascent autophagic membranes via an interaction with Atg14L (Barkor), the functional ortholog of yeast Atg14 (Sun, Fan et al. 2008; Matsunaga, Saitoh et al. 2009; Zhong, Wang et al. 2009). Atg14L has a novel hydrophobic motif, termed BATS (Barkor/Atg14L autophagosome targeting sequence), which directly binds to PI(3)P-positive membranes and contributes to the tethering of this subcomplex to the phagophore (Fan, Nassiri et al. 2011). Expression of Atg14L is stabilized by Beclin1, to which it directly binds, and together, they positively influence Vps34 kinase activity (Zhong, Wang et al. 2009). The origin of autophagosomal membranes is debated; however, growing evidence supports the existence of “omegasomes”, cup-shaped platforms which support the assembly of autophagosome machinery (Axe, Walker et al. 2008). Analysis by 3D-electron tomography has shown that these omegasome structures are cradled by portions of rough endoplasmic reticulum (ER) and contribute to the nucleation and dispersal of autophagosomes (Hayashi-Nishino, Fujita et al. 2009). An elegant live-cell microscopy-based investigation of the PI(3)P-binding protein, DFCP1, and its intriguing starvation-responsive ER localization led to this discovery (Axe, Walker et al. 2008).

In addition to the Atg14L-containing complex, a mutually exclusive Vps34 complex resides on endocytic compartments and is distinguished by the inclusion of UVRAG (UV radiation resistance-associated gene protein; homolog to yeast Vps38), which competes with Atg14L for binding to Beclin1 (Funderburk, Wang et al. 2010) . This complex, more abundant than the Atg14L complex, has been reported to promote the maturation of both endosomes and autophagosomes, although its exact contributions to these two processes is again debated (Liang, Feng et al. 2006; Itakura, Kishi et al. 2008; Matsunaga, Saitoh et al. 2009; Zhong, Wang et al. 2009). Mechanistically, UVRAG functions in several ways. On the most fundamental level, it promotes the catalytic activity of Vps34 (Liang, Feng et al. 2006). Secondly, UVRAG interacts with the class C-VPS/HOPS complex (via the Vps16 subunit), a guanine nucleotide exchange factor (GEF) for the late endosomal GTPase, Rab7 (Liang, Feng et al. 2006; Liang, Lee et al. 2008). This interaction stimulates activity of the complex, leading to GTP-loading of Rab7, and enhanced endosomal maturation (Liang, Lee et al. 2008).

The Vps34-UVRAG complex can associate with an additional regulator, Rubicon (RUN-domain protein as Beclin1-interacting and cysteine-rich containing). Recently discovered in two independent screens for Beclin1-interactors, Rubicon exists only in higher eukaryotes and uniquely, functions as an inhibitor of endocytic and autophagic maturation (Matsunaga, Saitoh et al. 2009; Zhong, Wang et al. 2009). Rubicon-mediated inhibition is achieved through two mechanisms: the direct binding and suppression of Vps34 activity and the competitive sequestration of UVRAG from C-VPS/HOPS. A direct interaction of Rubicon’s RUN domain with the kinase domain of Vps34 was recently described and found to suppress PI(3)P production (Sun, Zhang et al. 2011). In addition, Rubicon depletion enhances UVRAG binding to C-VPS/HOPS, facilitates Rab7 activity, and increases endocytic maturation (Sun, Westphal et al. 2010). Interestingly, a feed-forward loop was revealed whereby activated Rab7 sequesters Rubicon from UVRAG, thus liberating UVRAG to continually engage C-VPS/HOPS, and promote further loading of GTP to Rab7 (Sun, Westphal et al. 2010).

In addition to the control of Vps34 function conferred by the existence of unique subcomplexes, it is also plausible that phosphatases, which antagonize Vps34-catalyzed PI(3)P production, aid in the exquisite control of cellular PI(3)P and its specific cellular functions (Zeng, Overmeyer et al. 2006). This latter concept is the focus of the research presented here.

Protein tyrosine phosphatase receptor-type sigma (PTPsigma/PTPRS)

It has been estimated that 30% of the human proteome is subject to phosphorylation (Tautz, Pellecchia et al. 2006). Phosphorylation is a post-translational modification balanced by the actions of kinases, which catalyze the addition of phosphate moieties to specific amino acids, and phosphatases, which catalyze their removal (Tautz, Pellecchia et al. 2006). Tyrosine phosphorylation accounts for less than 0.1% of the total phosphorylation in mammalian cells; however, it represents a critical regulatory mechanism in signal transduction (Tautz, Pellecchia et al. 2006). By actively controlling the level of phosphorylation in cells, protein tyrosine phosphatases (PTPs) serve fundamental roles in signal transduction, making them vital to most cellular programs.

Of the 107 human PTPs, 38 members comprise the classic PTP family and exhibit strict specificity for tyrosine residues (Andersen, Mortensen et al. 2001). A subtype of this family includes the dual-domain receptor-like PTPs which express at the cell surface and contain two cytosolic active sites in tandem, termed D1 and D2 ((Andersen, Mortensen et al. 2001); Figure 1.2A)). The membrane-proximal D1 domains have robust catalytic activity, while the D2 domains are generally inactive. It has been postulated that the D2 domains may regulate the activity, stability, or substrate-specificity of the D1 domains (Barr, Ugochukwu et al. 2009). Three members of this subtype constitute the LAR family, including the ancestral LAR (*PTPRF*), PTPdelta (*PTPRD*), and PTPsigma (*PTPRS*). These three phosphatases are distinguished structurally, by their large ectodomains containing immunoglobulin and fibronectin repeats, and functionally, by their prominent role in homeostasis and neuronal development ((Andersen, Mortensen et al. 2001); Figure 1.2A)).

PTPsigma in Neurons and Development

An original role for the LAR family in neuronal function came from the discovery that expression of a *Drosophila* ortholog, DLAR, was required for the proper guidance of motor and photoreceptor axons as well as formation of synapses in flies (Krueger, Van Vactor et al. 1996). This finding instigated research and eventual confirmation of a similar function of vertebrate family members in nervous system development.

While it is apparent that LAR, PTPdelta, and PTPsigma all play important roles in neurons, they do so in both overlapping and distinct manners as evidenced in animal models targeting each of these genes. Mild abnormalities were observed in a murine model essentially lacking LAR expression (generated by gene trapping), including hippocampal and cholinergic defects (Yeo, Yang et al. 1997; Van Lieshout, Van der Heijden et al. 2001). Loss of PTPsigma or PTPdelta, however, resulted in more pronounced developmental defects. Over half of *Ptprd* $^{-/-}$ mice died within a few weeks of birth as a result of starvation, and those surviving to adulthood exhibited growth retardation and defects in learning and memory (Uetani, Kato et al. 2000). Sixty percent of *Ptprs*$^{-/-}$ mice died as neonates within two days of birth, and few survived longer than three weeks (Elchebly, Wagner et al. 1999; Wallace, Batt et al. 1999). Major abnormalities included neuroendocrine dysplasia, decreased brain size, structural irregularities of the central nervous system, growth retardation, wasting, spasms, and abnormal limb flexion (Elchebly, Wagner et al. 1999; Wallace, Batt et al. 1999). In addition to independent functions, PTPsigma and PTPdelta likely fulfill at least some complementary roles because deletion of both caused more pronounced developmental defects. All double *Ptprs*$^{-/-}$ / *Ptprd*$^{-/-}$ mice died immediately at birth, showing evidence of respiratory failure and paralysis (Uetani, Chagnon et al. 2006). This severe phenotype most likely stems from failed motor neuron targeting late in development (Uetani, Chagnon et al. 2006).

In support of its neuronal function, PTPsigma has been characterized as an important mediator of neurite outgrowth and axon guidance. In many contexts, PTPsigma has been shown to inhibit neurite outgrowth. First, *Ptprs*$^{-/-}$ mice showed enhanced nerve regeneration following injury in several models including sciatic nerve crush, optical nerve crush, and facial nerve crush (McLean, Batt et al. 2002; Thompson, Uetani et al. 2003; Sapieha, Duplan et al. 2005). Similarly, dorsal root ganglion neurons from *Ptprs*$^{-/-}$ mice exhibited enhanced outgrowth, an effect mediated by N-cadherin (Siu, Fladd et al. 2007). In agreement with this inhibitory role, it was shown that overexpression of PTPsigma could suppress neurite outgrowth in primary sensory neurons (Faux, Hawadle et al. 2007; Siu, Fladd et al. 2007). Most recently, it was reported that loss of PTPsigma promotes nerve regeneration following spinal cord injury (SCI) and that the interaction of the ectodomain of PTPsigma with chondroitin sulfate proteoglycans

(CSPGs) released at the site of injury, normally inhibits this process (Shen, Tenney et al. 2009; Fry, Chagnon et al. 2010).

There has also been evidence to the contrary that PTPsigma may function as a positive regulator in axon outgrowth. First, it was shown that PTPsigma promotes axon growth in retinal ganglion cells of chicks and that this involved an interaction with heparin sulfate proteoglycans (HSPGs) (Ledig, Haj et al. 1999; Aricescu, McKinnell et al. 2002; Rashid-Doubell, McKinnell et al. 2002). In fact, a substrate of purified PTPsigma ectodomains could directly support the growth of these retinal axons (Sajnani, Aricescu et al. 2005). A study combining crystallography and colocalization data reconciled these findings, demonstrating that CSPGs and HSPGs compete for occupation of a shared binding site in the ectodomain of PTPsigma to inhibit or promote outgrowth, respectively (Coles, Shen et al. 2011).

PTPsigma – Cytosolic Functions and Proteolytic Processing

While the function of the ectodomain of PTPsigma and its interactions with ligands has been well described in the control of axon growth, far less has been established concerning the cellular mechanisms by which PTPsigma functions, and more elusive the identity of its cytosolic substrates. N-Cadherin and neurotrophin receptors (TrkA, TrkB, TrkC) are the only substrates demonstrated to be directly dephosphorylated by PTPsigma and also supported *in vivo* (Faux, Hawadle et al. 2007; Siu, Fladd et al. 2007).

An important feature of regulation for PTPsigma and its relatives involves proteolytic processing away from the cell surface (Figure 1.2B). PTPsigma is translated as a pro-protein and undergoes Furin-mediated cleavage upstream of its transmembrane domain while processed through the Golgi. PTPsigma is then destined to the cell surface where it exists as two non-covalently associated subunits. The extracellular E-subunit is shed during a process called ectodomain-shedding. For PTPsigma, this was shown to occur in cells in response to high cell confluence, calcium influx, and treatment with the phorbol ester, TPA (12-O-tetradecanoylphorbol-13-acetate) (Aicher, Lerch et al. 1997). Ectodomain shedding is mediated by extracellular metalloproteases, and is triggered by internalization of a membrane-tethered C-terminal fragment (CTF). While the target of the internalized catalytic domains has not been identified, in the case of PTPsigma, the internalized catalytic domains appear as punctate cytosolic aggregates (Aicher, Lerch et al. 1997). A final proteolytic processing event, evidenced for LAR, involves gamma-secretase-catalyzed intramembrane cleavage, leading to the generation of a soluble intracellular domain (ICD) that is targeted inside the cell (Ruhe, Streit et al. 2006; Haapasalo, Kim et al. 2007). PTPsigma contains similar cleavage residues to LAR, making it therefore plausible that PTPsigma is also processed into an ICD (Figure 1.2).

Computational Models of Signal Transduction

Systems Biology – a Shifting Paradigm in Biology

Systems Biology is an interdisciplinary field founded on the principle that complex physiological networks can be best understood through a holistic integration of numerous scientific approaches (Kitano 2002; Kitano 2002; Kirschner 2005). When processes are analyzed in their entirety, through the complementation of experimentation and computational methods, emergent properties can be revealed which would not have been detected if individual components were studied in isolation (Janes and Yaffe 2006). Integral to the success of this field is the acquisition of large, detailed, high-quality data sets and the ability to analyze, interpret, apply, and model them to reveal higher-order behaviors of systems (Kitano 2002).

The study of signal transduction pathways is of interest to the Systems Biology field. Signaling pathways are comprised of numerous molecules (i.e. proteins, lipids, and metabolites) which interact dynamically in a spatial and temporal manner to control cellular programs and more broadly, network (e.g. immune system) and organismal behaviors. The large number of molecules involved and the infinite interactions that are possible necessitate the use of computational or mathematical models to comprehensively understand them (Hlavacek, Faeder et al. 2006). To date, models have been generated to describe signaling of EGFR, immune system receptors, and NF-κB, among others (Wiley, Shvartsman et al. 2003; Goldstein, Faeder et al. 2004; Tay, Hughey et al. 2010).

Conventional Modeling

The most basic approach to modeling a signaling pathway is through conventional model specification, that is, the description of molecules making up a system and the nature of their relationships to one another written as linear chemical reactions. Differential equations (generally ordinary; ODEs) are defined for each of these reaction schemes (Hlavacek, Faeder et al. 2006). Standard computing methods can be used to diagram a pathway, define equations, and calculate a model (Hlavacek, Faeder et al. 2006). These types of conventional models can be used to describe simple processes when the number of molecules and reactions is manageable. Simple models have been utilized to study cell signaling and are useful in identifying important design principles behind cellular processes (Kholodenko, Demin et al. 1999; Kholodenko, Hancock et al. 2010; Tay, Hughey et al. 2010).

Rule-Based Modeling

The need for a new type of a model manifests when considering a large number of proteins, all with numerous binding sites, modifiable residues, and activities. The potential number of interactions, modifications, and reaction consequences in this case is difficult to comprehend and results in "combinatorial complexity" (Endy and Brent 2001; Blinov, Faeder et al. 2006). A new paradigm in modeling, the use of rule-based models, was created to overcome the inability of conventional mechanics to handle this complexity (Faeder, Blinov et al. 2005). Here, rules are written to specify protein-protein interactions and the activities of molecular species, or agents. A simple rule would be "The SH2 domain of Protein A binds tyrosine residue 100 of Protein B whenever tyrosine residue 100 is phosphorylated." When written in well-defined machine-readable format, such as BioNetGen Language (BNGL), rules can be interpreted and used to generate chemical reactions and new species based on initial starting conditions (Blinov, Faeder et al. 2004; Hlavacek, Faeder et al. 2006). An example of a rule-based model accounting for complexity overlooked in a conventional model was reported for EGFR signaling by Blinov and colleagues (Blinov, Faeder et al. 2006).

Utility of Mathematical Models

Regardless of the methodology chosen for model specification, the aim should be to build a model which accurately reproduces biological observations and subsequently, allows for the testing of biologically-derived predictions and further, generates new, otherwise unpredictable, ideas about the framework or function of a system (Hlavacek, Faeder et al. 2006). As human diseases are often hallmarked by alterations in signaling, it is this predictive and testable power that will provide utility in disease research and the development of therapeutics (Hopkins 2008).

Considerable benefit will be yielded by a model in which the physiological response to very specific changes (i.e. genetic alterations or treatment with targeted-compounds) can be accurately predicted (Hopkins 2008).

Rationale for this Study

This project originated as an effort to identify phosphatases controlling Vps34-PI(3)P signaling, especially those which function in autophagy. Through a loss-of-function screen of all human phosphatase genes, we identified PTPsigma as a potential inhibitor of this signaling axis. Further, RNAi-mediated knockdown of PTPsigma was reported to confer chemoresistance to HeLa cells in culture and PTPsigma expression was decreased significantly in a study of metastatic prostate cancer tissue samples (MacKeigan, Murphy et al. 2005; Tomlins, Mehra et al. 2007). Although there was no precedence for PTPsigma to have a role in autophagy, the robust phenotype in conjunction with potential disease relevance, warranted follow-up investigation. We aimed to investigate the potential novel role for PTPsigma in PI(3)P signaling and autophagy using an integrative approach combining reductionist cell biology and biochemical techniques along with a systems-level mathematical modeling approach.

Specific Aim 1. To characterize the regulation of PI(3)P by PTPsigma.

> **Hypothesis**: PTPsigma regulates cellular PI(3)P through direct dephosphorylation.
>
> We discovered that RNAi-mediated knockdown of PTPsigma increased cellular PI(3)P levels by an unknown mechanism. Structural modeling demonstrated that the membrane-proximal catalytic domain of PTPsigma bears a unique conformation allowing accommodation of PI(3)P, suggesting this lipid may serve as a direct substrate. Accordingly, our aim was to characterize the control PTPsigma exerts on PI(3)P in cells and further characterize the biochemical mechanism by which PTPsigma regulates this lipid using *in vitro* approaches.

Specific Aim 2. To establish a role for PTPsigma in autophagy and chemoresistance.

Hypothesis: PTPsigma functions as a negative regulator of autophagy acting on autophagic vesicles and consequently, loss of PTPsigma drives chemoresistance through enhanced autophagy-mediated cell survival.

We found that upon loss of PTPsigma, cells accumulated abundant PI(3)P-positive vesicles which appeared autophagic. It has been shown that PTPsigma knockdown also confers chemoresistance to cancer cells in culture and its expression is lost in metastatic prostate cancer (MacKeigan, Murphy et al. 2005; Tomlins, Mehra et al. 2007). In this aim, we intended to a) establish the role of PTPsigma as a negative regulator of autophagy, b) determine the processing events which target PTPsigma to PI(3)P-positive autophagic membranes, and c) demonstrate that enhanced autophagy, as in the absence of PTPsigma, confers a survival advantage to cells subjected to chemotherapy. We further performed *in silico*-based identification of small molecule inhibitors of PTPsigma.

Specific Aim 3. To develop a data-driven mathematical model of autophagy.

Hypothesis: A data-driven model of autophagy will simulate and accurately predict perturbations to key autophagic machinery (Vps34 inhibition and loss of Atg9).

Autophagy is a central regulator of cellular function and has emerging implications in human disease. The elucidation of complex signaling processes, such as this, can be aided through the generation of computational models. We aimed to create a model, driven primarily by kinetic cell-based data, which would accurately simulate autophagic vesicle dynamics and allow for the generation and testing of novel predictions. Constructed initially as a simple model and described with conventional mechanics and stochastic simulations, it will serve as the foundation for a comprehensive, rule-based model in the future.

The results of the cell-based interrogation of PTPsigma and its regulation of PI(3)P and autophagy are summarized in Chapter 2. The *in silico*-based identification of small molecule inhibitors of PTPsigma is discussed in Chapter 3. Finally, the mathematical model constructed to understand mammalian autophagy dynamics is outlined in Chapter 4. Chapter 5 concludes with both an overreaching summary and discussion of future directions of these projects.

FIGURES

Figure 1.1. Overview of autophagy. Autophagy is executed in four stages: 1) mTORC1 controls autophagy *initiation* through inhibition of the ULK1/Atg13/FIP200 complex; 2) ULK1 activity permits *nucleation* of the double-membrane phagophore which is largely executed by the Vps34 complex, PI(3)P-binding effectors (i.e. WIPI proteins), and the transmembrane protein, Atg9; 3) membrane *maturation* into an enclosed autophagosome is accomplished by two ubiquitin-like conjugation events involving LC3 and Atg5-Atg12-Atg16; 4) autophagy is completed via *degradation* when the autophagosome fuses with a lysosome to form an autolysosome or alternatively, when it first fuses with an endosome to form an amphisome intermediate organelle that subsequently fuses with the lysosome. For interpretation of the references to color in this and all other figures, the reader is referred to the electronic version of this dissertation.

Figure 1.1 (cont'd)

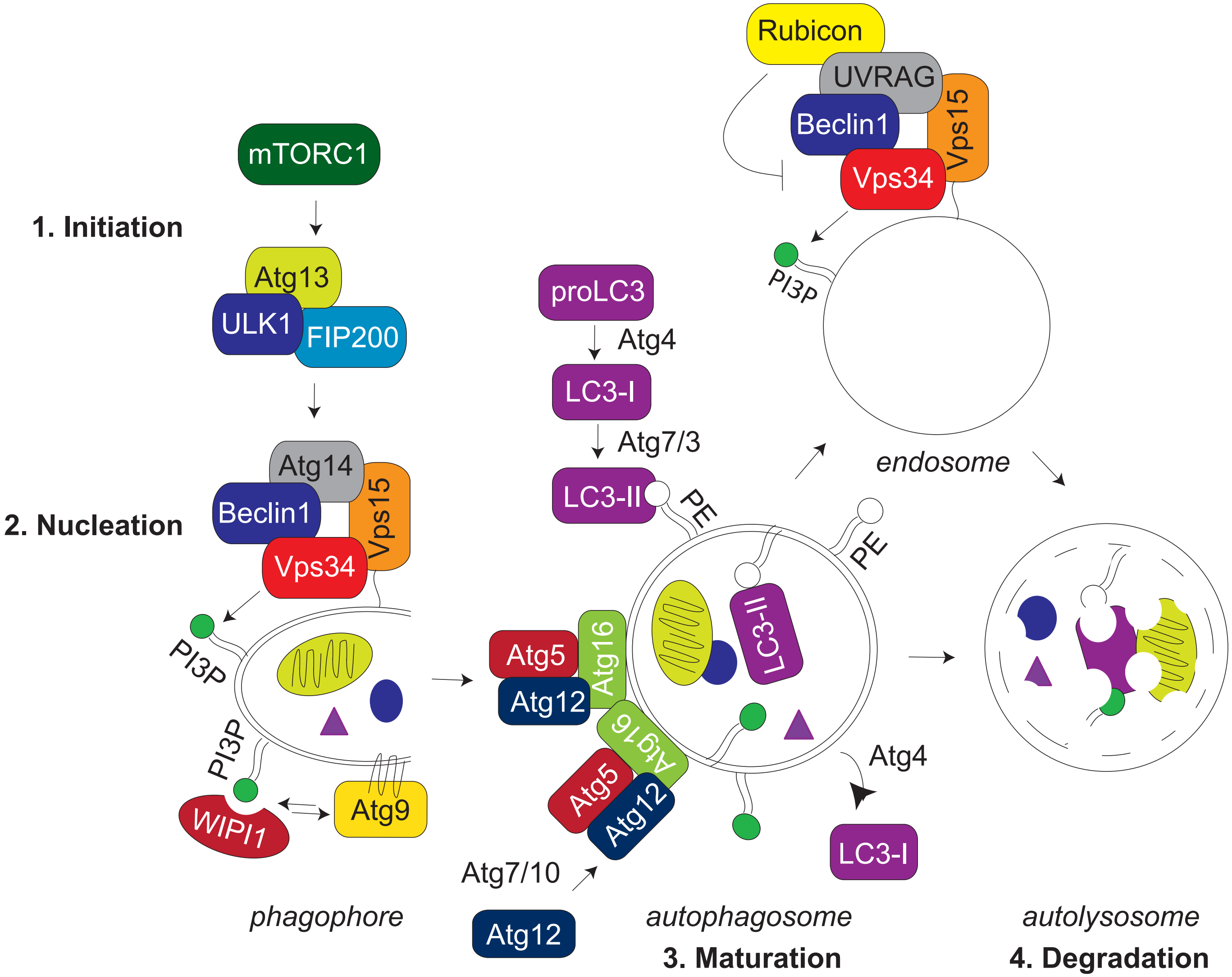

Figure 1.2. Structure and proteolytic processing of PTPsigma. (A) PTPsigma consists of an N-terminal ectodomain made of (3) immunoglobulin (Ig)-like repeats and fibronectin type III-like repeats (up to 8 in the longest isoform). A single transmembrane domain precedes two C-terminal cytosol-facing phosphatase domains, termed D1 and D2. **(B)** PTPsigma is generated as a large pro-protein and following furin-cleavage within the Golgi, is exported to the cell surface as two non-covalently linked subunits (E and P). Cleavage by extracellular metalloproteases results in ectodomain shedding and generation of a membrane-tethered C-terminal fragment (CTF) which can be internalized to the cell. Potential further processing by presenilin (PS) and gamma secretase is predicted to generate a intracellular domain (ICD) which is liberated from the membrane and may also be targeted inside the cell.

Figure 1.2 (cont'd)

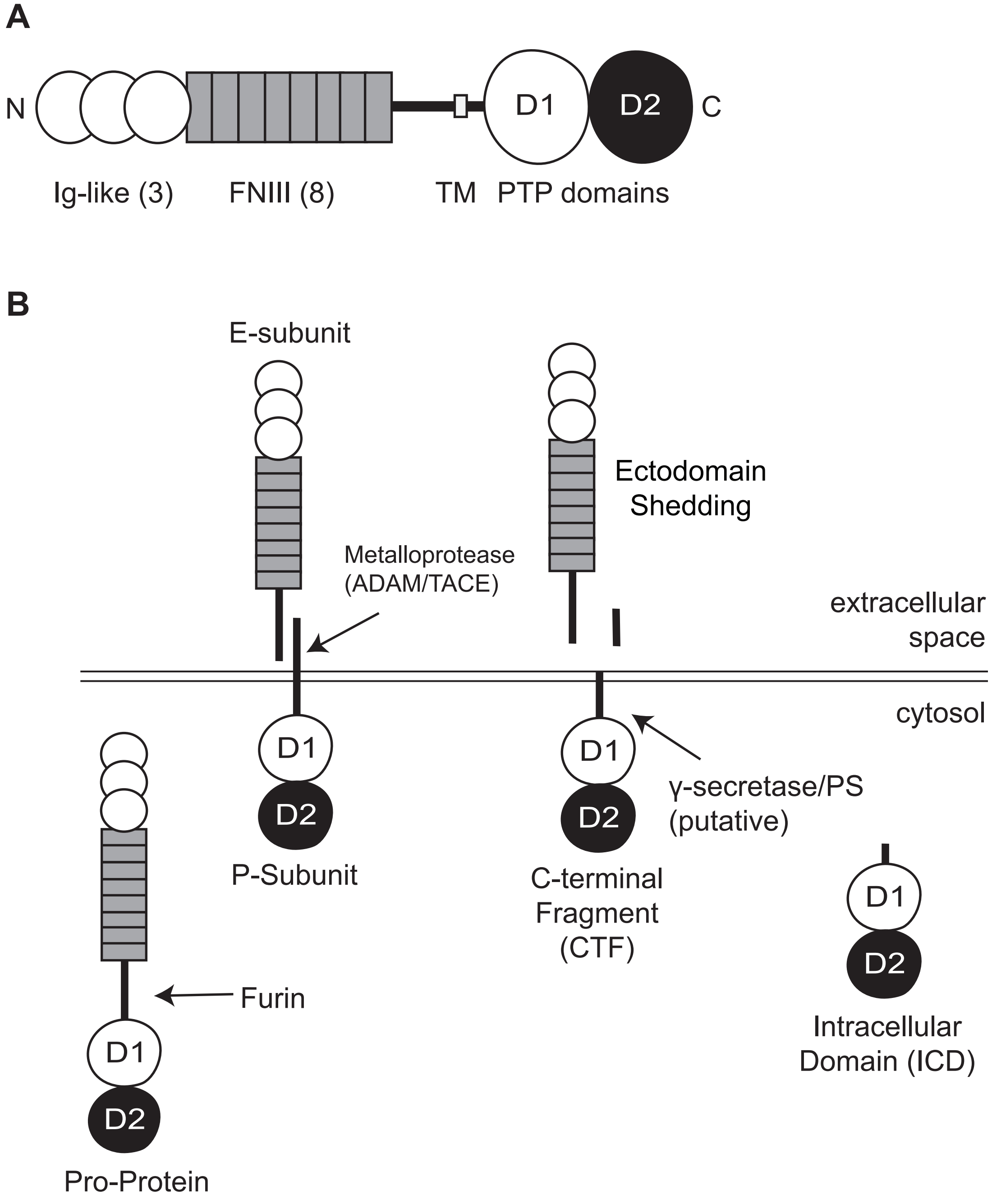

CHAPTER 2

Characterization of PTPsigma as a novel regulator of Vps34-PI(3)P signaling and autophagy

CHAPTER 2 SECTION I

Identification of PTPsigma as an autophagic phosphatase

Modified from

Martin KR, Xu Y, Looyenga BD, Davis RJ, Wu CL, Tremblay ML, Xu HE, Mackeigan JP (2011). Identification of PTPsigma as an autophagic phosphatase. *J Cell Sci*. 2011 Mar 1;124(Pt 5):812-9.

ABSTRACT

Macroautophagy is a dynamic process whereby portions of the cytosol are encapsulated in double-membrane vesicles and delivered to the lysosome for degradation. Phosphatidylinositol-3-phosphate (PI(3)P) is concentrated on autophagic vesicles and recruits effector proteins critical for this process. The production of PI(3)P by the class III phosphatidylinositol 3-kinase (PI3K), Vps34, has been well established; however, protein phosphatases which antagonize this early step in autophagy remain to be identified. To identify such enzymes, we screened human phosphatase genes by RNA interference (RNAi) and found that loss of PTPsigma, a dual-domain protein tyrosine phosphatase (PTP), increases cellular PI(3)P. The abundant PI(3)P-positive vesicles conferred by PTPsigma loss strikingly phenocopied those observed in amino acid-starved cells. Accordingly, we discovered that loss of PTPsigma hyperactivates both constitutive and induced autophagy. Finally, we found that PTPsigma localizes to PI(3)P-positive membranes in cells and this vesicular localization is enhanced during autophagy. Our findings propose a novel role for PTPsigma and provide insight into the regulation of autophagy. Mechanistic knowledge of this process is critical for understanding and targeting therapies for several human diseases, including cancer and Alzheimer's disease, in which abnormal autophagy may be pathological.

INTRODUCTION

In addition to the well-characterized role of PI(3)P in endocytosis, recent evidence has uncovered a critical requirement for this lipid in macroautophagy (autophagy) (Petiot, Ogier-Denis et al. 2000; Axe, Walker et al. 2008; Obara, Noda et al. 2008). Autophagy occurs constitutively in nearly all cells to maintain homeostasis, but is further activated in response to stress as a survival or adaptive mechanism. During autophagy, a double-membrane phagophore forms and elongates around portions of cytosol, matures into an enclosed autophagosome, and delivers its contents to the lysosome for degradation (Klionsky 2007). Basic biochemical components (i.e. amino acids and fatty acids) are exported from the lysosome and recycled by the cell, representing an energetically favorable alternative to de novo synthesis. In mammalian systems, the lipid kinase Vps34 forms a complex with several proteins including Vps15, Beclin1, Atg14L, UVRAG, and Bif1 to generate PI(3)P on autophagic vesicles (Itakura, Kishi et al. 2008; Zhong, Wang et al. 2009). PI(3)P then recruits and tethers effector proteins, such as WIPI-1 (Atg18), which are required for proper membrane formation (Proikas-Cezanne, Waddell et al. 2004; Obara, Sekito et al. 2008). The critical requirement for PI(3)P in this process is evidenced by the fact that autophagy is ablated in mutant Vps34 yeast strains and genetic Vps34 knockouts in *Drosophila* (Kihara, Noda et al. 2001; Juhasz, Hill et al. 2008). Despite knowledge of PI(3)P production, the antagonistic phosphatases which regulate PI(3)P during autophagy have remained elusive. Two myotubularin-related phosphatases, MTMR3 and MTMR14 (hJumpy), have recently been shown to dephosphorylate autophagic PI(3)P in various contexts (Vergne, Roberts et al. 2009; Taguchi-Atarashi, Hamasaki et al. 2010). However, given the complexity of autophagy execution and the number of proteins in the autophagy network, we predict that additional protein phosphatases exist to regulate this process. Accordingly, we performed a high-content cell-based RNAi screen using a fluorescent PI(3)P sensor to identify protein phosphatases that function upstream of PI(3)P during autophagy.

RESULTS

RNAi screen identifies PTPsigma as a modulator of PI(3)P signaling

FYVE (Fab1, YOTB, Vac1, and EEA1) domains are cysteine-rich zinc-finger binding motifs that specifically recognize and bind PI(3)P (Gaullier, Simonsen et al. 1998). An EGFP molecule fused to two tandem FYVE domains, termed EGFP-2xFYVE, serves as an effective cellular sensor of PI(3)P (Gillooly, Morrow et al. 2000). We analyzed U2OS cells stably expressing this construct by fluorescent microscopy and found that PI(3)P predominantly localized to punctate, often perinuclear, vesicles when cultured in complete growth media with full nutrients (Figure 2.1A). RNAi-mediated knockdown of Vps34 reduced cellular PI(3)P content and resulted in a diffuse cytosolic distribution of EGFP-2xFYVE (Figure 2.1B,F; Figure 2.6A). In contrast, a redistribution of EGFP-2xFYVE to small abundant autophagic vesicles occurred when cells were deprived of amino acids to potently induce autophagy (Figure 2.1C).

To identify genes that down-regulate PI(3)P signaling, we utilized multiple siRNAs targeting over 200 known and putative human phosphatases. The siRNAs were introduced into U2OS-EGFP-2xFYVE cells, and the cells were subsequently monitored for PI(3)P signaling. We identified several genes whose knockdown significantly increased cellular EGFP-2xFYVE punctae abundance (Figure 2.1E, Table 2.1). Most notably, PI(3)P was substantially increased following knockdown of the myotubularin family member, MTMR6 (Figure 2.6B,C), as well as the dual-domain PTP, PTPRS (PTPsigma) (Figure 2.1D,E). While reduced expression of MTMR6 was characterized by the appearance of enlarged perinuclear vesicles, the siRNAs targeting PTPsigma caused a dramatic accumulation of abundant smaller vesicles throughout the cytosol which phenocopied that observed during amino acid-starvation (Figure 2.1C,D).

Quantification of PI(3)P-positive vesicles revealed a 3.5-fold increase in abundance during starvation-induced autophagy and a nearly 5-fold increase caused by PTPsigma knockdown alone (Figure 2.1F). This phenotype was confirmed using four unique siRNA sequences targeting PTPsigma (Figure 2.6D-K).

To validate a physiological increase in PI(3)P following knockdown of PTPsigma, phospholipids were radiolabeled with ^{32}P-orthophosphate in vivo, extracted, and resolved by thin layer chromatography. Indeed, PI(3)P levels were specifically elevated in the absence of PTPsigma, while other lipid species remained unchanged (Figure 2.1D). In order to determine the identity of the PI(3)P-positive vesicles formed by PTPsigma knockdown, we immunostained cells with well-established markers of early endosomes (anti-EEA1 [early endosomal antigen 1]) and autophagic vesicles (AVs) (anti-LC3 [light chain 3]). We found that knockdown of PTPsigma had no substantial effect on the presence of EEA1-positive endosomes (Figure 2.1H; Figure 2.7A), but significantly increased the abundance of LC3-positive vesicles (Figure 2.1I). From this, we hypothesized that PTPsigma functions during autophagy and focused our attention on this enzyme as a candidate autophagic phosphatase.

Loss of PTPsigma hyperactivates constitutive and induced autophagy

The striking resemblance of PI(3)P-positive vesicles induced by PTPsigma knockdown to AVs formed during amino acid-starvation led us to propose that autophagy is hyperactivated in the absence of PTPsigma, despite the presence of nutrients. To test this, autophagy was analyzed in U2OS cells by evaluating two ubiquitin-like proteins, Atg12 and LC3 (Atg8), which become conjugated to AVs during autophagy. Following phagophore nucleation, Atg12 covalently binds Atg5 and oligomerizes with Atg16L at the autophagic membrane (Klionsky 2007). To measure vesicle abundance at this step, we immunostained cells for endogenous Atg12 and quantified Atg12-positive punctae. We found that PTPsigma knockdown increased AV abundance 3- to 5-fold from control when cells were cultured with rapamycin, a potent mTOR inhibitor and autophagy inducer, or full nutrients, respectively (Figure 2.2A; Figure 2.7B).

The membrane-bound Atg5/12/16L complex permits lipidation of LC3, a classic marker for AVs (Hanada, Noda et al. 2007). LC3 is unique among the autophagy proteins in that a portion of it remains membrane-bound and is degraded in the lysosome along with vesicle cargo. Therefore, lysosomal function can be inhibited [i.e. with bafilomycin A1 (Baf-A1) or chloroquine treatment] and LC3 accumulation used as a measure of autophagic flux (Tanida, Minematsu-Ikeguchi et al. 2005). We found that both PTPsigma knockdown and amino acid-starvation increased the abundance of LC3-II, the AV-lipidated form of LC3, when lysates were probed with endogenous antibodies (Figure 2.2B). Similarly, we observed an increased number of EGFP-LC3-positive punctae when PTPsigma expression was reduced under normal growth conditions, and these structures accumulated substantially when cells were cultured with Baf-A1, indicating their functionality (Figure 2.2C-F). PTPsigma knockdown caused an even greater increase in EGFP-LC3 punctae from control when cells were treated with both Baf-A1 and rapamycin (Figure 2.2G,H). Similar results were obtained when AVs were quantified from cells immunostained for endogenous LC3 (Figure 2.7C).

To confirm hyperactive autophagy in the absence of PTPsigma independently of fluorescent markers, we detected AVs by transmission electron microscopy (TEM). Autophagosomes are hallmarked by unique double-membranes and by the presence of engulfed cytosolic content- features which allow them to be detected by TEM. These vesicles fuse with the lysosomes or with endocytic compartments destined for the lysosome, generating degradative autolysosomal vesicles which can also be observed by TEM. While control cells contained very few AVs, chloroquine treatment increased their abundance, most of which appeared to be autolysosomal as expected (Figure 2.3A,B). Similarly, cells deprived of amino acids for one hour harbored elevated numbers of AVs, as did cells transfected with PTPsigma siRNAs but cultured in full nutrients (Figure 2.3C,D). These AVs generally appeared to be later stage degradative structures, consistent with active flux through the pathway. To establish this phenotype independent of RNAi, we examined autophagy during PTPsigma loss using wild-type (*Ptprs*$^{+/+}$) and PTPsigma knockout (*Ptprs*$^{-/-}$) murine embryonic fibroblasts (MEFs). We have previously generated *Ptprs*$^{-/-}$ mice by inserting a selectable neomycin resistance gene into the D1 phosphatase (catalytic) domain. From these mice, we generated MEFs that lack both *Ptprs* transcript and protein, as measured by northern blot and western blot, respectively (Elchebly, Wagner et al. 1999). TEM analysis showed that both *Ptprs*$^{+/+}$ and *Ptprs*$^{-/-}$ primary MEFs contained a basal level of AVs; however, they were twice as abundant in *Ptprs*$^{-/-}$ MEFs (Figure 2.3E-G). Again, most structures appeared to be degradative late stage vesicles. *Ptprs*$^{-/-}$ MEFs also contained a number of membrane whorls which may or may not be related to an autophagy phenotype. Collectively, these results demonstrate that loss of PTPsigma, by RNAi and genetic deletion, increases both constitutive and induced autophagy.

PTPsigma localizes to PI(3)P-positive vesicles and rescues the siRNA phenotype

Given the robust PI(3)P response elicited by PTPsigma knockdown, we hypothesized that PTPsigma may regulate autophagy by functioning at the level of PI(3)P-positive vesicles.

PTPsigma is a bulky receptor-like PTP with an extracellular segment and two tandem cytosolic phosphatase domains (termed D1 and D2). Complex processing events have been reported for PTPsigma and related enzymes, including ectodomain shedding and internalization from the cell surface (Aicher, Lerch et al. 1997; Ruhe, Streit et al. 2006). In order to determine the localization of PTPsigma phosphatase domains, untagged full-length protein (FL-PTPsigma) was transiently expressed in U2OS-EGFP-2xFYVE cells and detected by fluorescent microscopy using D1-targeted monoclonal antibodies. We found that in addition to its presence at the plasma membrane, PTPsigma localized to the perinuclear region and to numerous intracellular vesicle-like structures, many of which were PI(3)P-positive (Figure 2.4A). Strikingly, autophagy induction by amino acid-starvation induced a redistribution of PTPsigma to smaller vesicles which were abundant throughout the cytosol and were almost entirely PI(3)P-positive (Figure 2.4B,C). In support of the notion that this localization was autophagic, we discovered that PTPsigma was capable of localizing to mRFP-LC3-positive punctae in the context of both basal and induced autophagy as well (Figure 2.8B).

We further used exogenous PTPsigma expression in an RNAi rescue experiment to demonstrate the specificity of the PTPRS siRNA-induced phenotype. The naturally-occurring isoform of PTPsigma used in our studies lacks the fourth through seventh fibronectin domains (present in the longest isoform): a region encompassing the sequence targeted by a potent siRNA (siRNA-1; see Figure 2.6E,J,K) (Pulido, Serra-Pages et al. 1995). The accumulation of small, abundant, non-perinuclear PI(3)P-positive vesicles induced by siRNA transfection was rescued by exogenous expression of PTPsigma, an effect which was dose-dependent (Figure 2.4D,E). This result suggests a target-specific effect of siRNA-mediated PTPsigma knockdown and a role for this enzyme in PI(3)P signaling.

To verify that the PTPsigma-positive punctate structures were in fact vesicles functioning in a lysosomal pathway, we monitored PTPsigma localization in Baf-A1-treated cells. Baf-A1 prevents maturing vesicles (e.g. endocytic and autophagic) from fusing with lysosomes and in turn, they accumulate in a perinuclear region. We found that PTPsigma-positive vesicular structures began to accumulate quickly (within 15 minutes) and densely populated the perinuclear region within several hours (Figure 2.4F). This suggests that PTPsigma normally localizes to vesicles destined for the lysosome.

Finally, to determine if PTPsigma functions upstream or downstream of PI(3)P at the starvation-induced punctae, we analyzed its localization in cells depleted of the phospholipid. Autophagy was induced by amino acid-starvation in cells treated with wortmannin, a potent and irreversible inhibitor of Vps34 and other PI3K isoforms, or vehicle (DMSO). In vehicle-treated cells, starvation induced the formation of abundant PI(3)P-positive vesicles which also contained PTPsigma (Figure 2.5A). Conversely, wortmannin treatment essentially ablated the formation of PI(3)P during starvation; however, PTPsigma was still recruited to the abundant punctate structures (Figure 2.5B). This finding suggests that the localization of PTPsigma to intracellular structures formed during autophagy occurs upstream, or independently, of PI(3)P.

DISCUSSION

Through use of a high-content cell-based RNAi screen, we have identified phosphatases whose knockdown elevates cellular PI(3)P. Notably, RNAi-mediated knockdown of MTMR6 and several other phosphatases resulted in swollen and often perinuclear PI(3)P-positive vesicles. Previous studies have shown similar phenotypes when endocytic PI(3)P is elevated, for example, by constitutive activation of early endosomal Rab5, or knockdown of the PI5-kinase, PIKfyve (Murray, Panaretou et al. 2002; Rutherford, Traer et al. 2006). Accordingly, the vesicles observed following knockdown of these phosphatases are likely endosomal and these enzymes, including MTMR6, may function in endocytic signaling. Of note, knockdown of both PTPN11 (SHP2) and PTPN13 (PTPL1) resulted in increased EGFP-2xFYVE punctae (Table 2.1). PTPN13, a phosphatase proposed to have both tumor suppressive and oncogenic functions, has been implicated in several signal transduction pathways. Specifically, PTPN13 was shown to inhibit PI3K/Akt signaling and thus, the PI(3)P phenotype elicited by knockdown could potentially be explained by altered 3’-phosphoinositide metabolism (Dromard, Bompard et al. 2007; Abaan and Toretsky 2008). Mutations in SHP2 are associated with several human diseases, most notably Noonan syndrome, LEOPARD syndrome, and juvenile myelomonocytic leukemia (Araki, Mohi et al. 2004; Mohi, Williams et al. 2005; Kontaridis, Swanson et al. 2006; Mohi and Neel 2007). Its activity has been linked to numerous signaling pathways, often downstream of receptor tyrosine kinases, and the observed phenotype could be a consequence of disruption of any number of substrates (Chan, Kalaitzidis et al. 2008).

Surprisingly, we did not identify MTMR3 or MTMR14 (hJumpy), the PI(3)P-phosphatases with reported roles in autophagy. The myotubularin phosphatases comprise a large, highly conserved family of enzymes whose members have been shown to function as heteromeric partners (Lorenzo, Urbe et al. 2006). As one example, MTMR3 and MTMR4, both FYVE-domain containing phosphatases, have been demonstrated to interact and inhibit PI(3)P (Lorenzo, Urbe et al. 2006). Accordingly, gene-by-gene loss of function analysis of this family may not reveal phenotypes if compensation within the family occurs. Further, these enzymes may serve cell- or context-specific functions not revealed in this study.

The most striking result from this study was the presence of abundant PI(3)P-positive vesicles following PTPsigma knockdown which phenocopied that of an autophagic cell. We confirmed hyperactive autophagy in the absence of PTPsigma through use of multiple autophagy markers, as well as electron microscopy. Atg12 and LC3-positive autophagic vesicles were substantially more abundant in the absence of PTPsigma when cells were cultured in full nutrients (constitutive AVs) or treated with rapamycin (induced AVs). These autophagic vesicles accumulated upon treatment with the lysosomal inhibitors, Baf-A1 and chloroquine, demonstrating that they were functional and destined for lysosomal degradation. This phenotype suggests PTPsigma regulates an early step in autophagy induction and its loss results in increased autophagic vesicle generation. This is consistent with the fact that PI(3)P is generated on early phagophores and is required for proper autophagic vesicle formation. A role for PTPsigma in autophagy induction and specifically, PI(3)P regulation, is supported by our findings that PTPsigma localizes to PI(3)P-positive vesicles which increase in number during autophagy.

It remains to be addressed how PTPsigma is targeted to autophagic vesicles. PTPsigma is expressed at the cell surface in a two subunit complex comprised of a large ectodomain and a membrane-spanning intracellular domain. Accordingly, it is implicated in cell-cell and cell-ECM interactions, and it is a critical regulator of axon homeostasis and neuronal development (Aicher, Lerch et al. 1997; Elchebly, Wagner et al. 1999; Wallace, Batt et al. 1999; Uetani, Chagnon et al. 2006). Relevant to our own work, ectodomain shedding and internalization of a membrane-bound carboxy-terminal fragment has been demonstrated previously (Aicher, Lerch et al. 1997). Through immunofluorescent analysis of PTPsigma using D1 domain-specific antibodies, we place intracellular PTPsigma on PI(3)P-positive autophagic vesicles. Autophagosomes frequently fuse with endosomes during their maturation, forming hybrid organelles called amphisomes, establishing the possibility that PTPsigma is internalized by endocytosis to arrive at autophagic vesicles (Klionsky 2007). Further, the close relative of PTPsigma, LAR (PTPRF), undergoes an additional proteolytic event whereby a soluble intracellular domain is formed and targeted inside the cell, similar to the Notch receptor (Ruhe, Streit et al. 2006). PTPsigma contains similar cleavage residues to LAR, making it therefore plausible that PTPsigma is targeted from the plasma membrane to autophagic vesicles through a series of proteolytic events in response to autophagic stimuli. Thus, this phosphatase may serve several unique functions during various cellular conditions which are governed by its subcellular localization.

A critical finding presented here is the recruitment of PTPsigma to vesicular structures during amino acid-starvation which occurs even in the absence of PI(3)P generation. This finding, together with the hyperactivation of autophagy elicited by PTPsigma knockdown (as measured by PI(3)P, Atg12, and LC3), suggests PTPsigma regulates autophagy at an early step upstream of this lipid. In further support of this, we found that while almost all PTPsigma-positive vesicles are also positive for PI(3)P (EGFP-2xFYVE presence), fewer harbored LC3, a marker which is incorporated into AVs at later maturation stages.

There are several potential mechanisms by which PTPsigma may function to regulate autophagy. First, it is possible that PTPsigma could directly dephosphorylate PI(3)P following recruitment to AVs. We did test the activity of recombinant PTPsigma in vitro, and while we could not detect PI(3)P-phosphatase activity, it cannot be entirely excluded that PI(3)P does not serve as a direct substrate *in vivo* (Figure 2.9). It is also possible that PTPsigma uses its robust protein phosphatase activity to regulate the function of a PI(3)P-modifying enzyme, such as a PI(3)P-phosphatase or a PI(4)- or PI(5)-kinase. Alternatively, PTPsigma could control the activity of Vps34, which contains at least one phosphotyrosine site, or another component within the larger Vps34 complex (Imami, Sugiyama et al. 2008). Finally, PTPsigma may contribute to the regulation of autophagy at the earliest initiation step, which is executed by a complex of autophagy proteins, namely ULK1 (Atg1) and Atg13. The functional formation of this complex, which permits the generation of the PI(3)P-positive phagophore, was recently found to be tightly regulated by phosphorylation events (Chang and Neufeld 2009; Ganley, Lam du et al. 2009; Hosokawa, Hara et al. 2009; Jung, Jun et al. 2009). The aim of future work will be to determine the precise mechanism by which PTPsigma functions to regulate autophagy.

MATERIALS AND METHODS

siRNA screen and validation

U2OS-EGFP-2xFYVE cells were seeded on 96-well plates (2,000 per well) in McCoy's 5A medium (Invitrogen, Carlsbad, CA) supplemented with 10% fetal bovine serum (FBS, Invitrogen) at 37°C for 24 hours. Four siRNA molecules per phosphatase gene (phosphatase siRNA library version 2.0, Qiagen, Valencia, CA) were transfected per well at a final concentration of 25 nM using 0.2 μl HiPerfect transfection reagent (Qiagen) per well. After 48 hours, cells were fixed with 3.7% formaldehyde and nuclei were stained with Hoechst-33342 (Invitrogen). Cells were visualized at 40x on a Zeiss LSM 510 Meta confocal microscope (Oberkochen, Germany) and EGFP-2xFYVE fluorescence was compared to that of control siRNA-transfected cells within each plate. Triplicate wells from each gene were qualitatively scored by two independent scorers on a scale from –100 (decreased EGFP-2xFYVE signal and distribution) to +100 (increased) and mean scores were determined. Twenty-seven phosphatase genes whose knockdown increased EGFP-2xFYVE fluorescence in the primary screen were used in a secondary screen, where four siRNAs were individually transfected to eliminate off-target hits. The primary score was multiplied by a binned secondary screen score (score of 1.0 for 3 or 4 of 4 siRNAs yielding a phenotype; 0.75 for 2 of 4 siRNAs; and 0 for 0 or 1 of 4 siRNAs). Quantitative real-time PCR (qRT-PCR) assays with SYBR green dye (Roche, Basel, Switzerland) and gene-specific primers confirmed that siRNAs effectively reduced mRNA expression of target genes. For imaging, cells were cultured on number 1.5 coverglass, transfections repeated as above, cells fixed, nuclei stained, and coverglass inverted into microslides with mounting gel. A control siRNA transfected well was cultured for 3 hours in amino acid-starvation media [Dulbecco's phosphate-buffered saline (DPBS) with 10% FBS and 1 g/L D-glucose]. Cells were imaged using a 60x oil objective on a Nikon TE300 fluorescent microscope (Tokyo, Japan). EGFP-2xFYVE-positive vesicles were quantified using image analysis software.

Phospholipid labeling, extraction, and thin layer chromatography (TLC)

U2OS cells were seeded in McCoy's 5A with 10% FBS at 200,000 cells per well of 6-well tissue culture plates. After 24 hours, control or PTPRS siRNAs were transfected at a final concentration of 25 nM using 2 μl HiPerfect transfection reagent per ml medium. Control siRNA was All-star Negative Control (Qiagen) and PTPRS siRNAs were two unique sequences (SI02759288, SI03056284, Qiagen). After 48 hours of transfection, the medium was replaced with phosphate-free DMEM (Invitrogen) supplemented with 10% phosphate-free FBS for 30 min. $^{32}PO_4$ (0.25 mCi) was added per ml of medium for an additional 2 hours (Perkin Elmer, Waltham, MA). Radiolabeling was quenched with ice-cold TCA (10% final concentration) and cells incubated on ice for 1 hour. Cells were scraped, pelleted, and lipids extracted via an acidified Bligh and Dyer method (Bird 1994). Lipids were lyophilized, resuspended in chloroform:methanol (1:1), spotted on 20 cm x 20 cm silica gel TLC plates (Whatman, Maidstone, UK), and resolved in a chamber using boric acid buffer (Walsh, Caldwell et al. 1991). A PI(3)P standard was generated by incubating synthetic phosphatidylinositol (diC16 PtdIns; Echelon, Salt Lake City, UT) with immunoprecipitated PI3K (using anti-p85, Cell Signaling, Danvers, MA) and ^{32}P-ATP (Perkin Elmer). The TLC plate was exposed to film for 20 hours at –80°C and developed.

Fluorescent microscopy and western blot analyses of autophagy markers

U2OS cells were seeded at a density of 35,000 cells per well in McCoy's 5A medium with 10% FBS on number 1.5 coverglass in 24-well tissue culture plates (for fluorescent imaging) or 150,000 cells per well on 6-well dishes (for western blot). After 24 hours, cells were transfected with control or PTPRS siRNAs for 48 hours, as described above. Following, cells were treated for 1-2 hours in amino acid-starvation media or with 50 nM rapamycin (Calbiochem, San Diego, CA), 25 μM chloroquine (Sigma-Aldrich, St. Louis, MO), 100 nM Baf-A1 (A.G. Scientific, San Diego, CA) or normal growth medium (full nutrients; McCoy's 5A with 10% FBS), as indicated. For western blots, cells were lysed [in 10 mM KPO_4, 1 mM EDTA, 10 mM $MgCl_2$, 5 mM EGTA, 50 mM bis-glycerophosphate, 0.5% NP40, 0.1% Brij35, 0.1% sodium deoxycholate, 1 mM $NaVO_4$, 5 mM NaF, 2 mM DTT, and complete protease inhibitors (Sigma-Aldrich)] and 20 μg of total protein was resolved by SDS-PAGE. Proteins were transferred to PVDF membranes and probed with primary antibodies (LC3B, Cell Signaling Technologies; anti-α-tubulin, Sigma-Aldrich) for 16 hours at 4°C followed by secondary antibodies (HRP-linked rabbit- or mouse- IgG, GE, Piscataway, NJ) for 1 hour at room temperature. Proteins were detected by enhanced chemiluminescence. For EGFP-LC3 imaging, U2OS cells stably expressing ptfLC3 (Addgene plasmid 21074) (Kimura, Noda et al. 2007) were fixed with 3.7% formaldehyde and nuclei stained with Hoechst-33342 (2 μg/ml). Coverglass were inverted onto microslides using mounting gel and cells imaged using a 100x oil-immersion objective on a Nikon Eclipse Ti fluorescence microscope. For immunofluorescence, cells were fixed with 3.7% formaldehyde, permeabilized with 0.2% triton-X 100, and blocked with 3% bovine serum albumin (BSA) in PBS. Antibodies (LC3B, Atg12, EEA1; Cell Signaling Technologies) were added for 16 hours at 4°C followed by Alexa Fluor (AF)-488 conjugated anti-rabbit IgG (Invitrogen) for 1 hour at room temperature. Nuclei were counterstained with Hoechst-33342, coverglass inverted onto microslides using mounting gel, and cells imaged using 60x or 100x oil-immersion objectives on a Nikon TE300 fluorescence microscope (LC3, Atg12) or a 63x water-immersion objective on a Zeiss LSM510 Meta confocal microscope (EEA1). For quantification, punctae were counted using image analysis software after establishing an intensity threshold.

Transmission electron microscopy (TEM)

U2OS cells in 10 cm dishes were transfected with control or PTPRS siRNAs for 48 hours as described above. Cells (siRNA-transfected U2OS cells or primary MEFs) were briefly trypsinized, pelleted, rinsed, and resuspended in 2% glutaraldehyde fixative (Sigma-Aldrich). Cell pellets were embedded in 2% agarose, postfixed in osmium tetroxide, and dehydrated with an acetone series. Samples were infiltrated and embedded in Poly/Bed 812 resin and polymerized at 60°C for 24 hours. Ultrathin sections (70 nm) were generated with a Power Tome XL (Boeckeler Instruments, Tucson, Arizona) and placed on copper grids. Cells were examined using a JEOL 100CX Transmission Electron Microscope at 100 kV (Tokyo, Japan). Autophagic structures were quantified from images encompassing approximately 8.5 μm^2 of cell area each. Electron microscopy services were performed by Alicia Pastor and the Michigan State University Center for Advanced Microscopy (East Lansing, MI). MEFs were provided by Michel L. Tremblay (McGill University, Goodman Cancer Center).

Exogenous PTPsigma expression and immunofluorescence

U2OS-EGFP-2xFYVE cells were seeded at a density of 20,000 cells per well in McCoy's 5A medium with 10% FBS on number 1.5 coverglass in 24-well tissue culture dishes. Full-length PTPsigma cDNA (BC104812) was inserted into pRK7 by EcoRI digestion and ligation to yield FL-PTPsigma-pRK7 (FL-PTPsigma). DNA was transfected at 0.15 µg per well using 0.45 µl FuGeneHD transfection reagent (Roche, Mannheim, Germany) in 50 µl Optimem and 450 µl McCoy's 5A with 10% FBS for 24 hours. For two hours, cells were cultured with full nutrient media or starved of amino acids (Fig. 4A-C), or amino acid-starved while treated with DMSO or 100 nM wortmannin (Sigma-Aldrich) (Figure 2.5, Figure 2.8). Alternatively, cells were treated with Baf-A1 (100 nM in full nutrient media) for 0, 15, 60, or 240 minutes (Figure 2.4E). Cells were then fixed with 3.7% formaldehyde, permeabilized with 0.2% Triton-X 100, blocked in 3% BSA, and stained with antibodies targeting the D1 domain of PTPsigma for 2 hours at room temperature. AF-546-conjugated anti-mouse-IgG (Invitrogen) were incubated for an additional hour at room temperature and nuclei stained with Hoechst-33342. Cells were imaged using oil-immersion objectives at 60x on a Nikon TE3000 or 100x on an Eclipse Ti fluorescent microscope. For Fig. 4C, cells were treated as above and imaged using a 63x water-immersion objective on a Zeiss LSM510 Meta microscope. Red (AF-546, FL-PTPsigma) and green (EGFP-2xFYVE, PI(3)P) channels were captured with confocality through the Z-plane using 16 increments of 0.25 µm. Stacks through the indicated X and Y planes are shown at the border of an image of the third Z-plane. For Figure 2.8B, U2OS cells stably expressing mRFP-LC3 (Addgene plasmid 21075) (Kimura, Noda et al. 2007) were seeded, transfected, treated (full nutrient or amino acid starvation media for 2 hours), and stained as above. Images were captured at 100x using an oil-immersion objective on an Eclipse Ti fluorescent microscope.

Rescue of siRNA phenotype

U2OS-EGFP-2xFYVE cells were seeded on number 1.5 coverglass in 24-well dishes at 20,000 cells per well in McCoy's 5A medium with 10% FBS. 24 hours later, PTPRS siRNA-1 (CACGGCATCAGGCGTGCACAA; Qiagen) was transfected at a concentration of 25 nM using 1 μl oligofectamine per well per 500 μl McCoy's with 10% FBS (Invitrogen). FL-PTPsigma-pRK7 plasmid DNA was transfected 24 hours later at a concentration of 0.15 μg DNA per well using 0.45 μl FuGeneHD transfection reagent in 50 μl Optimem and 450 μl McCoy's 5A with 10% FBS for an additional 24 hours. Cells were fixed and immunostained as described above. Cells were imaged using a 60x oil objective on a Nikon TE300 fluorescent microscope for EGFP-2xFYVE phenotype (green) and FL-PTPsigma-pRK7 expression (red). FL-PTPsigma-pRK7 expression levels were categorized as high or low. The presence or absence of a robust PTPRS siRNA-induced EGFP-2xFYVE phenotype was determined (phenotype defined as the presence of small, abundant, non-perinuclear EGFP-2xFYVE-positive vesicles; indicated with white arrows in Figure 2.4D) for 30-40 cells each of low and high FL-PTPsigma-expressing cells as well as cells transfected with PTPRS siRNA-1 but not FL-PTPsigma-pRK7.

In vitro phosphatase assays

GST-tagged recombinant PTPsigma containing all residues C-terminal to the transmembrane domain (BC104812 cDNA; aa 883-1501) was generated in pGEXKG (Guan and Dixon 1991). GST-tagged full-length MTMR6 (NM_004685.2) was generated in pGEXKG and GST-tagged recombinant PTP1B was purchased (Upstate, Billerica, MA). Proteins were purified from BL21 Escherichia coli after isopropyl β-D-1-thiogalactopyranoside (IPTG) induction and used in phosphatase assays. For PI(3)P-phosphatase reactions, 1μg protein was suspended in 50 µl assay buffer (50 mM sodium acetate, 25 mM Tris-HCl, 10 mM DTT, pH 6.5) with 0, 25, 50, or 200 µM diC8-PI(3)P and reactions carried out at 37°C for 25 min. For p-Tyr-phosphatase assays, reactions were carried out as above using 0, 10, 25, or 100 µM p-Tyr peptide (TSTEPQpYQPGENL; Upstate) at 37°C for 15 min. Released phosphates were detected with malachite green (Upstate) and absorbance measured at 650 nm. Background levels from enzyme-only and substrate-only (p-Tyr or PI(3)P) reactions were subtracted and absorbance converted to picomoles free phosphate released per minute using a standard curve.

ACKNOWLEDGEMENTS

We thank the Van Andel Institute Systems Biology lab for advice, analysis, and reagents. This work was supported by the Department of Defense Prostate Cancer Research Program of the Office of Congressionally Directed Medical Research Programs PC081089 to J.P. MacKeigan. J.P. MacKeigan is also supported by Award Number R01CA138651 from the National Cancer Institute.

TABLES

Table 2.1. siRNA-mediated knockdown of human phosphatase genes alters cellular PI(3)P. U2OS-EGFP-2xFYVE cells were transfected with siRNAs targeting human phosphatase genes for 48 h (4 siRNA sequences per gene per well; all four sequences displayed). Following knockdown, EGFP-2xFYVE signal and distribution was visualized by confocal microscopy and scored from -100 (decreased punctae from control cells) to +100 (increased punctae) and means determined. Select genes were validated using multiple unique siRNA sequences and their efficacy was incorporated into their scores (see *Methods*). Genes were ranked based on their scores from 1 (most increased EGFP-2xFYVE) to 206 (most decreased).

Table 2.1 (cont'd)

Gene Symbol	Description	Score	Rank
ACP1	acid phosphatase 1, soluble	25	40
ACP2	acid phosphatase 2, lysosomal	-17	176
ACP5	acid phosphatase 5, tartrate resistant	25	41
ACP6	acid phosphatase 6, lysophosphatidic	-8	167
ACPP	acid phosphatase, prostate	42	20
ACPT	acid phosphatase, testicular	0	117
ALPI	alkaline phosphatase, intestinal	58	9
ALPL	alkaline phosphatase, liver/bone/kidney	25	42
ALPPL2	alkaline phosphatase, placental-like 2	17	63
CDC25A	cell division cycle 25A	17	64
CDC25B	cell division cycle 25B	50	13
CDC25C	cell division cycle 25C	17	65
CDKN3	cyclin dependent-kinase inhibitor 3 (CDK2-associated dual specificity phosphatase)	25	43
CTDP1	CTD (carboxy-terminal domain, RNA polymerase II, polypeptide A) phosphatase, subunit 1	0	118
CTDSP2	CTD (carboxy-terminal domain, RNA polymerase II, polypeptide A) small phosphatase 2	8	85
CTDSPL	CTD (carboxy-terminal domain, RNA polymerase II, polypeptide A) small phosphatase-like	8	86
DKFZP566K0524	DKFZP566K0524 protein	17	66
DOLPP1	dolichyl pyrophosphate phosphatase 1	0	119
DUSP10	dual specificity phosphatase 10	8	87
DUSP11	dual specificity phosphatase 11 (RNA/RNP complex 1-interacting)	8	88
DUSP12	dual specificity phosphatase 12	0	120
DUSP13	dual specificity phosphatase 13	42	21
DUSP14	dual specificity phosphatase 14	8	89
DUSP15	dual specificity phosphatase-like 15	-42	198
DUSP16	dual specificity phosphatase 16	0	121
DUSP18	dual specificity phosphatase 18	33	29

Table 2.1 (cont'd)

DUSP19	dual specificity phosphatase 19	-8	168
DUSP2	dual specificity phosphatase 2	33	30
DUSP21	dual specificity phosphatase 21	0	122
DUSP22	dual specificity phosphatase 22	0	123
DUSP23	dual specificity phosphatase 23	0	124
DUSP24	dual specificity phosphatase 24 (putative)	-33	193
DUSP3	dual specificity phosphatase 3 (vaccinia virus phosphatase VH1-relate	-33	194
DUSP6	dual specificity phosphatase 6	25	44
DUSP7	dual specificity phosphatase 7	33	31
DUSP8	dual specificity phosphatase 8	42	22
DUT	dUTP pyrophosphatase	42	23
ENPP1	ectonucleotide pyrophosphatase/phosphodiesterase 1	0	125
ENPP2	ectonucleotide pyrophosphatase/phosphodiesterase 2 (autotaxin)	-33	195
ENPP3	ectonucleotide pyrophosphatase/phosphodiesterase 3	0	126
FBP1	fructose-1,6-bisphosphatase 1	0	127
FBP2	fructose-1,6-bisphosphatase 2	0	128
FLJ32332	likely ortholog of mouse protein phosphatase 2C eta	-17	177
G6PC	glucose-6-phosphatase, catalytic (glycogen storage disease type I, vor	0	129
G6PC2	glucose-6-phosphatase, catalytic, 2	50	14
G6PC3	glucose 6 phosphatase, catalytic, 3	0	130
ILKAP	integrin-linked kinase-associated serine/threonine phosphatase 2C	0	131
IMPA1	inositol(myo)-1(or 4)-monophosphatase 1	-17	178
INPP1	inositol polyphosphate-1-phosphatase	50	15
INPP4B	inositol polyphosphate-4-phosphatase, type II, 105kDa	8	90
INPP5A	inositol polyphosphate-5-phosphatase, 40kDa	8	91
INPP5B	inositol polyphosphate-5-phosphatase, 75kDa	33	32
INPP5D	inositol polyphosphate-5-phosphatase, 145kDa	0	132
INPP5E	inositol polyphosphate-5-phosphatase, 72 kDa	0	133
INPP5F	inositol polyphosphate-5-phosphatase F	50	18
ITPA	inosine triphosphatase (nucleoside triphosphate pyrophosphatase)	8	92
LHPP	phospholysine phosphohistidine inorganic pyrophosphate phosphatase	8	93

Table 2.1 (cont'd)

LOC387870	similar to protein tyrosine phosphatase, receptor type, Q isoform 1 precursor; glomerular mesangial cell receptor protein-tyrosine phosphatase; glomerular mesangial cell receptor protein-tyrosine	0	134
LOC389772	similar to Osteotesticular phosphatase; protein tyrosine phosphatase receptor type V; protein tyrosine phosphatase receptor type W; protein tyrosine phosphatase, receptor type, V	0	135
LOC391025	similar to protein tyrosine phosphatase, receptor type, U isoform 2 precursor; protein tyrosine phosphatase J; protein tyrosine phosphatase receptor omicron; pi R-PTP-Psi	56	12
LOC400927	similar to TPTE and PTEN homologous inositol lipid phosphatase isoform alpha; TPTE and PTEN homologous inositol lipid	17	67
LOC442428	similar to fructose-1,6-bisphosphatase 2; fructose-1,6-bisphosphatase isozyme 2; D-fructose-1,6-bisphosphate 1-phosphohydrolase; FBPase; muscle fructose-bisphosphatase; hexosediphosphatase	25	45
LOC474338	SUMO1 pseudogene 3	-8	169
LPPR2	lipid phosphate phosphatase-related protein type 2	0	136
MINPP1	multiple inositol polyphosphate histidine phosphatase, 1	-42	199
M-RIP	myosin phosphatase-Rho interacting protein	25	46
MTM1	myotubularin 1	25	47
MTMR2	myotubularin related protein 2	25	48
MTMR3	myotubularin related protein 3	0	137
MTMR4	myotubularin related protein 4	17	68
MTMR6	myotubularin related protein 6	33	33
MTMR8	myotubularin related protein 8	8	94
MTMR9	myotubularin related protein 9	8	95
PDP2	pyruvate dehydrogenase phosphatase isoenzyme 2	8	96
PDPR	pyruvate dehydrogenase phosphatase regulatory subunit	58	10
PHOSPHO1	phosphatase, orphan 1	-8	170
PHPT1	phosphohistidine phosphatase 1	17	69
PIB5PA	phosphatidylinositol (4,5) bisphosphate 5-phosphatase, A	25	49
PIP3AP	phosphatidylinositol-3-phosphate associated protein	0	138
PLIP	PTEN-like phosphatase	17	70

Table 2.1 (cont'd)

PME-1	protein phosphatase methylesterase-1	33	34
PNKP	polynucleotide kinase 3'-phosphatase	17	71
PPAP2A	phosphatidic acid phosphatase type 2A	8	97
PPAP2B	phosphatidic acid phosphatase type 2B	8	98
PPAP2C	phosphatidic acid phosphatase type 2C	8	99
PPEF1	protein phosphatase, EF hand calcium-binding domain 1	17	72
PPEF2	protein phosphatase, EF hand calcium-binding domain 2	8	100
PPFIA1	protein tyrosine phosphatase, receptor type, f polypeptide (PTPRF), interacting protein (liprin), alpha 1	0	139
PPFIA2	protein tyrosine phosphatase, receptor type, f polypeptide (PTPRF), interacting protein (liprin), alpha 2	0	140
PPFIA3	protein tyrosine phosphatase, receptor type, f polypeptide (PTPRF), interacting protein (liprin), alpha 3	25	50
PPFIA4	protein tyrosine phosphatase, receptor type, f polypeptide (PTPRF), interacting protein (liprin), alpha 4	25	51
PPM1A	protein phosphatase 1A (formerly 2C), magnesium-dependent, alpha i	-58	204
PPM1B	protein phosphatase 1B (formerly 2C), magnesium-dependent, beta is	17	73
PPM1D	protein phosphatase 1D magnesium-dependent, delta isoform	8	101
PPM1E	protein phosphatase 1E (PP2C domain containing)	0	141
PPM1F	protein phosphatase 1F (PP2C domain containing)	0	142
PPM1G	protein phosphatase 1G (formerly 2C), magnesium-dependent, gamma	8	102
PPM1L	protein phosphatase 1 (formerly 2C)-like	8	103
PPM2C	protein phosphatase 2C, magnesium-dependent, catalytic subunit	8	104
PPP1CA	protein phosphatase 1, catalytic subunit, alpha isoform	17	74
PPP1CB	protein phosphatase 1, catalytic subunit, beta isoform	-17	179
PPP1CC	protein phosphatase 1, catalytic subunit, gamma isoform	17	75
PPP1R10	protein phosphatase 1, regulatory subunit 10	-75	205
PPP1R11	protein phosphatase 1, regulatory (inhibitor) subunit 11	0	143
PPP1R12A	protein phosphatase 1, regulatory (inhibitor) subunit 12A	0	144
PPP1R12B	protein phosphatase 1, regulatory (inhibitor) subunit 12B	17	76
PPP1R12C	protein phosphatase 1, regulatory (inhibitor) subunit 12C	-8	171
PPP1R13B	protein phosphatase 1, regulatory (inhibitor) subunit 13B	50	16

Table 2.1 (cont'd)

PPP1R14A	protein phosphatase 1, regulatory (inhibitor) subunit 14A	-17	180
PPP1R14C	protein phosphatase 1, regulatory (inhibitor) subunit 14C	0	145
PPP1R14D	protein phosphatase 1, regulatory (inhibitor) subunit 14D	-25	188
PPP1R15A	protein phosphatase 1, regulatory (inhibitor) subunit 15A	0	146
PPP1R15B	protein phosphatase 1, regulatory (inhibitor) subunit 15B	-25	189
PPP1R16B	protein phosphatase 1, regulatory (inhibitor) subunit 16B	-100	206
PPP1R1A	protein phosphatase 1, regulatory (inhibitor) subunit 1A	17	77
PPP1R1B	protein phosphatase 1, regulatory (inhibitor) subunit 1B (dopamine and cAMP regulated phosphoprotein, DARPP-32)	33	35
PPP1R1C	protein phosphatase 1, regulatory (inhibitor) subunit 1C	67	7
PPP1R2	protein phosphatase 1, regulatory (inhibitor) subunit 2	92	2
PPP1R2P9	protein phosphatase 1, regulatory (inhibitor) subunit 2 pseudogene 9	17	78
PPP1R3A	protein phosphatase 1, regulatory (inhibitor) subunit 3A (glycogen and sarcoplasmic reticulum binding subunit, skeletal muscle)	0	147
PPP1R3B	protein phosphatase 1, regulatory (inhibitor) subunit 3B	17	79
PPP1R3C	protein phosphatase 1, regulatory (inhibitor) subunit 3C	0	148
PPP1R3D	protein phosphatase 1, regulatory subunit 3D	-50	200
PPP1R3F	protein phosphatase 1, regulatory (inhibitor) subunit 3F	-17	181
PPP1R7	protein phosphatase 1, regulatory subunit 7	-25	190
PPP1R8	protein phosphatase 1, regulatory (inhibitor) subunit 8	0	149
PPP1R9A	protein phosphatase 1, regulatory (inhibitor) subunit 9A	-33	196
PPP1R9B	protein phosphatase 1, regulatory subunit 9B, spinophilin	0	150
PPP2CA	protein phosphatase 2 (formerly 2A), catalytic subunit, alpha isoform	0	151
PPP2CB	protein phosphatase 2 (formerly 2A), catalytic subunit, beta isoform	0	152
PPP2R1A	protein phosphatase 2 (formerly 2A), regulatory subunit A (PR 65), alp	25	52
PPP2R1B	protein phosphatase 2 (formerly 2A), regulatory subunit A (PR 65), bet	92	3
PPP2R2A	protein phosphatase 2 (formerly 2A), regulatory subunit B (PR 52), alp	-8	172
PPP2R2B	protein phosphatase 2 (formerly 2A), regulatory subunit B (PR 52), bet	25	53
PPP2R2C	protein phosphatase 2 (formerly 2A), regulatory subunit B (PR 52), gar	33	36
PPP2R2D	protein phosphatase 2, regulatory subunit B, delta isoform	0	153
PPP2R3A	protein phosphatase 2 (formerly 2A), regulatory subunit B'', alpha	8	105
PPP2R4	protein phosphatase 2A, regulatory subunit B' (PR 53)	33	37

Table 2.1 (cont'd)

PPP2R5A	protein phosphatase 2, regulatory subunit B (B56), alpha isoform	0	154
PPP2R5B	protein phosphatase 2, regulatory subunit B (B56), beta isoform	-50	201
PPP2R5C	protein phosphatase 2, regulatory subunit B (B56), gamma isoform	17	80
PPP2R5E	protein phosphatase 2, regulatory subunit B (B56), epsilon isoform	-17	182
PPP3CA	protein phosphatase 3 (formerly 2B), catalytic subunit, alpha isoform (calcineurin A alpha)	-25	191
PPP3CB	protein phosphatase 3 (formerly 2B), catalytic subunit, beta isoform (calcineurin A beta)	-17	183
PPP3CC	protein phosphatase 3 (formerly 2B), catalytic subunit, gamma isoform (calcineurin A gamma)	25	54
PPP3R1	protein phosphatase 3 (formerly 2B), regulatory subunit B, 19kDa, alpha isoform (calcineurin B, type I)	-17	184
PPP4C	protein phosphatase 4 (formerly X), catalytic subunit	-17	185
PPP4R1	protein phosphatase 4, regulatory subunit 1	0	155
PPP5C	protein phosphatase 5, catalytic subunit	42	24
PPP6C	protein phosphatase 6, catalytic subunit	-8	173
PR48	protein phosphatase 2A 48 kDa regulatory subunit	-50	202
PSPH	phosphoserine phosphatase	42	25
PSTPIP1	proline-serine-threonine phosphatase interacting protein 1	-8	174
PSTPIP2	proline-serine-threonine phosphatase interacting protein 2	8	106
PTEN	phosphatase and tensin homolog (mutated in multiple advanced cance	-17	186
PTP4A1	protein tyrosine phosphatase type IVA, member 1	8	107
PTP4A2	protein tyrosine phosphatase type IVA, member 2	8	108
PTP4A3	protein tyrosine phosphatase type IVA, member 3	0	156
PTPDC1	protein tyrosine phosphatase domain containing 1	17	81
PTPLA	protein tyrosine phosphatase-like (proline instead of catalytic arginine),	17	82
PTPLB	protein tyrosine phosphatase-like (proline instead of catalytic arginine),	8	109
PTPN1	protein tyrosine phosphatase, non-receptor type 1	25	55
PTPN11	protein tyrosine phosphatase, non-receptor type 11 (Noonan syndrome	75	5
PTPN12	protein tyrosine phosphatase, non-receptor type 12	50	17
PTPN13	protein tyrosine phosphatase, non-receptor type 13 (APO-1/CD95 (Fas)-associated phosphatase)	83	4

Table 2.1 (cont'd)

PTPN14	protein tyrosine phosphatase, non-receptor type 14	58	11
PTPN18	protein tyrosine phosphatase, non-receptor type 18 (brain-derived)	69	6
PTPN2	protein tyrosine phosphatase, non-receptor type 2	0	157
PTPN21	protein tyrosine phosphatase, non-receptor type 21	8	110
PTPN22	protein tyrosine phosphatase, non-receptor type 22 (lymphoid)	8	111
PTPN23	protein tyrosine phosphatase, non-receptor type 23	-25	192
PTPN3	protein tyrosine phosphatase, non-receptor type 3	8	112
PTPN4	protein tyrosine phosphatase, non-receptor type 4 (megakaryocyte)	67	8
PTPN5	protein tyrosine phosphatase, non-receptor type 5 (striatum-enriched)	0	158
PTPN6	protein tyrosine phosphatase, non-receptor type 6	25	56
PTPN7	protein tyrosine phosphatase, non-receptor type 7	-50	203
PTPN9	protein tyrosine phosphatase, non-receptor type 9	0	159
PTPNS1	protein tyrosine phosphatase, non-receptor type substrate 1	0	160
PTPNS1L2	protein tyrosine phosphatase, non-receptor type substrate 1-like 2	0	161
PTPRA	protein tyrosine phosphatase, receptor type, A	42	26
PTPRB	protein tyrosine phosphatase, receptor type, B	8	113
PTPRC	protein tyrosine phosphatase, receptor type, C	8	114
PTPRD	protein tyrosine phosphatase, receptor type, D	-17	187
PTPRE	protein tyrosine phosphatase, receptor type, E	25	57
PTPRF	protein tyrosine phosphatase, receptor type, F	0	162
PTPRG	protein tyrosine phosphatase, receptor type, G	25	58
PTPRH	protein tyrosine phosphatase, receptor type, H	0	163
PTPRJ	protein tyrosine phosphatase, receptor type, J	33	38
PTPRK	protein tyrosine phosphatase, receptor type, K	25	59
PTPRM	protein tyrosine phosphatase, receptor type, M	8	115
PTPRN	protein tyrosine phosphatase, receptor type, N	8	116
PTPRN2	protein tyrosine phosphatase, receptor type, N polypeptide 2	25	60
PTPRR	protein tyrosine phosphatase, receptor type, R	17	83
PTPRS	protein tyrosine phosphatase, receptor type, S	100	1
PTPRV	protein tyrosine phosphatase, receptor type, V	50	19
PTPRZ1	protein tyrosine phosphatase, receptor-type, Z polypeptide 1	42	27
RNGTT	RNA guanylyltransferase and 5'-phosphatase	33	39

Table 2.1 (cont'd)

SBF1	SET binding factor 1	0	164
SGPP1	sphingosine-1-phosphate phosphatase 1	0	165
SKIP	skeletal muscle and kidney enriched inositol phosphatase	-33	197
SNAP23	synaptosomal-associated protein, 23kDa	0	166
SPAP1	SH2 domain containing phosphatase anchor protein 1	42	28
TA-PP2C	T-cell activation protein phosphatase 2C	17	84
TENC1	tensin like C1 domain containing phosphatase	-8	175
TPTE	transmembrane phosphatase with tensin homology	25	61
TPTE2	transmembrane phosphoinositide 3-phosphatase and tensin homolog	25	62

FIGURES

Figure 2.1. Cell-based siRNA screen identifies PTPsigma as a modulator of PI(3)P. (**A-D**) U2OS-EGFP-2xFYVE cells transfected with control siRNA (A), Vps34 siRNA (B), starved of amino acids for 3 hours (C), or transfected with PTPRS siRNAs (D), were fixed and imaged at 60x magnification by fluorescent microscopy (green: PI(3)P, EGFP-2xFYVE; blue: nuclei). Insets show 2x magnifications of small EGFP-2xFYVE vesicles. Bars, 10 µm. (**E**) Following knockdown of phosphatases, EGFP-2xFYVE-positive punctae were scored from -100 (decreased from control cells) to +100 (increased). Phosphatases are ranked and plotted by decreasing score (left to right) with genes whose loss increased EGFP-2xFYVE fluorescence highlighted in green and whose loss caused decreases highlighted in blue. PTPRS is identified. (**F**) Mean EGFP-2xFYVE-positive punctate were quantified from cells under the conditions indicated using image analysis software. Bars represent s.e.m., $*p < 0.05$. (**G**) Phospholipids were radiolabeled in vivo, extracted, resolved by TLC, and visualized by autoradiography following transfection with control or PTPRS siRNAs. A radiolabeled PI(3)P standard was resolved adjacent to extracted lipids. (**H,I**) Endosomes were labeled by immunostaining with anti-EEA1 antibodies (H) and autophagic vesicles were labeled with anti-LC3B antibodies (I) following transfection with control or PTPRS siRNA (red: EEA1; green: LC3B; blue: nuclei). Insets show 2x magnifications of LC3-positive vesicles. Bars, 10 µm.

Figure 2.1 (cont'd)

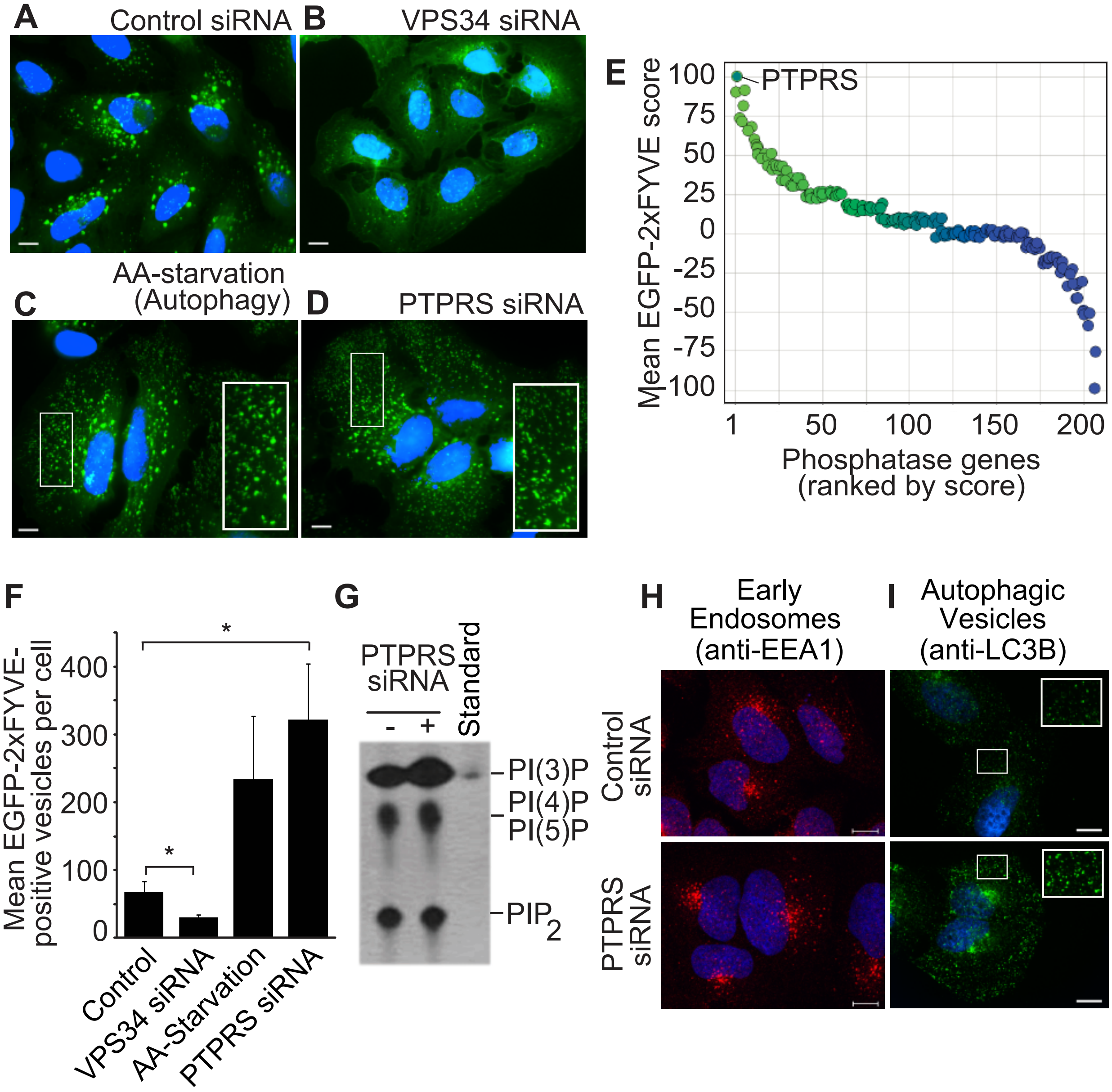

Figure 2.2. Loss of PTPsigma hyperactivates autophagy. (**A**) Atg12-positive punctae were quantified from 60x images of cells transfected with control (black) or PTPRS siRNAs (white) and treated for 1 hour with normal growth media (full nutrients) or 50 nM rapamycin. Values represent relative Atg12-positive punctae per cell following normalization to control cells cultured with full nutrients. Bars represent s.e.m., *** $p < 0.001$. (**B**) LC3-I and LC3-II were analyzed by western blot using whole cell lysates from control siRNA-transfected cells, PTPRS siRNA-transfected cells, or amino acid-starved cells. α-tubulin was probed as a loading control. (**C-H**) EGFP-LC3-positive punctae were visualized in U2OS cells transfected with control (C,E,G) or PTPRS (D,F,H) siRNAs following 2 hour treatment with normal growth media (full nutrients; C,D), 100nM bafilomycin A1 (Baf-A1; E,F), or 50 nM rapamycin and 100 nM Baf-A1 (G,H) (green: EGFP-LC3; blue: nuclei). Insets are 2x magnifications of EGFP-LC3-positive AVs. Bars, 10µm.

Figure 2.2 (cont'd)

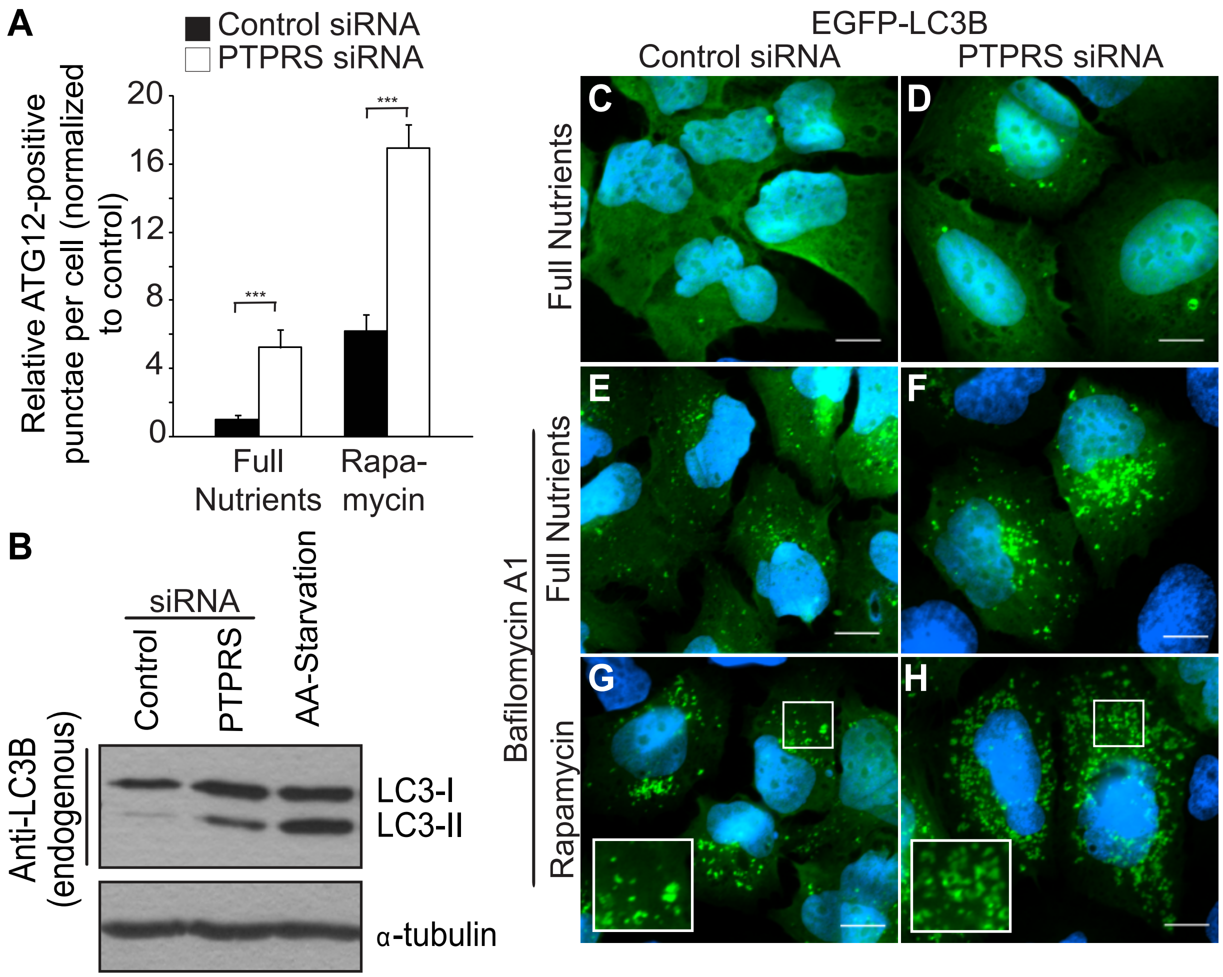

Figure 2.3. Loss of PTPsigma increases autophagic vesicle abundance as measured by electron microscopy. (**A-D**) Few autophagic vesicles (AVs) were found by transmission electron microscopy (TEM) within control cells cultured in full nutrients (A), but were abundant in chloroquine-treated (B), amino acid (AA)-starved (C), and PTPRS siRNA-transfected (D) cells. Black arrows indicate autophagic vesicles (autophagosomal or autolysosomal). White scale bars in (A-D) represent 1 µM. (**E-G**) Primary wild-type PTPRS (+/+, E) and knockout PTPRS (-/-, F) MEFs were analyzed by TEM and AVs quantified (G). AVs, defined as autophagic structures containing cytosolic components, generally degradative, were counted from 8 μm^2 sampling regions per cell. Values represent mean AVs per sampling area. Bars represent s.e.m., $^{**}p < 0.01$. White scale bars in (E-F) represent 0.5 µM.

Figure 2.3 (cont'd)

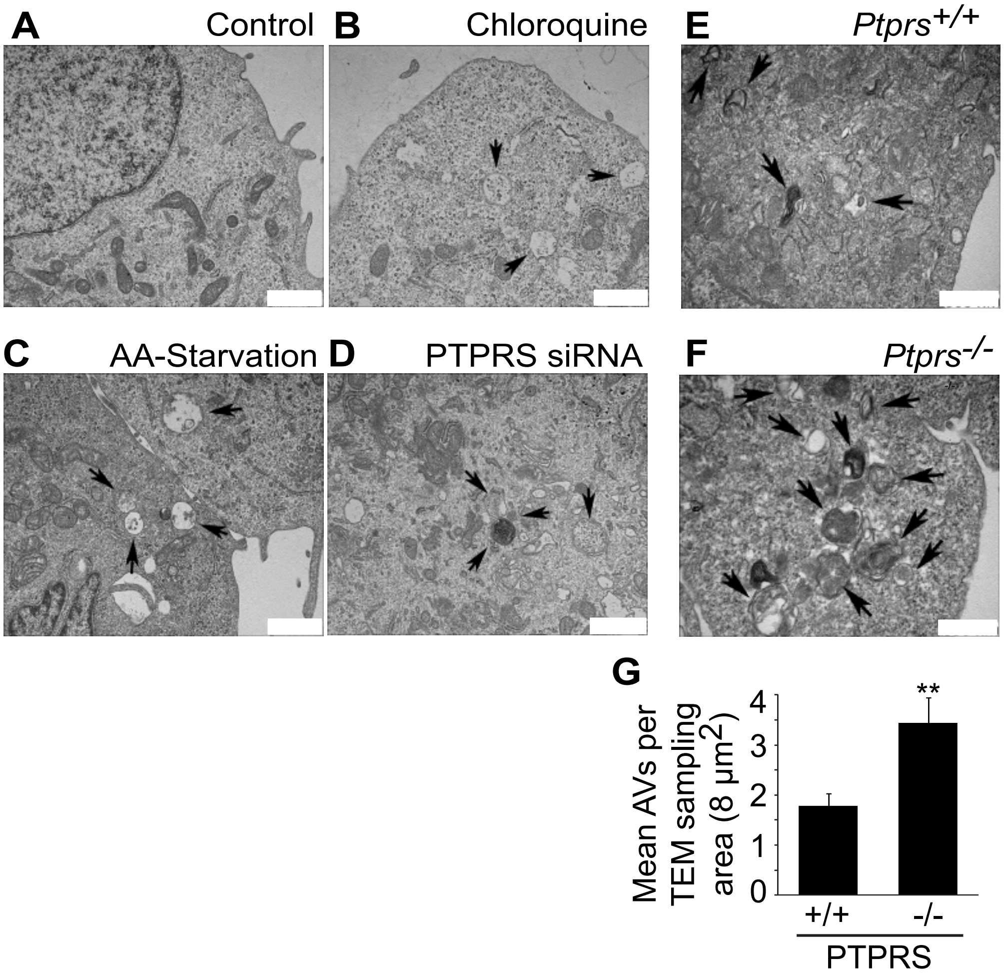

Figure 2.4. Exogenous PTPsigma localizes to PI(3)P vesicles and rescues the siRNA phenotype. (**A,B**) FL-PTPsigma was transiently expressed in U2OS-EGFP-2xFYVE cells and PI(3)P and PTPsigma imaged by fluorescent microscopy following 2 hour incubation with full nutrient media (A) or amino acid-starvation media (B) [green: PI(3)P; red: anti-PTPsigma (D1-targeted antibodies); blue: nuclei]. Insets are 2x magnifications of boxed regions. Bars, 10 µm. (**C**) U2OS-EGFP-2xFYVE cells transfected with FL-PTPsigma and amino acid-starved for 2 hours were imaged using D1-targeted PTPsigma antibodies. A Z-stack of 0.25 µm increments was captured using sequential channel acquisition and confocal microscopy, with the third slice displayed and Z-stacks through the X and Y planes shown at the border. Insets are 2x magnifications of boxed regions. Bar, 10µm (green: PI(3)P, EGFP-2xFYVE; red: anti-PTPsigma; yellow: colocalization). (**D,E**) U2OS-EGFP-2xFYVE cells were transfected with PTPRS siRNA-1 for 48 hours, after which FL-PTPsigma (which lacks the sequence targeted by siRNA-1) was introduced for an additional 24 hours. PI(3)P and PTPsigma were imaged as previously described. The presence of siRNA-induced phenotype (abundant, non-perinuclear EGFP-2xFYVE-positive vesicles; indicated by white arrows in (D)) was determined for cells expressing no, low, or high levels of FL-PTPsigma (E). Bars, 10 µm. (**F**) FL-PTPsigma-positive vesicular structures accumulate when lysosomal fusion is inhibited. U2OS cells expressing FL-PTPsigma for 24 hours were treated with 100 nM Baf-A1 in full nutrient media for 0, 15, 60, or 240 minutes and FL-PTPsigma imaged using D1-targeted PTPsigma antibodies (red). Nuclei were stained with Hoechst (blue). Bars, 10 µm.

Figure 2.4 (cont'd)

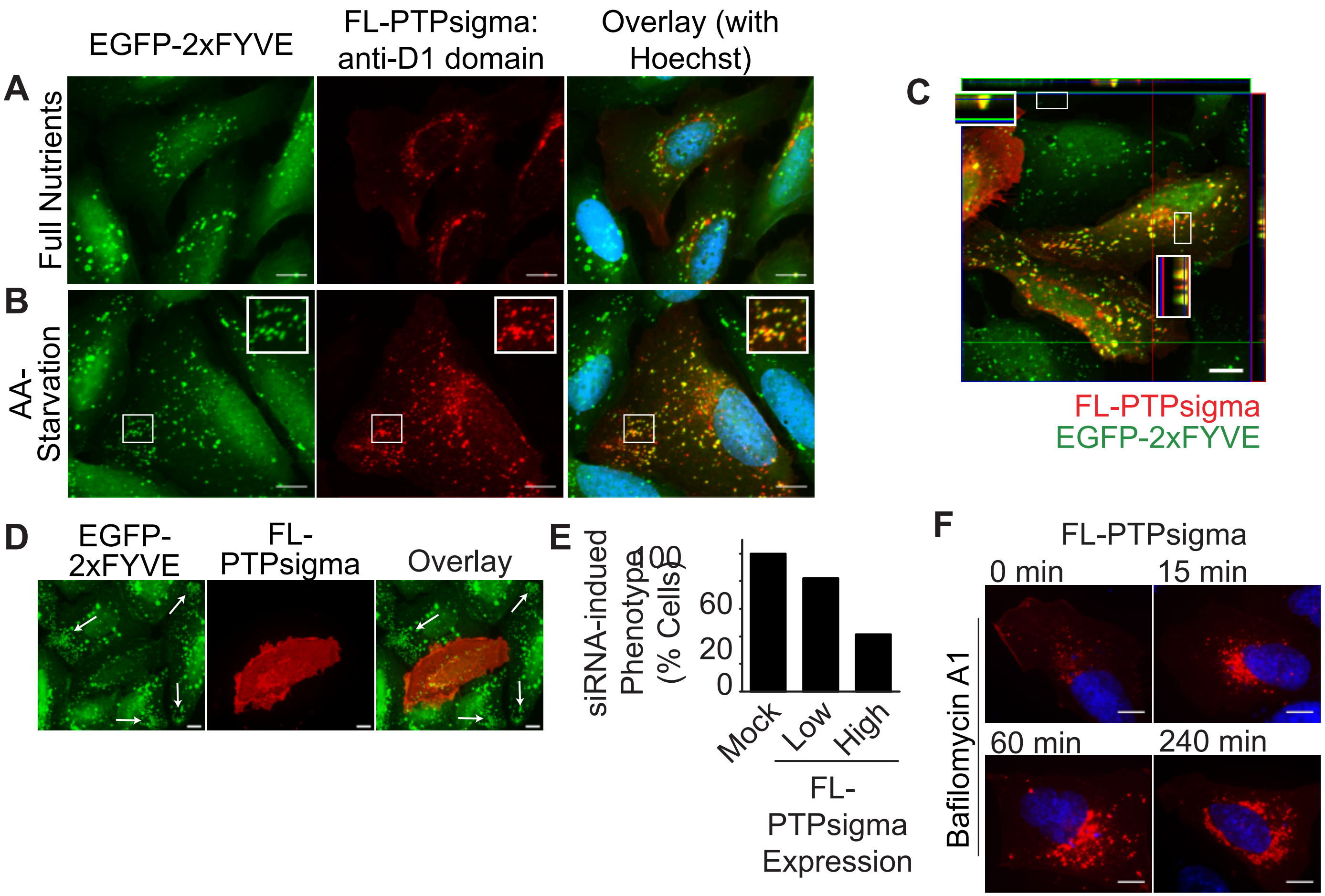

Figure 2.5. Localization of PTPsigma to vesicular structures does not require PI(3)P. (**A-B**) U2OS cells expressing FL-PTPsigma were treated with vehicle (DMSO; A) or 100 nM wortmannin (PI3K inhibitor; B) for 2 hours while cultured in amino acid-starvation media and PI(3)P and PTPsigma imaged by fluorescent microscopy [green: PI(3)P, EGFP-2xFYVE; red: anti-PTPsigma (D1-targeted antibodies); blue: nuclei]. Insets are 2x magnifications of boxed regions. Bars, 10 µm.

Figure 2.5 (cont'd)

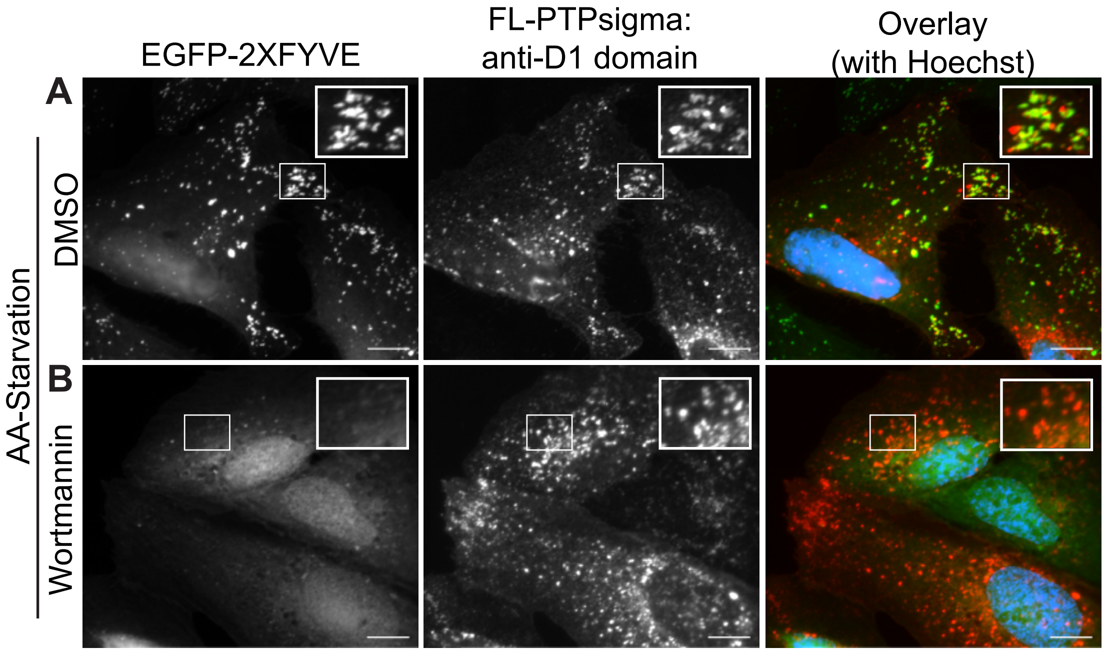

Figure 2.6. Target genes are effectively knocked down by siRNA. (**A**) Western blot analysis of whole cell extracts following transfection with control or Vps34 siRNA shows depletion of Vps34 protein levels. α-tubulin was probed as a loading control. (**B**) U2OS-EGFP-2xFYVE cells were transfected with MTMR6 siRNA, fixed, and imaged at 60x by fluorescent microscopy as in Fig. 1. A bar, 10 µm. (**C**) MTMR6 mRNA was depleted by 96% following transfection with MTMR6 siRNA for 48 hours. RNA extracted from control- or MTMR6- siRNA transfected cells was converted to cDNA and MTMR6 levels determined by qRT-PCR using gene-specific primers. Values were normalized to GAPDH. (**D-I**) U2OS-EGFP-2xFYVE cells were transfected with control (D) or PTPRS siRNA [E, siRNA-1, F, siRNA-2, G, siRNA-3, H, siRNA-4, I, siRNA-pool (1-4)] for 48 hours, fixed, and imaged by fluorescent microscopy (green: PI(3)P, EGFP-2xFYVE; blue: nuclei). Insets are 2x magnifications of boxed regions, highlighting the abundant vesicles caused by PTPRS siRNA transfection. Bars, 10 µm. (**J**) EGFP-2xFYVE punctae were quantified from cells following PTPRS knockdown with four unique siRNAs. Values represent means and bars represent s.e.m. (**K**) PTPRS mRNA knockdown following 48 hour transfection with four unique siRNAs (individually or pooled) was determined by qRT-PCR using gene-specific primers and GAPDH normalization, as described above.

Figure 2.6 (cont'd)

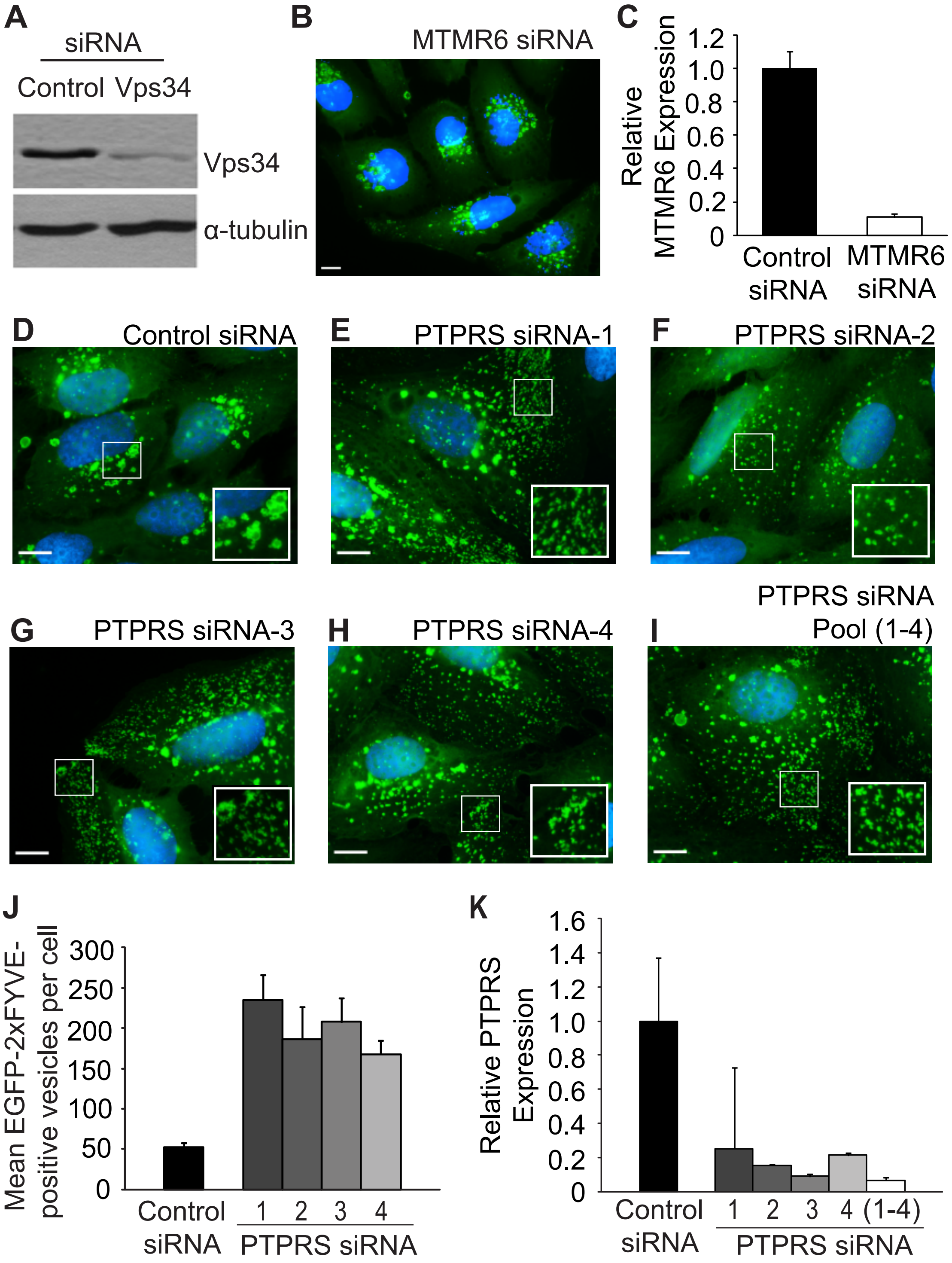

Figure 2.7. PTPsigma knockdown increases the abundance of autophagic, but not endocytic, vesicles. (**A**) U2OS cells were transfected with control or PTPRS siRNAs, fixed, and immunostained with anti-EEA1 antibodies (see Fig. 1H). EEA1-positive vesicles were quantified using image analysis software. Bars represent s.e.m. (**B**) U2OS cells transfected with control (left panels) or PTPRS (right panels) siRNAs were cultured for 1 hour with nutrient-rich medium (top panels) or 50 nM rapamycin (bottom panels). Cells were stained with anti-Atg12 antibodies and imaged by fluorescent microscopy at 60x (green: Atg12; blue: nuclei). Bars, 10 μm. (**C**) U2OS cells transfected with control or PTPRS siRNAs were cultured for 1 hour with normal growth media (full nutrients; left), 25 μM chloroquine in normal growth media (middle), or 50 nM rapamycin and 25 μM chloroquine in normal growth media (right). Cells were fixed, immunostained with anti-LC3B antibodies, and imaged by fluorescent microscopy at 60x. LC3-positive punctae were quantified images using image analysis software (black: control siRNA; white: PTPRS siRNAs). Bars represent s.e.m., $^{*}p < 0.05$, $^{**}p < 0.01$.

Figure 2.7 (cont'd)

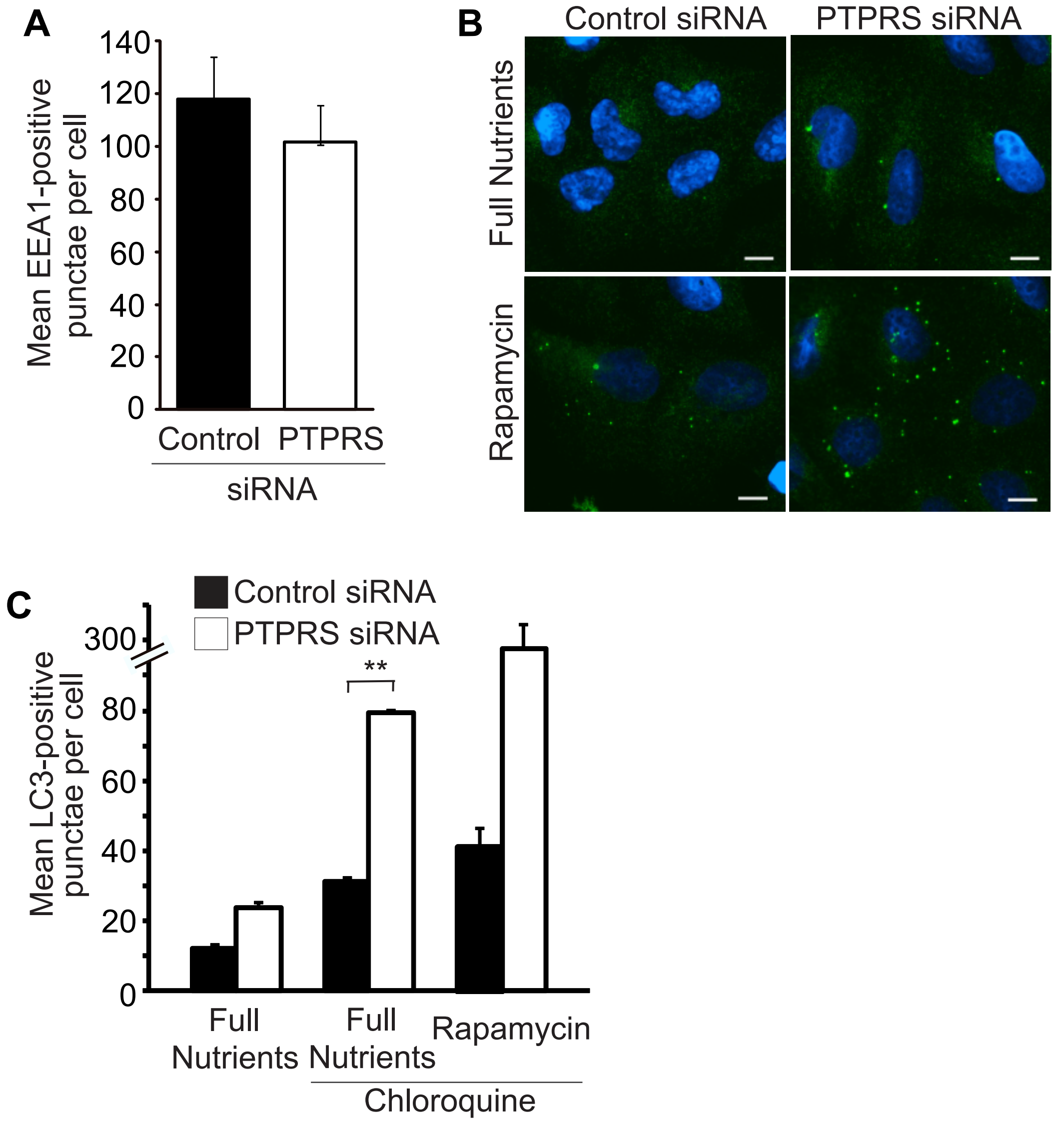

Figure 2.8. FL-PTPsigma colocalization with mRFP-LC3 and mock control for FL-PTPsigma immunofluorescence. (**A**) U2OS-EGFP-2xFYVE cells were mock transfected (with transfection reagent but no DNA) for 24 hours, stained with PTPsigma (anti-D1) antibodies, and imaged as in Fig. 4A-C, Fig. 5, and (B). Absence of signal in the red channel demonstrates specificity of FL-PTPsigma expression captured in the above figures [green: PI(3)P; red: anti-PTPsigma (D1-targeted antibodies); blue: nuclei]. Bars, 10 µm. (**B**) FL-PTPsigma was transiently expressed in U2OS-mRFP-LC3 cells and LC3 and PTPsigma imaged by fluorescent microscopy following 2 hour incubation with full nutrient media (top panels) or amino acid-starvation media (lower panels) [red: mRFP-LC3; green: PTPsigma (D1-targeted antibodies); blue: nuclei]. Insets are 2x magnifications of boxed regions. White arrows indicated punctae positive for both PTPsigma and LC3.

Figure 2.8 (cont'd)

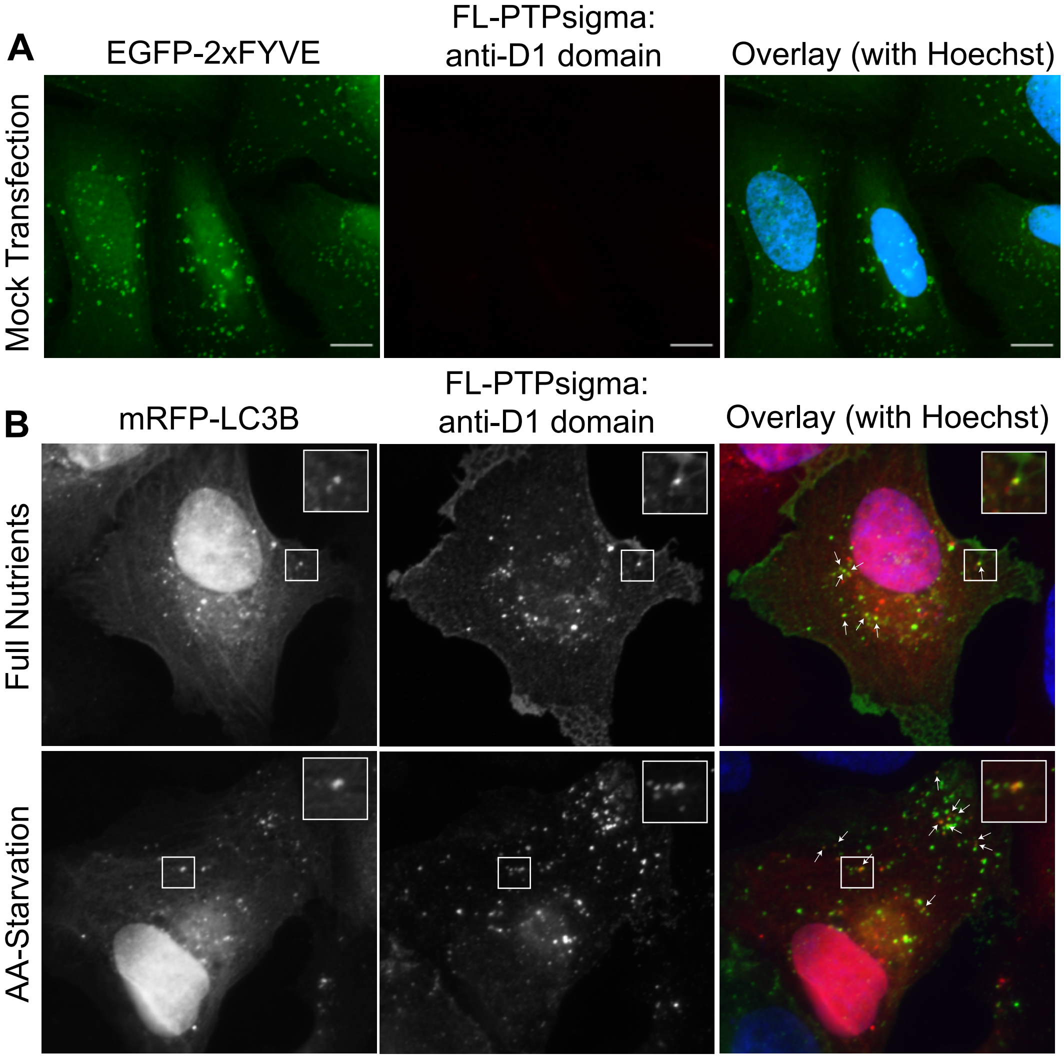

Figure 2.9. PTPsigma dephosphorylates phosphotyrosine, but not PI(3)P, in vitro. (**A**) Recombinant GST-fusions of PTP1B (left), PTPsigma (middle) and MTMR6 (right) were incubated with a phosphotyrosine peptide at the indicated concentrations for 15 minutes at 37°C and released phosphates measured by malachite green quenching and 650 nm absorbance. (**B**) Recombinant GST-fusions of PTP1B (left), PTPsigma (middle) and MTMR6 (right) were incubated with water-soluble PI(3)P substrate at the indicated concentrations and released phosphates measured by malachite green quenching and 650 nm absorbance. Bars represent s.d.m.

Figure 2.9 (cont'd)

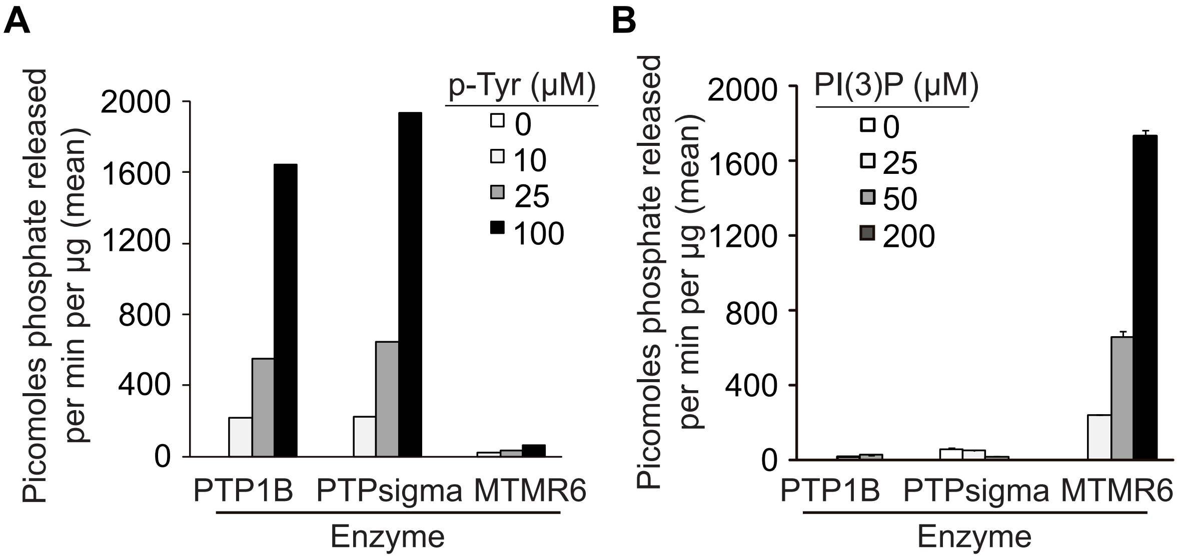

CHAPTER 2 SECTION 2

A potential role for PTPsigma as a Vps34 complex effector and the discovery of autophagy-relevant processing events

Martin KR, MacKeigan JP

ABSTRACT

Phosphatidylinositol-3-phosphate (PI(3)P) is an intracellular signaling lipid required for dynamic membrane trafficking pathways including endocytosis and autophagy(Funderburk, Wang et al. 2010). As such, it is essential that PI(3)P be generated and maintained on membranes in a spatially and temporally controlled manner. In a search for phosphatases which contribute to this exquisite regulation, we recently reported that PTPsigma, a dual-domain protein tyrosine phosphatase (PTP), functions as a negative regulator of PI(3)P signaling and autophagy (Martin, Xu et al. 2011). Following this initial identification, several important issues remained concerning the regulation and function of this phosphatase. Specifically, we found that loss of PTPsigma increases PI(3)P-positive vesicle abundance and enhances autophagy; however, the mechanism underlying this loss-of-function phenotype was not established. Further, we determined that PTPsigma localizes to PI(3)P-positive vesicles in a dynamic manner; however, potential processing events responsible for targeting this receptor-like PTP from the cell surface to its vesicular location were not investigated.

Here, we address these key outstanding issues to uncover important features of PTPsigma function and regulation as it pertains to PI(3)P signaling. First, we determine that loss of PTPsigma increases the catalytic activity of Vps34, the lipid kinase which generates PI(3)P, and further, that PTPsigma is capable of interacting with Vps34 and one of its binding partners, Rubicon. Second, loss of PTPsigma induces changes in tyrosine phosphorylation detected in the Vps34 complex as well as whole cell extracts. Future identification of the targets for this phosphorylation will likely reveal substrates of PTPsigma that mediate its role in PI(3)P signaling. Lastly, we detect the formation of distinct PTPsigma processing fragments during

normal growth conditions as well as upon autophagy induction. We discuss potential mechanisms by which PTPsigma may function to downregulate PI(3)P and the proteolytic processing events which control its internalization and presence on PI(3)P membranes.

INTRODUCTION

Balanced PI(3)P signaling is crucial to maintain homeostatic function of both endocytosis and autophagy, two convergent membrane-trafficking processes. Vps34, the sole member of the mammalian class III phosphoinositide-3-kinase (PI3K) family, produces PI(3)P and has been found to reside within large complexes of regulatory proteins which control its function in these processes (Sun, Fan et al. 2008; Matsunaga, Saitoh et al. 2009; Zhong, Wang et al. 2009). After formation, turnover of PI(3)P through dephosphorylation can be executed by myotubularin-related lipid phosphatases (Blondeau, Laporte et al. 2000; Vergne, Roberts et al. 2009; Taguchi-Atarashi, Hamasaki et al. 2010). In addition to these regulatory mechanisms, we hypothesized that novel protein phosphatases exist which control PI(3)P, especially through downregulation of that autophagic machinery. To explore this hypothesis, we performed a cell-based screen of human phosphatase genes using RNA interference and found that loss of PTPsigma hyperactivates PI(3)P and autophagy (Martin, Xu et al. 2011).

In our initial report, we showed that PTPsigma resides on PI(3)P membranes in a dynamic and nutrient-responsive manner. We also observed through an RNAi rescue experiment that overexpressed PTPsigma can reduce cellular PI(3)P levels. Although we first hypothesized that PTPsigma may directly dephosphorylate PI(3)P, after extensive investigation, we could not detect robust lipid phosphatase activity *in vitro*. Additionally, when we depleted cells of PI(3)P (by inhibiting Vps34), the dynamic localization of PTPsigma to PI(3)P-positive membranes was not affected, suggesting that its vesicular presence occurs independently of this lipid. These findings led us to postulate that PTPsigma has protein substrates involved in PI(3)P signaling and that alterations of their activity upon PTPsigma knockdown explain this loss-of-function phenotype. Because of the robust PI(3)P production in the absence of PTPsigma and evidence for tyrosine phosphorylation of Vps34 and several of its binding partners, we hypothesized that PTPsigma may function as a Vps34-complex effector. In this study, we explore this hypothesis and report our findings from the following aims: (1) to determine if PTPsigma has the ability to interact with proteins comprising Vps34 complexes; (2) to establish the control, if any, PTPsigma exerts on Vps34 catalytic activity; and (3) to identify phosphorylation changes which occur upon PTPsigma knockdown. Indeed, we found that PTPsigma is capable of interacting with Vps34 and its endocytic binding partner, Rubicon. Further, loss of PTPsigma enhanced phosphorylation of unknown targets associated with Vps34 and increased lipid kinase activity as measured *in vitro*.

An additional question arising from our initial identification of PTPsigma as a regulator of autophagy concerns the processing of PTPsigma. As a cell-surface receptor-like molecule, PTPsigma is capable of undergoing defined proteolytic processing whereby its large ectodomain is shed and a membrane-tethered C-terminal fragment (CTF) is internalized inside the cell (Aicher, Lerch et al. 1997). LAR, a close relative of PTPsigma, has been characterized to undergo an additional cleavage event, mediated by gamma secretase and presenilin, which results in the formation of an intracellular domain (ICD) which is liberated from the membrane (Ruhe, Streit et al. 2006; Haapasalo, Kim et al. 2007). Based on close homology to LAR, it is possible that PTPsigma also forms an ICD although to our knowledge, this has yet to be studied. We raised the possibility that processing events may be regulated to control the function of PTPsigma in autophagy. Specifically, we hypothesized that PTPsigma undergoes distinct processing events which lead to the formation of a CTF or ICD and it is in this form that intracellular PTPsigma controls PI(3)P signaling. We determined that under normal growth conditions (that is, in full nutrients), an abundant PTPsigma P-subunit is processed into a CTF which accumulates kinetically upon lysosomal inhibition. This suggests a continuous formation and turnover of the CTF within the lysosome. Intriguingly, additional processing occurs during starvation-induced autophagy to produce a potential PTPsigma ICD; however, this fragment does not appear to be a major target of the lysosome. The lysosomal turnover of a CTF and further nutrient-responsive processing represent novel findings for PTPsigma that may be important for regulation of its function in PI(3)P signaling.

RESULTS

PTPsigma and Vps34 can co-immunoprecipitate with one another

Loss of PTPsigma appears to hyperactivate autophagy from a very early step (PI(3)P). Thus, we filtered a publically available database, PhosphoSite Plus, for evidence of tyrosine phosphorylation on proteins functioning early in autophagy (www.phosphosite.org). In our search of proteins including Vps34 and its key binding partners, the ULK1 complex, and autophagic PI(3)P effectors, we found six potentially phosphorylated tyrosine residues (Table 2.2). Intriguingly, all but one of these were found on Vps34-related proteins. From this finding, together with the robust effect loss of PTPsigma exerts on PI(3)P and the localization of PTPsigma on membranes enriched in PI(3)P, we postulated that PTPsigma may regulate Vps34 or an associated protein.

To determine if PTPsigma could interact with Vps34, we used a combination of exogenous and endogenous protein detection in co-immunoprecipitation (co-IP) experiments. PTPsigma expression is low and undetectable at the endogenous protein level by immunoblot using currently available resources. Endogenous Vps34 can be readily detected, however, antibodies which can immunoprecipitate Vps34 are not available. Accordingly, we began by immunoprecipitating exogenously expressed V5-PTPsigma-CTF (residues including and C-terminal to the transmembrane domain) with a substrate trapping mutation in the D1 active site (C1589S) from 293FT cells. We found that under normal growth conditions (that is, full serum, glucose, and amino acids), endogenous Vps34 was pulled down in the precipitate (Figure 2.10A). Interestingly, this interaction was not apparent after 1 hour amino acid starvation (autophagy) (Figure 2.10A). To see if we could detect this interaction in the reverse orientation, we expressed and immunoprecipitated V5-Vps34 from 293FT cells which co-expressed its regulatory proteins, Vps15 and Beclin1, as well as untagged full-length PTPsigma. When probed with a D1-targeted antibody, PTPsigma was readily detected in all Vps34 immunoprecipitates (Figure 2.10B). While the substrate-trapping mutation appeared to enhance the interaction, it cannot be excluded that expression levels contributed to this difference. Importantly, substitution of the putatively phosphorylated tyrosine, Y517, with an alanine, did not alter the interaction with PTPsigma (Figure 2.10B). Taken together, these data suggest that PTPsigma and Vps34 are capable of interacting together in cells and this interaction does not depend on phosphorylation of Vps34 at Y517.

PTPsigma and Rubicon may interact in cells

In an effort to further elucidate the potential interaction with Vps34, we tested the ability of PTPsigma to interact with several components of the Vps34 complex (Vps15, Beclin1, UVRAG, and Rubicon) using a similar co-IP approach. We discovered that PTPsigma was capable of interacting with Rubicon independent of Vps34 overexpression, although this did not appear to be as robust as the interaction with Vps34 (Figure 2.10C). Rubicon is part of the Vps34 complex that localizes to endomembranes and functions along the endocytic system (Matsunaga, Saitoh et al. 2009; Zhong, Wang et al. 2009). It is unique among the Vps34 interactors in that rather than supporting the function of Vps34, it suppresses its activity and downregulates the maturation of endosomes and autophagosomes (Matsunaga, Saitoh et al. 2009; Zhong, Wang et al. 2009). Given this interaction from cell lysates, we analyzed the location of Rubicon and PTPsigma by fluorescent microscopy and found that their subcellular localization largely overlapped (Figure 2.10D). Specifically, both proteins localize to peripheral vesicles as well as perinuclear membranous networks (Figure 2.10D).

Loss of PTPsigma is characterized by specific cellular changes in tyrosine phosphorylation

After establishing the potential for PTPsigma to reside within a Vps34 complex, we sought to address if PTPsigma controls the phosphorylation of these proteins. To this end, U2OS cells were transfected with control siRNAs or siRNAs targeting PTPsigma for 48 hours (this knockdown condition results in a substantial increase in cellular PI(3)P and enhances autophagy; See Chapter 2 Section 1). For the final 24 hours of knockdown, we exogenously expressed the Vps34 core complex (Vps34-Vps15-Beclin1). After cells were lysed and Vps34-immunoprecipitates collected, we assayed tyrosine phosphorylation by immunoblot. Remarkably, we discovered phosphorylation of a prominent band near 100 kDa which was only present in the absence of PTPsigma (Figure 2.11A). Acute treatment of control cells with the pan PTP inhibitor, pervanadate, prior to lysis did not generate phosphorylation of this band suggesting it is generated through a more time-intensive process (Figure 2.11A). The molecular weight of this band does not correlate with any of the three overexpressed Vps34-complex proteins but rather, it may represent an endogenous protein interacting and precipitating with this complex. A protein of slightly smaller size appears to also be phosphorylated and incorporated into this complex although its phosphorylation state was not substantially changed by loss of PTPsigma (Figure 2.11A).

We chose to complement this finding with an unbiased approach to observe global changes in phosphorylation of proteins elicited by PTPsigma knockdown. We once again transfected U2OS cells with control or PTPsigma siRNAs for 48 hours. Following, the lysates were immunoprecipitated with phospho-tyrosine-specific antibodies and captured proteins were probed by immunoblot using the same phospho-tyrosine antibody. We discovered at least three bands with increased phosphorylation in the absence of PTPsigma, each corresponding to a unique molecular weight (Figure 2.11B). A band just beneath the 115 kDa marker showed considerable phosphorylation in cells transfected with PTPsigma siRNAs although it was also basally phosphorylated in the control cells. A faint band close to the 180 kDa marker was phosphorylated in PTPsigma-depleted cells but apparently not in the control. Lastly, and relevant to the Vps34 complex phospho-analysis, a phosphorylated band near 100 kDa was present only upon PTPsigma knockdown (Figure 2.11B). The key next step is to use mass spectrometry to identify these phosphorylated proteins.

Loss of PTPsigma increases the *in vitro* kinase activity of Vps34

Based on the observation that loss of PTPsigma drives changes in phosphorylation and these alterations may be related to the Vps34-complexes, we next determined whether PTPsigma could affect the kinase activity of Vps34 *in vitro.* It has been reported that full activity of Vps34 *in vitro* requires immunoprecipitation from cells co-expressing functional binding partners (Backer 2008). We verified that three exogenous proteins comprising the Vps34 core complex (V5-Vps34, Flag-Vps15, and Beclin1) were forming a functional complex in cells. First, a series of co-IP experiments revealed that Vps34 interacts with both Vps15 and Beclin1 when expressed in pairs and also, when all three are expressed together (Figure 2.12A). Further, we tested the ability of immunoprecipitated Vps34 to catalyze the production of PI(3)P *in vitro* using synthetic phosphatidylinositol substrate and radiolabeled ATP. Consistent with the previous data, we found that co-expression of binding partners enhanced the catalytic activity of Vps34 (Figure

2.12B). A portion of this increase may be attributed to more stable expression of Vps34 promoted by co-expression of Vps15 and/or Beclin1 (Figure 2.12A). When this activity was tested from cells transfected with PTPsigma siRNAs, an increase of approximately 60% was observed (Figure 2.12C). When activity was measured from cells expressing a larger Vps34 complex which included the core, Rubicon, and UVRAG, PTPsigma knockdown similarly increased kinase activity, by approximately 75% (Figure 2.12C). Although not shown here, the increase in activity is likely not due to increased expression as a previous experiment under the same general conditions showed similar expression and immunoprecipitation of the Vps34 complex from control or PTPRS siRNA-transfected cells (Figure 2.11A).

PTPsigma is processed to a CTF and degraded in the lysosome

This revelation that PTPsigma may function as an effector of the Vps34-complex, together with prior knowledge that PTPsigma localizes to PI(3)P-vesicles in a dynamic manner, led us to wonder whether its function in this axis is characterized by unique proteolytic processing events. PTPsigma has been previously reported to shed its ectodomain and internalize from the cell surface as a membrane-bound C-terminal fragment (CTF) (Aicher, Lerch et al. 1997). The intracellular destination of this CTF, and any further processing to a soluble intracellular domain (ICD), has not been studied. We aimed to determine if PTPsigma exists as a CTF and/or ICD in our cell model and if nutrient-starvation triggers proteolytic changes in PTPsigma, much like it triggers a redistribution to smaller, peripheral vesicles.

To this end, we expressed full-length untagged exogenous PTPsigma in U2OS cells and used immunoblotting to determine the presence of all potential fragments– the pro-subunit, P-subunit, CTF, and ICD – each distinguished by a unique predicted molecular weight of ~170 kDa, 85 kDa, 76 kDa, and 72 kDa, respectively. Because processing into each of these forms occurs upstream of the D1 domain, we used a D1-directed antibody for detection. First, we analyzed basal processing of PTPsigma which occurs during normal growth conditions. We found that PTPsigma exists predominantly as a full-length pro-subunit and as a cell surface-expressed P-subunit (Figure 2.13A). When lysosomes were inhibited with bafilomycin A1 (BafA1), a smaller band of a molecular weight consistent with a CTF appeared within 15 to 30 minutes and accumulated kinetically (Figure 2.13A). To determine if this fragment was in fact processed from the P-subunit, we inhibited extracellular metalloproteases responsible for P-subunit-to-CTF processing using a small molecule inhibitor, Batimastat (Ruhe, Streit et al. 2006). In contrast to the vehicle control, cells pre-treated with Batimastat failed to produce this fragment, supporting its identity as a processed P-subunit fragment, likely a CTF (Figure 2.13B).

PTPsigma is further processed during starvation-induced autophagy

To determine whether PTPsigma processing is altered during autophagy induction, we kinetically starved cells of amino acids and probed for PTPsigma fragments. Starvation induced the generation of a novel PTPsigma fragment of lower molecular weight than the putative CTF (Figure 2.13C). When cells were concurrently starved of amino acids and treated with BafA1, the putative CTF accumulated once again, but the smaller fragment did so only slightly, if at all (Figure 2.13C). This suggests that although the membrane-bound CTF is degraded in the lysosome, this novel fragment is likely not regulated in the same manner.

DISCUSSION

In sum, the results of experiments summarized here begin to address some of the questions raised in our initial report that PTPsigma suppresses autophagy. First, through co-IPs, we detected interactions between PTPsigma and both Vps34 and Rubicon. While it will need to be further characterized and verified endogenously, it appears that a Vps34-PTPsigma interaction may be relevant during normal growth conditions but relieved during autophagy induction. This is an intriguing notion given that the robust PI(3)P phenotype elicited by PTPsigma knockdown was initially discovered and subsequently characterized in cells cultured in full nutrient media. Accordingly, if PTPsigma in fact functions as a negative regulator of Vps34, we predict it exerts this control during normal growth because upon depletion, cells exhibit inappropriately active PI(3)P signaling and autophagy.

In this light, normal expression of PTPsigma could be viewed as a brake pedal in Vps34 activity, functioning in a similar role to Rubicon (Matsunaga, Saitoh et al. 2009; Zhong, Wang et al. 2009). This function could have great purpose given the bimodal manner in which autophagy contributes to cell fate (Levine 2007). At one extreme, a cell defective in autophagy is rendered susceptible to stress and starvation and more prone to cell death induced by these. Conversely, a cell which engages autophagy in excess is likely to suffer a premature death resulting from detrimental degradation of vital cytosolic content (Levine 2007 Nature). Consequently, it would benefit a cell to have checkpoints in place, such as PTPsigma suppression of PI(3)P production, which would contribute to a homeostatic level of autophagy.

In agreement with an inhibitory function, PTPsigma knockdown appears to increase the catalytic activity of Vps34 as measured *in vitro*. This enhanced kinase activity likely explains, at least in part, the abundance of PI(3)P previously observed under these same conditions. Intriguingly, we observed an endogenous protein of approximately 100 kDa which co-precipitated with exogenous Vps34 and was tyrosine-phosphorylated in response to PTPsigma knockdown. While the identity of the phospho-protein is unknown, it is an exciting possibility that PTPsigma exerts control over Vps34 through its regulation. Future studies will seek to identify this protein and determine whether it is directly dephosphorylated by PTPsigma. If so, the contribution of its phosphorylation status to Vps34 function will be investigated.

In contrast to the Vps34 interaction, the ability of PTPsigma to precipitate Rubicon was relatively weak. Despite this, their subcellular localization on endomembranes was in close alignment, suggesting they function within the same subcellular compartment. Rubicon has been found to localize to membranes of both early and late endocytic compartments, including those enriched with PI(3)P (Sun, Fan et al. 2008; Matsunaga, Saitoh et al. 2009; Zhong, Wang et al. 2009; Sun, Zhang et al. 2011). This suggests that the PI(3)P-positive vesicles where we observe PTPsigma are likely also endocytic in origin. The phenotype reported for RNAi-mediated knockdown of Rubicon was very similar to that which we observed for PTPsigma knockdown and included an increased abundance and flux of autophagic vesicles (Matsunaga, Saitoh et al. 2009; Zhong, Wang et al. 2009). Because both of these proteins downregulate autophagy, localize to the same vesicles, and can interact to some degree, it is possible that PTPsigma and Rubicon cooperate with one another to suppress Vps34-PI(3)P signaling. Interestingly, Rubicon has at least one potentially phosphorylated tyrosine residue and is 109 kDa in size, similar to that of the unidentified phosphoprotein discussed above, raising the possibility that Rubicon is a substrate of PTPsigma. This hypothesis remains to be tested.

We found that PTPsigma was processed from its P-subunit into a putative CTF. This processing occurs under normal growth conditions and results in CTF targeting and turnover in the lysosome. Further, we presented evidence that PTPsigma is processed into a C-terminal fragment smaller than the CTF during starvation-induced autophagy. This fragment does not appear to be targeted to the lysosome and while it is logical to assume it is an ICD, its molecular weight is smaller than that reported for a LAR ICD (Haapasalo, Kim et al. 2007). PTPsigma does in fact have residues within and just C-terminal to its transmembrane domain similar to those in Notch that are required for gamma-secretase-mediated ICD formation (Gupta-Rossi, Six et al. 2004). However, mutation of the analogous residues in LAR did not impair the ability of gamma secretase to generate an ICD so they may not be critical for a PTPsigma-ICD either (Haapasalo, Kim et al. 2007). If this detected fragment is in fact an ICD, it may be generated through a unique mechanism or from a specific site downstream of the transmembrane domain, resulting in a smaller size. Regardless, because PTPsigma exerts its inhibitory effect on autophagy in the presence of nutrients, it is likely that the CTF is the fragment relevant to PI(3)P suppression. The fact that the CTF is membrane-bound and turned over in the lysosome supports a model where PTPsigma is processed and internalized from the cell surface as part of the endocytic pathway. It would likely be during this trafficking that PTPsigma resides on PI(3)P-positive endocytic vesicles and suppresses Vps34 signaling to impede the maturation of both endosomal and autophagic vesicles, akin to Rubicon.

MATERIALS AND METHODS

Co-immunoprecipitation experiments

10 cm dishes of 80% confluent U2OS or 293FT cells were transfected with the indicated plasmids for 24 hours prior to cell lysis using a 1:3 µg DNA to µl FuGeneHD (Roche) ratio in Optimem and McCoy's 5A (U2OS) or DMEM (293FT) supplemented with 10% FBS. Cells were lysed under conditions previously described in Chapter 2 Section 1. V5-fusions were precipitated from cleared lysates (normalized for total protein by Bradford assay) using V5 antibodies (Invitrogen) for 2 to 24 hours at 4°C. Protein G was added for the final 1h at 4°C. Beads were collected and washed three times with lysis buffer. After the final wash, beads were resuspended in 2x sample loading buffer and resolved by SDS-PAGE. Western blotting was performed as described in Chapter 2 Section 1 using the antibodies indicated in figures. Antibodies used included Vps15 (Abcam), Beclin1 (BD), V5 (Invitrogen), GFP (Abcam), Vps34 (Invitrogen), PTPsigma (kind gift from Michel Tremblay), and phosphotyrosine (CST).

Phosphotyrosine analyses

Pervanadate was prepared for 10 min in the dark from sodium orthovanadate and hydrogen peroxide in 1xPBS and used on cells at a concentration of 100 µM in normal media for 30 min prior to cell lysis. For Figure 2.11A, U2OS cells expressing Vps34 complexes were immunoprecipitated with anti-V5 antibodies and proteins captured were probed by western blot with anti-phosphotyrosine antibodies. For Figure 2.11B, U2OS cells transfected with PTPsigma or control siRNAs for 48 hours (as described in Chapter 2 Section 1) were lysed, immunoprecipitated with anti-phosphotyrosine antibodies, and proteins captured were probed by western blot with anti-phosphotyrosine.

PTPsigma and GFP-Rubicon fluorescent microscopy

Fluorescent microscopy of exogenously expressed proteins was performed as described in Chapter 2 Section 1. Briefly, U2OS cells were co-transfected with EGFP-Rubicon (Addgene plasmid 28022; Sun et al 2011 JBC) and full-length PTPsigma (see Chapter 2 Section 2) for 24 hours. Cells were stained with anti-PTPsigma D1 antibodies and AF546-conjugated secondary antibodies (red channel). Cells were imaged with an 100x/oil objective using a Nikon Ti Eclipse fluorescent microscope.

PTPsigma processing experiments

U2OS cells were transfected with full-length PTPsigma (see Chapter 2 Section 2 details) for 24 hours. Following, cells were treated with BafA1 (100 nM) and/or starved of amino acids (see Chapter 2 Section 1 for media composition) for the indicated times. Cells were lysed, protein content normalized, and lysates probed by western blot with anti-PTPsigma D1 targeted antibodies. In Figure 2.13B, cells were pre-treated with vehicle (DMSO) or batimastat (Tocris, 10 µM) for 4 hours then treated with BafA1 (100 nM) for the indicated times.

Vps34 *in vitro* kinase assays

Vps34 core complex proteins were cloned in full-length form into pRK7. Vps34 (NM_002647.2) was fused with an N-terminal V5 tag introduced in the forward PCR primer. Vps15 (BC110318.1) was fused with an N-terminal Flag tag introduced in the forward primer. Beclin1 (BC010276.1) was cloned without an epitope tag.

293FT cells were co-transfected with the Vps34 core complex (Vps15, Beclin1, and Vps34) with or without EGFP-Rubicon and EGFP-UVRAG (Addgene plasmid 24296; (Itakura, Kishi et al. 2008). Vps34 was immunoprecipitated as described above using V5 antibodies. Beads were either collected and probed for complex proteins by western blot or washed and subjected to *in vitro* kinase assays.

For kinase assays, beads were washed in 1% NP40 in 1xPBS, 100 mM Tris-HCl pH 7.5 + 500 mM lithium chloride, and TNE (50 mM Tris-HCl pH 7.5, 140 mM sodium chloride, 5 mM EDTA). After the final wash, beads were resuspended in 50 µl Vps34 kinase buffer (50 mM Tris-HCl pH 7.5, 150 mM sodium chloride), 100 µM short chain phosphatidylinositol (diC8-PtdIns), and 10 mM manganese chloride. After a 10 min pre-incubation at room temperature, 10 to 20 µCi ^{32}P-ATP was added with 50 µM non-labeled ATP. Reactions proceeded at room temperature for 25 min while shaking, stopped with 80 µl 1N HCl, and lipids extracted using 160 µl chloroform:methanol (1:1). Lipid phases were spotted on silica TLC plate s(Fisher) and resolved for 2 to 4 hours in $CHCl_3$:MeOH:NH_4OH:H_2O (86:76:10:14). Plates were exposed to film (4 hours at -80°C and 3 hours at room temperature) for autoradiography (Figure 2.12B) or quantified on the phosphorimager (Figure 2.12B, Figure 2.12C).

TABLES

Table 2.2. Potentially phosphorylated tyrosine residues of the early autophagic machinery. The publically available database of post-translational protein modifications, PhosphoSite Plus, was filtered for proteins involved in early autophagy (grouped by Vps34 and key binding partners, ULK1 complex proteins, and autophagic PI(3)P effectors below). Predicted molecular weights (also obtained from PhosphoSite Plus) and tyrosine residues with evidence of phosphorylation, if any, are listed in the right-hand column. “None” indicates that no phosphorylated residues have been identified and reported. Original citations for mass spectrometry data identifying these residues are included in the right column.

Table 2.2 (cont'd)

Protein	**Molecular Weight (kDa)**	**pY site**	**Reference(s)**
VPS34 (PIK3C3)	102	Y517[1]	Imami, Sugiyama et al. 2008
VPS15 (PIK3CR4)	153	Y673[2]	Brill, Xiong et al. 2009
BECLIN1	52	None	---
UVRAG	78	Y516[3,4]	Oppermann, Gnad et al. 2009; CST Curated Dataset 4609, 2008
RUBICON	109	Y449[5-8]	CST Curated Dataset 871, 2005; CST Curated Datasets 1648, 1658, 1652, and 1655, 2006; CST Curated Dataset 2484, 2658, 2007; CST Curated Dataset 3766, 2008
ATG14L (BARKOR)	55	Y37[9]	Iliuk, Martin et al. 2010
ULK1	113	None	---
ULK2	113	Y331[10]	Li, Ren et al. 2009
ATG13	57	None	---
FIP200 (RB1CC1)	183	None	---
DFCP1 (ZFYVE1)	87	None	---
WIPI1 (ATG18)	49	None	---
WIPI2	49	None	---

FIGURES

Figure 2.10. PTPsigma potentially functions as a Vps34 effector. (A-C) PTPsigma is capable of interacting with Vps34 and Rubicon. (A) 293FT cells were transfected with V5-PTPsigma-CTF C1589S mutant and incubated for 1 hour in the presence (+) or absence (-) of amino acids and lysates immunoprecipitated (IPed) with V5 antibodies. Whole cell lysates (input) and immunoprecipitates (IP) were probed by immunoblot (IB) with V5 and Vps34 antibodies. (B) 293FT cells were transfected with a wild-type (WT) or Y517A mutant (Y/A; generated by site-directed mutagenesis) V5-Vps34 (along with Flag-Vps15 and untagged Beclin1) and full-length wild-type (WT) PTPsigma (FL-PTPsigma) or PTPsigma with a double C1589S/C1880S mutation (C/S). Lysates were IPed with V5 antibodies and probed by western blot with V5 and D1-targeting PTPsigma antibodies. (C) U2OS cells expressing GFP-Rubicon were co-transfected with wild-type (WT) or C1589S-mutated (C/S) V5-PTPsigma-CTF and lysates IPed with V5 antibodies. Whole cell lysates (input) and immunoprecipitates were probed by immunoblot with GFP and V5 antibodies. **(D)** U2OS cells were co-transfected with FL-PTPsigma and GFP-Rubicon and localization imaged at 100x magnification by fluorescent microscopy. FL-PTPsigma was detected with D1-targeted antibodies and AF-546 secondary antibodies. Nuclei stained with Hoechst. Insets represent 2x magnifications of boxed regions.

Figure 2.10 (cont'd)

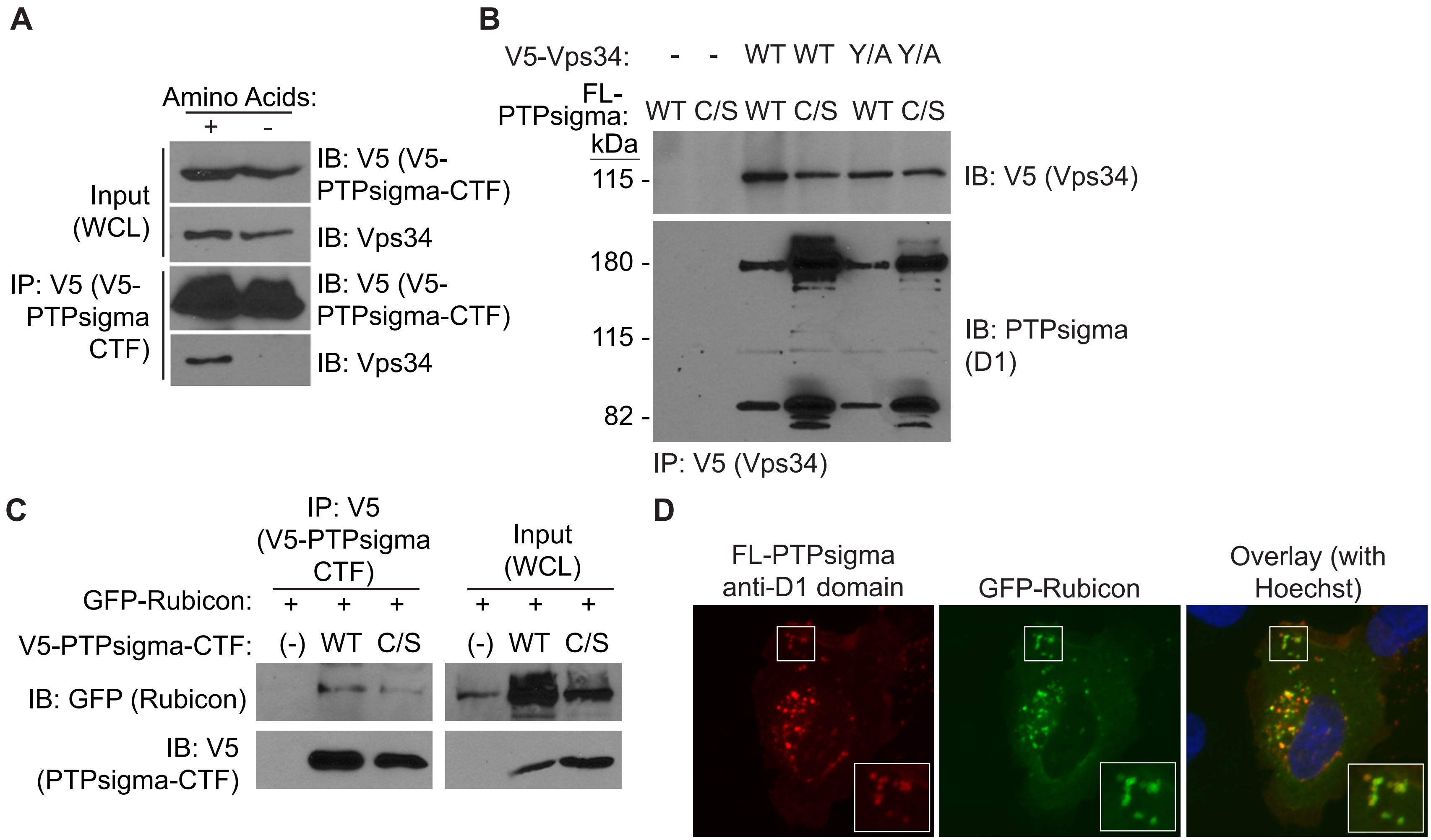

Figure 2.11. Phosphotyrosine analyses following PTPsigma knockdown. (A) Vps34-V5, Flag-Vps15, and Beclin1 were expressed in U2OS cells transfected with control or PTPsigma siRNAs. Cells were treated with (+) or without (-) pervanadate (VO_4) for 30 min prior to cell lysis. V5-immunoprecipitates were probed by immunoblot with V5 or phospho-tyrosine (pTyr) antibodies. Heavy chain (HC) shown as an IP control. (**B)** U2OS cells transfected with control or PTPsigma siRNAs were immunoprecipitated with pTyr antibodies and probed with pTyr antibodies by western blot. Heavy chain (HC) indicated as an IP control.

Figure 2.11 (cont'd)

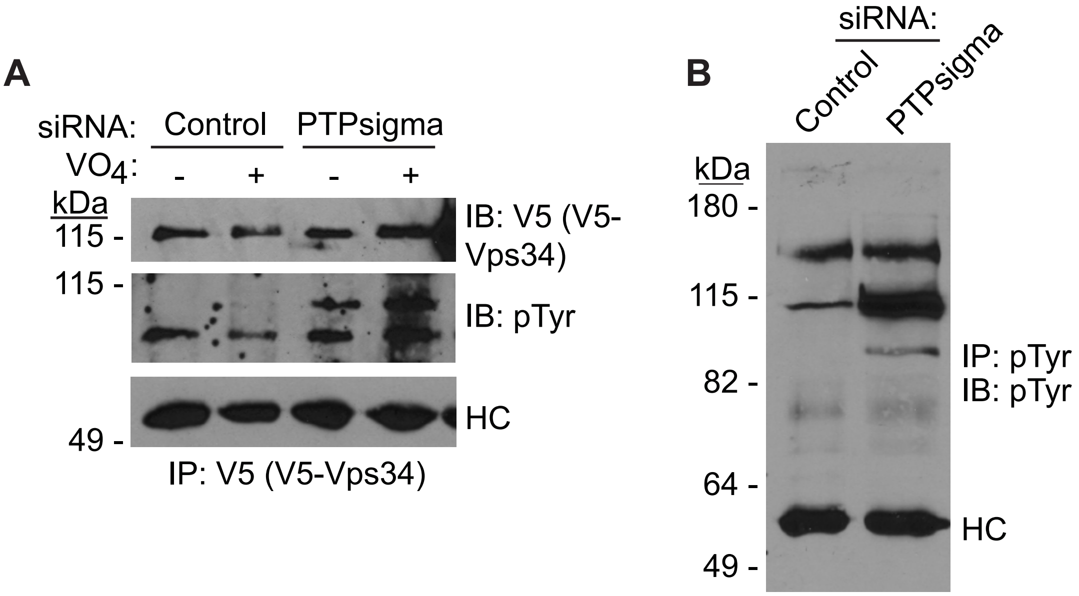

Figure 2.12. ***In vitro*** **kinase activity of functional Vps34 complexes. (A-B)** Vps34 complexes were tested for functional interactions and activity. (A) Combinations of V5-Vps34, Flag-Vps15, and Beclin1 were transfected into 293FT cells and immunoprecipitated with V5 antibodies. Whole cell lysates (input) and immunoprecipitates (IP) were probed by western blot with V5, Vps15, and Beclin1 antibodies. (B) V5-immunoprecipitates were analyzed for *in vitro* kinase activity. IPs were incubated with phosphatidylinositol (PtdIns) and ^{32}P-ATP in kinase assay buffer, lipids extracted, and ^{32}PI(3)P products visualized by autoradiography (bottom panel) or quantified by phosphorimaging (plot). **(C)** U2OS cells transfected with control or PTPRS siRNAs were further transfected with the Vps34 core complex (V5-Vps34, Flag-Vps15, and Beclin1) or the core complex plus GFP-Rubicon and GFP-UVRAG. *In vitro* kinase assays were performed as in (B) and ^{32}PI(3)P quantification shown.

Figure 2.12 (cont'd)

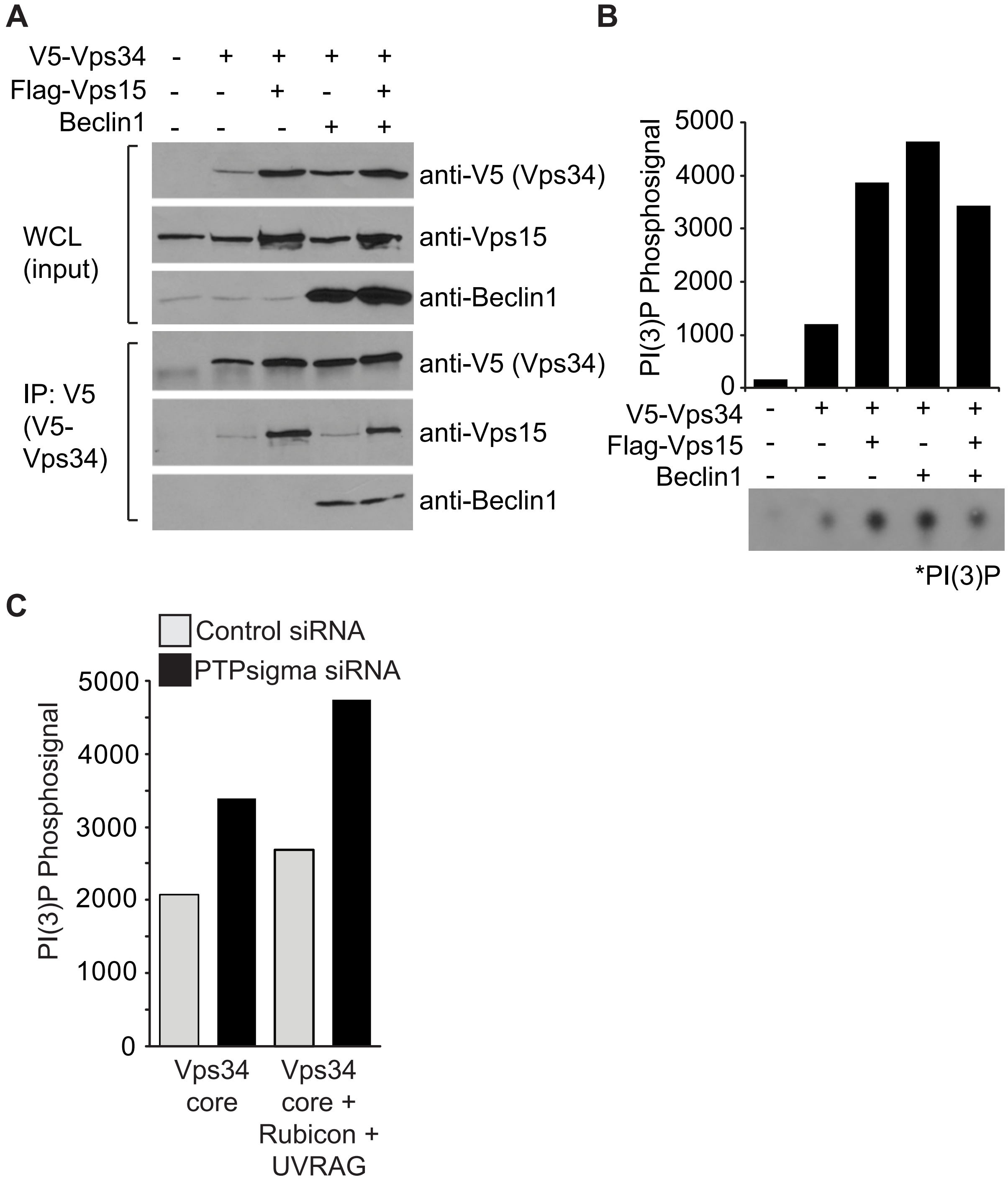

Figure 2.13. Proteolytic processing of PTPsigma. (A-B) A PTPsigma C-terminal fragment (CTF) is generated and processed in a lysosomal pathway. (A) U2OS cells expressing full-length untagged PTPsigma (FL-PTPsigma) were treated with bafilomycin A1 (BafA1), a lysosomal inhibitor, for 0 to 240 minutes. Lysates were probed by western blot with D1-targeted PTPsigma antibodies. (B) U2OS cells expressing FL-PTPsigma were pre-treated with Batimastat (Bati), an extracellular metalloprotease inhibitor, or DMSO (vehicle) for 4 hr then supplemented with BafA1 for the indicated times. Lysates were probed by western blot with D1-targeted PTPsigma antibodies. **(C)** U2OS cells expressing FL-PTPsigma were amino acid-starved to induce autophagy for the times indicated in the absence (left) or presence (right) of BafA1. Lysates were probed by western blot with D1-targeted PTPsigma antibodies.

Figure 2.13 (cont'd)

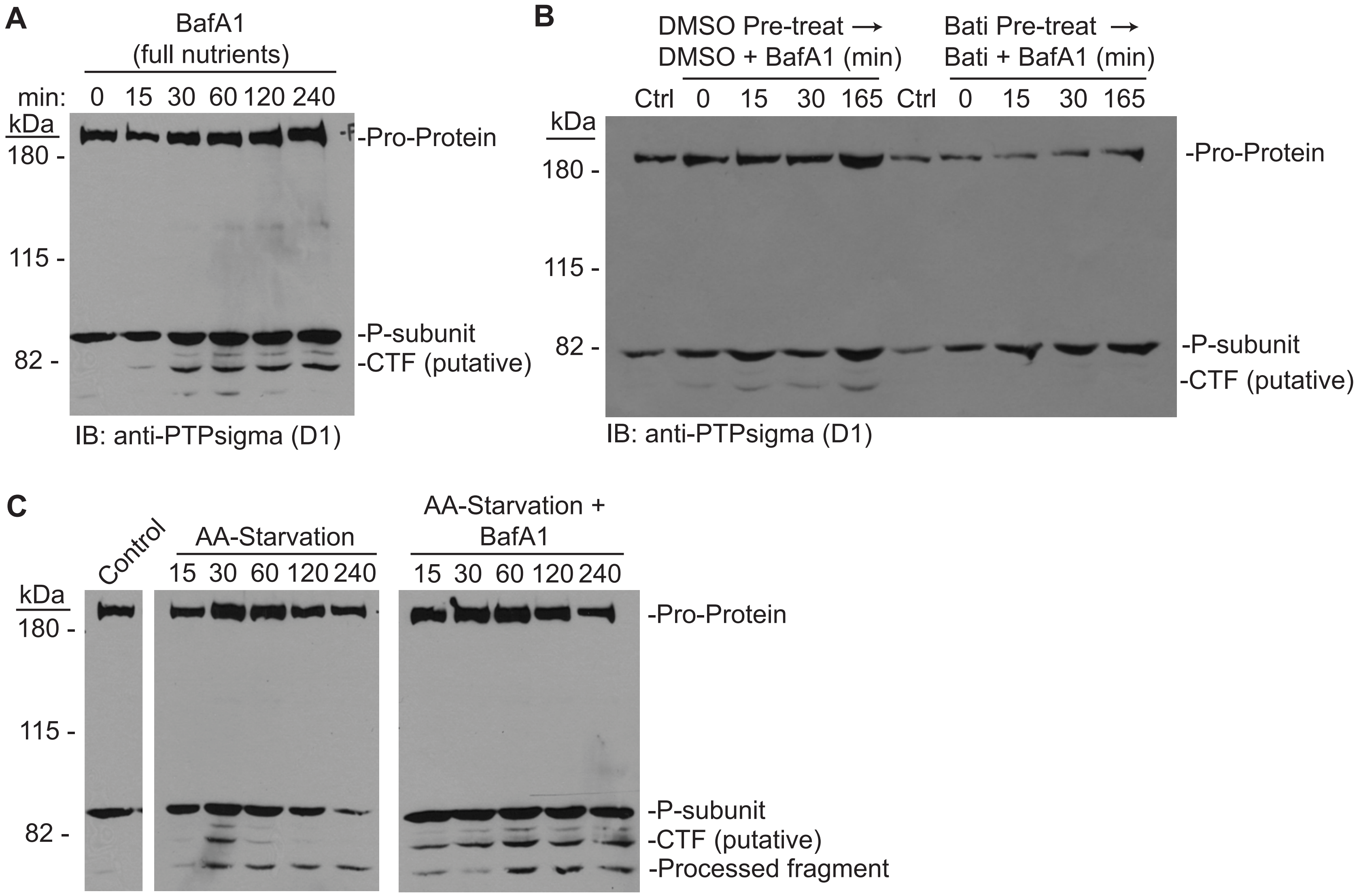

CHAPTER 3

In silico-based identification of small molecule inhibitors targeting PTPsigma

Martin KR, Xu Y, Narang P, Petit J, Meurice N, Xu E, MacKeigan JP

INTRODUCTION

Tyrosine phosphorylation is a key mechanism by which cells exert exquisite control of signaling processes. Protein tyrosine kinases (PTKs) and phosphatases (PTPs) work in concert to control these cascades and alterations in the expression or activity of these enzymes hallmark many human diseases (Tonks 2006; Lahiry, Torkamani et al. 2010). Given their generally positive regulation of signaling, protein kinases have long been the focus of both extensive research and drug development efforts. In contrast, the molecular characterization of PTPs trailed that of PTKs by ten years, and their role as critical mediators of signal transduction was initially underappreciated (Tautz, Pellecchia et al. 2006). Only recently has the PTP field reached the forefront of disease research and as justification for this, half of PTP genes are now implicated in at least one human disease (Tautz, Pellecchia et al. 2006).

The development of phosphatase-modulating compounds is critical not only for potential therapeutic benefit, but more fundamentally, for use as molecular probes which will be useful for discerning the complex functions of these enzymes. Unfortunately, phosphatases have historically been perceived as “undruggable” for several important reasons (Tautz and Mustelin 2007). The first is that a single phosphatase often controls multiple signaling pathways and thus, inhibition would not yield a specific desired result. Second, signaling cascades are generally controlled by multiple phosphatases and accordingly, blocking the activity of one may not be sufficient to yield a desired pathway effect. Finally, and most importantly, the active site of phosphatases displays high conservation which hinders the ability to develop catalysis-directed inhibitors with any degree of selectivity (Tautz and Mustelin 2007). Despite these pitfalls, the emerging role of phosphatases as mediators of vital cell processes and disease etiology has necessitated a solution to these drug development issues. Largely through use of structure-based drug design, several PTPs are now promising targets for disease treatment. Most notably, bidentate inhibitors of PTP1B, implicated in type II diabetes and obesity, have been developed which span both the catalytic pocket and a second substrate binding pocket discovered adjacent to the active site (Shen, Keng et al. 2001; Zhang 2002; Sun, Fedorov et al. 2003).

Several studies have uncovered physiologically important functions for PTPsigma, a dual-domain receptor type PTP, which highlight its attractiveness as a biological target. It has been well established, primarily through knockout animal studies, that loss of PTPsigma expression enhances axon guidance and neurite outgrowth (Elchebly, Wagner et al. 1999; Wallace, Batt et al. 1999). Further, it was recently reported that loss of PTPsigma facilitates nerve regeneration following spinal cord injury (SCI), owing to the interaction of its ectodomain with chondroitin sulfate proteoglycans (CSPGs) (Shen, Tenney et al. 2009). In addition to its neural function, PTPRS has been implicated in two cancer paradigms, chemoresistance and metastatic disease. First, RNAi-mediated knockdown of PTPsigma in cultured cancer cells was found to confer resistance to several chemotherapeutics (MacKeigan, Murphy et al. 2005). Additionally, loss of PTPRS expression in metastatic prostate cancer was uncovered through a study of laser-captured patient tissues encompassing progressive stages of prostate malignancy (Tomlins, Mehra et al. 2007). Finally, we have discovered that loss of PTPsigma hyperactivates autophagy, a cellular recycling program that may contribute to chemoresistance of cancer cells (Martin, Xu et al. 2011). Taken together, it is apparent that modulation of PTPsigma may have therapeutic potential in a range of diseases including SCI, neuronal diseases, and cancer. Aside from therapeutic potential, a better understanding of the cellular function of PTPsigma and its substrates would be aided by use of a specific molecular inhibitor.

Several approaches can be taken for the identification of small molecule inhibitors of phosphatases. The first method involves high-throughput screening (HTS) of thousands of compounds *in vitro* (Tierno, Johnston et al. 2007). This approach has become plausible with the advent of automated HTS instrumentation and has been successfully utilized to discover inhibitors of LAR (PTPRF), PTP1B, SHP2, CD45, and others (Mattila and Ivaska 2011). While this approach is beneficial in that it directly measures enzyme inhibition by a variety of scaffolds, the technical and physical investment is considerable as is the potential for experimental artifacts leading to false negatives and positives.

An alternative approach to an initial *in vitro* screen, and the one adopted for this study, involves a primary screen completed entirely *in silico*. This method entails computationally docking small molecules into the crystal structure of a phosphatase active site and selecting hits as those molecules which bind favorably, akin to a natural substrate (Kitchen, Decornez et al. 2004). Subsequently, the chosen lead scaffolds can be screened for phosphatase inhibition *in vitro*. This approach has gained popularity as the number of enzymes with solved crystal structures has increased and it is advantageous in many ways. First, utilization of the phosphatase structure allows for the exclusion of molecules which have little chance of interacting with the active site, greatly reducing the number of scaffolds to be physically screened. This manageable number of compounds contributes to improved *in vitro* screen quality and confidence in its results. Second, an understanding of the unique structural features and residues comprising the active site as well as potential proximal folds or binding pockets can guide the selection or refinement of an inhibitor. Further, an *in silico* approach is incredibly efficient in that it allows tens of thousands to millions of compounds to be virtually screened (via computer software programs) in a matter of weeks with no wet lab undertaking.

In this study, we sought to identify small molecule inhibitors targeting the active site of PTPsigma. We employed virtual library screening (VLS) in conjunction with *in vitro* phosphatase inhibition assays, to identify structural determinants of PTPsigma inhibitor activity, selectivity, and potency (Figure 3.1). From over one million compounds screened *in silico*, we identified the top-ranking 200 based on predicted optimal binding energies, which were further filtered for diversity of scaffolds and verified by visual inspection. This VLS approach identified 66 lead scaffolds with promising binding potential. These PTPsigma target leads, as well as 88 additional compounds identified by substructure search in ChemBridge, were tested for inhibition of PTPsigma *in vitro.* While we discovered several compounds with low micromolar potency against PTPsigma, follow-up investigation revealed little to no selectivity, as most scaffolds inhibited PTP1B in a similar manner. We discuss a future refinement of this approach which we predict will lead to the discovery of inhibitors with greater selectivity for PTPsigma and which could be applied to drug discovery of other classes of phosphatases as well.

RESULTS

In silico screening identifies small molecules targeted to the D1 active site of PTPsigma

The tandem phosphatase domains of PTPsigma have been crystallized in their apo form (Almo, Bonanno et al. 2007). We retrieved this structure from the protein data bank (PDB 2FH7) and verified its utility by molecularly docking a phosphotyrosine peptide. While the D1 domain exhibited favorable binding with this natural substrate, we were intrigued to observe that the active site harbored a uniquely wide conformation (Figure 3.2A). The specificity for tyrosine residues observed by classic PTPs is due in large part to a binding cleft which is deep, to accommodate a phosphotyrosyl ring, but narrow, to occlude bulkier species like phospholipids (Begley, Taylor et al. 2006). We performed a similar docking of phosphotyrosine into the active site of PTP1B and confirmed the narrowness of a typical PTP pocket (Figure 3.2B). While some of the difference in conformation may stem from the fact that the PTPsigma crystal is in an open form (that is, the WPD loop has not closed over a substrate), we hypothesized that the PTPsigma active site could be exploited in the development of inhibitors selectively targeted to PTPsigma.

To this end, we used ZINC to screen a library of ChemBridge compounds (totaling 1,100,000) *in silico* for their ability to dock into the D1 domain of PTPsigma (Irwin and Shoichet 2005). From the top scoring 200 compounds which were most favorably bound by the active site, we chose 66 compounds representing unique scaffolds to test *in vitro* (Figure 3.2C,D).

In silico-identified compounds inhibit PTPsigma activity *in vitro*

We measured the ability of compounds to inhibit the catalytic activity of PTPsigma using the generic phosphatase substrate, *para*-nitrophenyl phosphate (pNPP). The dephosphorylated product, para-nitrophenol (pNP), yields an intense yellow color under alkaline conditions measurable at 405 nm absorbance on a spectrophotometer. Briefly, compounds or controls were incubated (at a final concentration of 10 µM) with purified recombinant PTPsigma prior to the addition of pNPP substrate. The reactions were stopped, products measured, and activity calculated. We found that 19 compounds conferred inhibition of PTPsigma; the most potent being compounds 6, 46, 48, and 49 which reduced PTPsigma activity by greater than 60% (Figure 3.3A-F). We performed a library search for compounds similar to these effective scaffolds and discovered 88 additional candidates which were tested *in vitro* in a slightly modified manner. In this secondary screen, compounds were screened at a higher concentration (100 µM) but with a shortened pre-incubation period to favor direct inhibitors. We found that the majority of compounds inhibited PTPsigma by greater than 60% (Figure 3.4A-D). However, compounds similar to 46 represented less than 10% of these effective inhibitors and in fact, compound 46 itself reduced PTPsigma activity by only 30% under these modified conditions (Figure 3.4B). Accordingly, we narrowed our focus to compounds similar to compounds 6, 48, and 49 for subsequent investigation.

PTPsigma-targeted compounds lack selectivity

We next sought to establish the relative specificity of these compounds for PTPsigma over other phosphatases. To this end, we measured the ability of compounds to inhibit PTP1B, a classic PTP in a distinct subfamily. When biochemically validating competitive inhibitors, it is critical that enzymes be tested using a substrate concentration at or below the K_m (Tierno, Johnston et al. 2007). We determined apparent K_m values for both PTPsigma and PTP1B to be approximately 250 µM pNPP and then selected an optimal substrate concentration of 200 µM

(Figure 3.5B-C,E-F). Next, we selected an enzyme amount (2 µg) for each phosphatase that yielded linear product formation for the duration of the reaction while producing a maximal signal of at least five-fold above background (Figure 3.5A,D). We began by measuring inhibition with the three lead scaffolds as well as the pan PTP inhibitor, sodium orthovanadate. The compounds were each tested across a range of doses from 0 to 500 µM. Unexpectedly, we determined that not only did the lead compounds inhibit PTP1B, they did so slightly more potently than PTPsigma (Figure 3.6A-D).

Retrospectively, we hypothesized that because the primary screen conditions included a several hour pre-incubation period of enzyme and compound, the lead scaffolds may have been inhibiting PTPsigma via an indirect mechanism. In particular, because PTP active sites are maintained in a reduced state for preservation of the nucleophilic cysteine and primed for optimal activity, these enzymes are extremely sensitive to oxidation (Tonks 2005). Thus, oxidative species, such as hydrogen peroxide (H_2O_2), generated in assay buffers is a common culprit for compromised phosphatase activity (Tautz and Mustelin 2007). To determine whether the reaction conditions were favoring H_2O_2-mediated inhibition of PTPsigma, we repeated compound experiments in the presence or absence of catalase, an enzyme which converts H_2O_2 into water and oxygen. In fact, catalase negated all inhibition conferred by compounds 48 and 49 (Figure 3.6E). In all reactions, even the DMSO vehicle control, catalase increased the activity of PTPsigma (Figure 3.6E). This effect is likely explained by catalase-mediated removal of other oxidative species formed in the reaction buffer, notably from DMSO, which is a mild oxidant.

To determine if any of the original primary compounds were true competitive inhibitors of PTPsigma, we again altered the screening conditions to significantly diminish the potential for

H_2O_2 generation. We used a low dose of compound (10 µM) and reduced the pre-incubation period to only 10 minutes, as H_2O_2 inhibition is time-dependent (Tautz and Mustelin 2007). Under these conditions, we discovered that two compounds, 36 and 38, inhibited PTPsigma by approximately 40%, slightly more potent than the equivalent dose of sodium orthovanadate (Figure 3.6F). Following, we tested their strength of inhibition against PTPsigma compared to PTP1B using serially diluted doses from 0 to 100 µM. Despite inhibition of PTPsigma with IC_{50} concentrations between 5 to 10 µM, we once again observed more enzymatic inhibition of PTP1B (Figure 3.6G,H). In fact, when all 154 compounds used in this study were comprehensively tested for inhibition of PTP1B under these improved conditions, we discovered an essentially identical profile of inhibition as that of PTPsigma (data not shown).

DISCUSSION

Taken together, this virtual screening approach led to the identification of several small molecule inhibitors of PTPsigma with modest potency *in vitro*. Computational docking demonstrated that these compounds were molecularly accommodated by the D1 PTP domain of PTPsigma, similar to a natural phosphotyrosine substrate. Accordingly, we predicted that these compounds function as competitive inhibitors. Using conditions optimized for this mode of inhibition, we found at least two compounds, 36 and 38, which inhibited PTPsigma potently at IC_{50} concentrations between 5 and 10 µM. Unfortunately, we found that these compounds inhibited PTP1B with similar or slightly better efficacy than PTPsigma.

A partial explanation for this promiscuity lays in the probable generation of H_2O_2 species by at least a subset of these compounds (as was confirmed for compounds 48 and 49). Oxidation and inhibition of PTP active sites by H_2O_2 has been well established as a physiological mode of regulation (Salmeen, Andersen et al. 2003). A number of compounds, in particular those containing quinones, have been documented to inhibit phosphatases through the generation of H_2O_2 species (Urbanek, Suchard et al. 2001; Bova, Mattson et al. 2004; Tautz and Mustelin 2007). While none of the compounds we tested contained quinones, they may contain other properties and side groups which participate in oxidation (Figure 3.2C). Although the precise mechanism was not characterized, the ablation of inhibition by 48 and 49 achieved through co-treatment with catalase provides evidence that for at least these compounds, inhibition is partially mediated through H_2O_2 generation. Despite this, compounds 36 and 38 inhibited both PTPsigma and PTP1B under conditions where oxidation was not a major contributor. This suggests that despite functioning as predicted competitive inhibitors designed to dock into the distinct PTPsigma active site, these compounds do not contain selectivity for PTPsigma. They likely have sufficient abilities to bind both PTP domains studied here as well as many others.

In response to this unexpected outcome, we propose an alternative strategy for the development of small molecule inhibitors of PTPsigma with improved selectivity. First, despite our findings, we believe an *in silico* docking approach is an effective method to identify unique scaffolds that can lead to the development of both potent and selective inhibitors. However, selectivity could be improved by implementing a secondary *in silico* screen which filters out first-hit compounds that are predicted to have PTP1B binding. Scaffolds with the greatest differential in binding energies, meaning favorable docking into PTPsigma but unfavorable binding into PTP1B, would then be prioritized for *in vitro* validation. Because of this coupled primary and secondary screening and more stringent hit requirements, the primary scaffold hit list should be of greater scope than documented here and include several hundred leads from disparate classifications.

In addition, a detailed active site analysis of PTPsigma should be undertaken. Especially when sequence and structural conservation is high, as is the case for PTPs, the identification of key residues or structural determinants comprising and surrounding the active site can facilitate the identification or refinement of a selective inhibitor. For example, the undesirable druggability of PTPs stems from the fact that residues forming the active site predominantly lie within highly conserved motifs showing little sequence variability across the entire PTP family (Andersen, Mortensen et al. 2001). After performing a structural alignment of PTPsigma and PTP1B, we found that of five regions facing the active site, four were *bona fide* conserved PTP motifs (Figure 3.7A-B). The remaining region contained residues linking two hydrophobic core motifs

(Figure 3.7A). In fact, of the four residues facing the active site which differed from PTPsigma to PTP1B, we found that only two showed divergent orientations: PTPsigma residues R1498 (corresponding to S118 in PTP1B) and H1558 (corresponding to F182 in PTP1B) (Figure 3.7A). In our initial docking experiment, R1498 did not contribute to p-Tyr binding directly although it faces the active site. H1558 directly follows the WPD loop, a flexible hinge motif that folds proximal to the active site in response to substrate binding. It is possible that choosing or modifying a scaffold to incorporate molecular interaction with these residues could increase selectivity for PTPsigma. However, if the sequence conservation proves to prevent selectivity from being reasonably achieved with an active site-directed compound, targeting a less conserved region of PTPsigma, such as the ectodomain, could be pursued. Alternatively, further exploration of the crystal structure to identify adjacent binding pockets may prove productive. Use of bidentate inhibitors which bind both the active site and a proximal pocket has proven successful for inhibiting PTP1B (Zhang 2002). This dual binding mechanism is proposed to improve affinity while the interaction with less-conserved adjacent residues improves selectivity (Shen, Keng et al. 2001; Zhang 2002; Sun, Fedorov et al. 2003).

The potential utility of a PTPsigma inhibitor is evidenced by the significant finding that loss of PTPsigma increases regeneration following spinal cord injury (Shen, Tenney et al. 2009). Further, our discovery that loss of PTPsigma hyperactivates autophagy suggests that a small molecule inhibitor of this enzyme would function as an autophagy agonist. As such, it could serve as a useful molecular probe for research in this emerging field and potentially, also have therapeutic utility for a host of diseases such as neurodegenerative diseases. Unfortunately, the field of phosphatase drug discovery is plagued with issues and past setbacks, such as the difficulty in achieving selectivity. Despite this, the critical role of PTPs in normal physiology as well as disease etiology demands a solution to these problems. More rationally designed drug discovery strategies, such as those discussed here for PTPsigma, may inform the development of potent and selective PTP-targeted compounds for lead optimization.

MATERIALS AND METHODS

Structural modeling and substrate docking

The crystal structures of PTPsigma (PDB 2FH7) and PTP1B (PDB 1SUG) were retrieved from the Protein Data Bank. The initial conformations of p-Tyr peptide were extracted from the CD45-p-Tyr peptide complex structure (PDB 1YGU). The ICM program was used for protein and substrate preparation (MolSoft, La Jolla, CA). p-Tyr peptide was docked into the active site of PTPsigma and PTP1B with default parameters implemented in the ICM program. Structural docking was completed by Yong Xu.

Virtual Library Screening (VLS)

We used the ZINC library (version 8; University of California San Francisco) of ChemBridge compounds for virtual screening with the D1 active site of PTPsigma (PDB 2FH7). GOLD program was used for virtual docking and ChemScore scoring function was used to rank the top 200 hits with favorable binding energies (Cambridge Crystallographic Data Centre, Cambridge). We used ICM clustering analysis (MolSoft) to identify 66 representative compounds from unique clustering groups. Substructure similarity searching based on compounds 6, 46, 48, and 49 within ChemBridge compounds identified 88 additional leads. VLS was completed by Yong Xu.

In vitro phosphatase assays

The 66 in silico-identified compounds were purchased from ChemBridge and diluted to 5 or 10 mM in DMSO. GST-tagged recombinant PTPsigma containing all residues C-terminal to the transmembrane domain (BC104812 cDNA; aa 883-1501) was generated in pGEXKG (Guan and Dixon 1991). GST-tagged recombinant full-length PTP1B (BC018164) was generated with a 6xHIS tag in pGEXKG. Proteins were purified from BL21 Escherichia coli after isopropyl β-D-1-thiogalactopyranoside (IPTG) induction and purity was confirmed by SDS-PAGE and coomassie blue staining. Compounds were pre-incubated with recombinant enzymes in freshly prepared phosphatase buffer (50 mM sodium acetate, 25 mM Tris-HCl, 3 mM DTT, pH 6.5) for 10 to 120 minutes, as indicated in figure legends. Following, *para*-nitrophenyl phosphate (pNPP; Sigma S0942), initially diluted in assay buffer, was added to reactions for a final volume of 100 µl and reactions were carried out in a 37°C water bath for 15 to 30 minutes. Reactions were quenched with 100 µl 1N sodium hydroxide (NaOH) and 180 µl was transferred to flat-bottom clear 96-well plates. Absorbance of pNP product at 405 nm was measured on a spectrophotometer and plotted. Background absorbance values of compound-only wells were subtracted from the corresponding reactions. DMSO was included as a vehicle control.

Structural sequence alignment and analysis

SiteFinder (MOE) was used to predict the binding pocket residues of PTPsigma using the crystal structure (PDB 2FH7). PTPsigma and PTP1B sequences were aligned based on structure using MOE. Alignment was performed by Pooja Narang and Nathalie Meurice.

FIGURES

Figure 3.1 Workflow overview for PTPsigma inhibitor search. Virtual library screening (VLS) was performed using the D1 active site of PTPsigma as a target. 66 target leads were screened *in vitro* to hypothesize about structural determinants of potency using 4 chosen lead compounds. 88 additional compounds based on the 4 leads were used for structure-activity analysis. 2 non-selective but potent inhibitors resulted leading to the refinement of a model which will include consideration of selectivity constraints and a revisit of the VLS.

Figure 3.1 (cont'd)

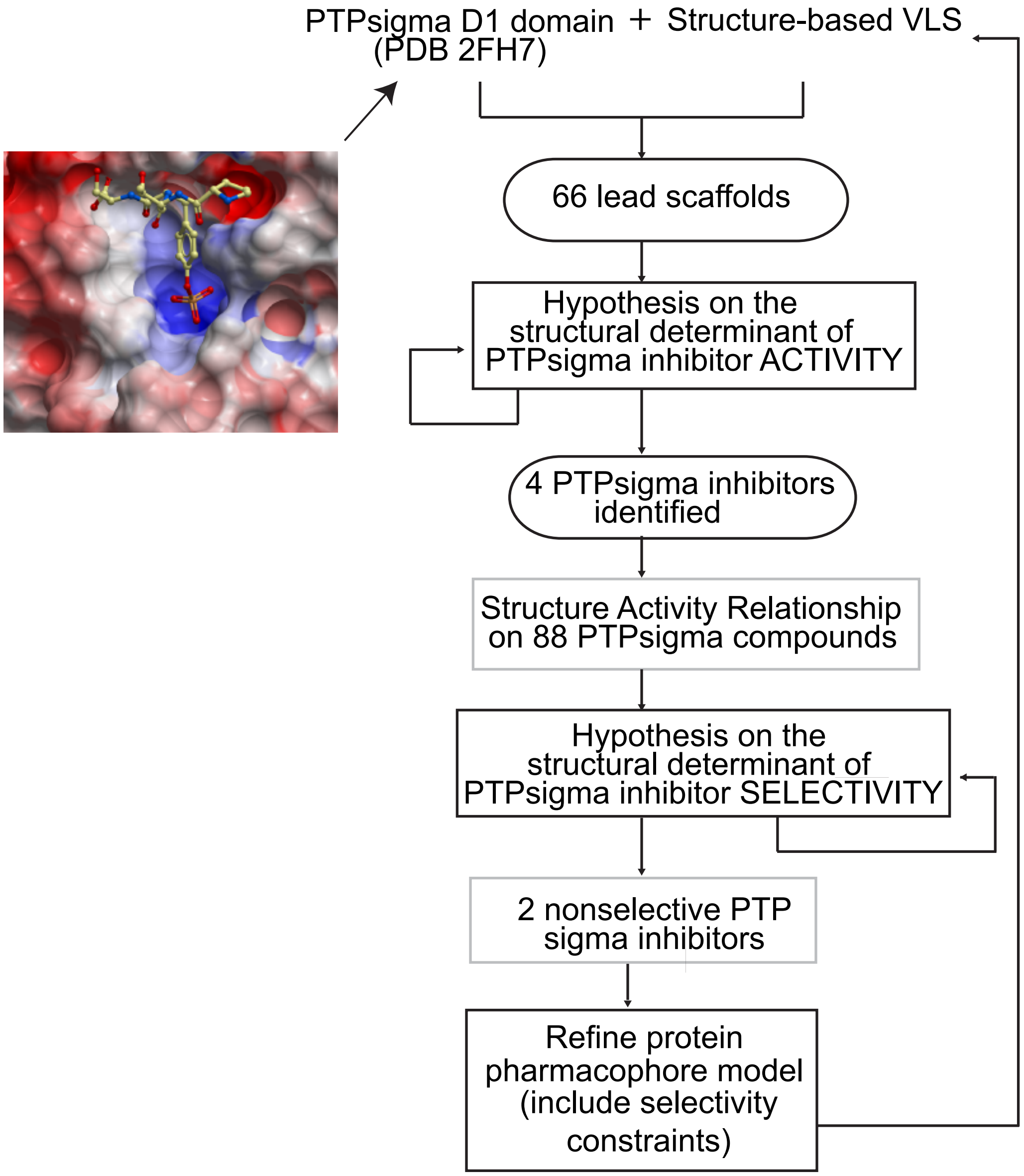

Figure 3.2. ***In silico*** **screen for compounds which dock into PTPsigma. (A-B)** Analysis of phosphatase active sites and interactions with a natural substrate. (A) The D1 domain of PTPsigma docked a phosphotyrosine (p-Tyr) substrate with favorability, although it revealed a uniquely wide conformation. (B) The PTPsigma pocket was contrasted with that of the classic PTP, PTP1B, which has a deep yet narrow active site to accommodate p-Tyr. Surface resonance of the active sites are displayed (upper panels) with negatively (red) and positively (blue) charged residues shown and substrates drawn in ball-and-stick form. Active site cross-sections are shown with bound substrates (lower panels). All structures were generated with ICM software (MolSoft). **(C)** *In silico* docking identified 66 lead scaffolds which dock into PTPsigma. A ZINC library of compounds was virtually screened for the ability to bind the D1 PTP pocket of PTPsigma. From 200 top scoring hits, 66 uniquely-structured scaffolds were chosen as leads. Chemical structures (from ChemBridge) are shown.

Figure 3.2 (cont'd)

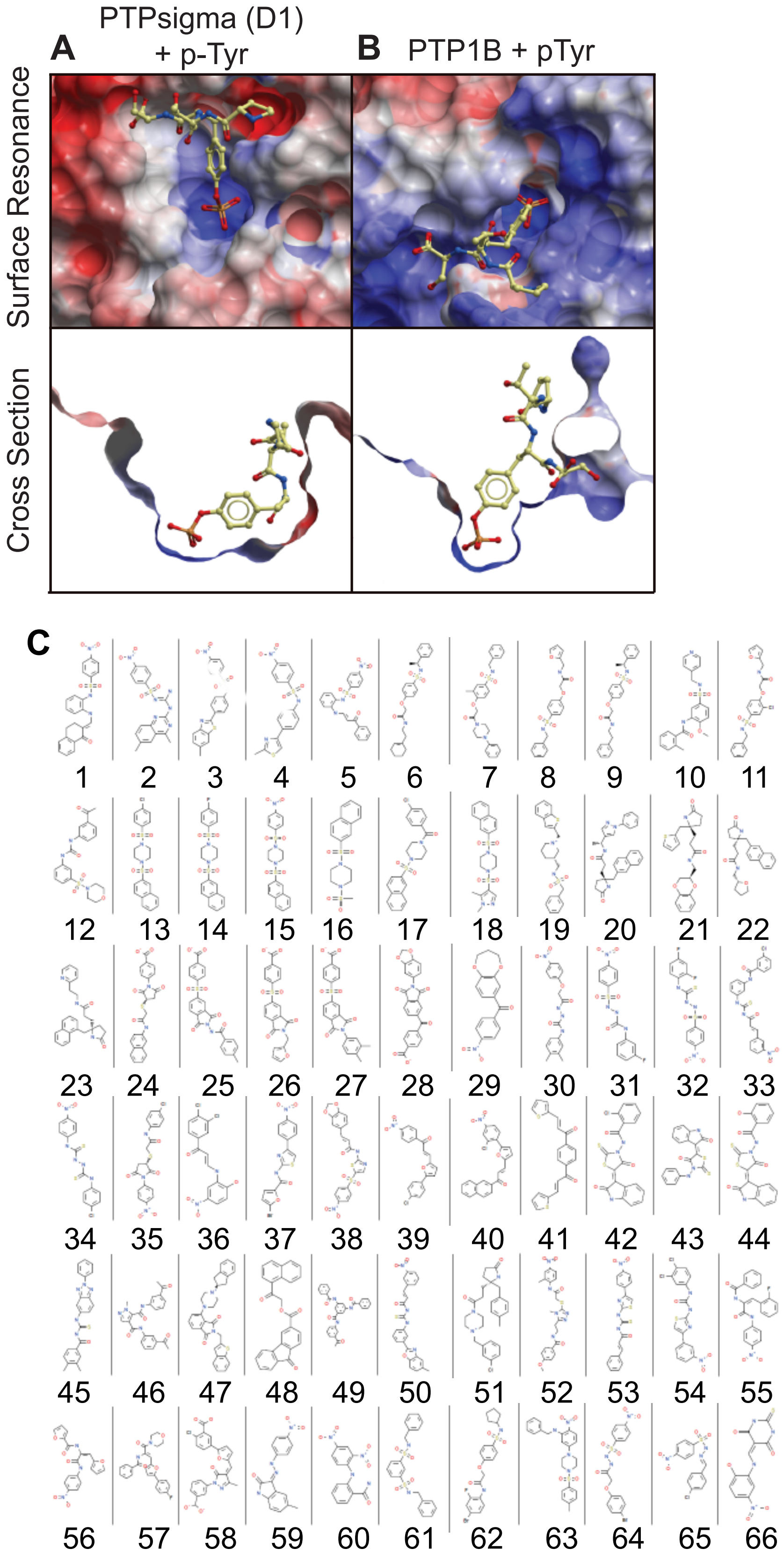

Figure 3.3. Primary *in vitro* screening of lead scaffolds filters for potency. (A) 66 lead scaffolds were purchased from ChemBridge and tested *in vitro* for the ability to inhibit PTPsigma phosphatase activity. Compounds were incubated with recombinant PTPsigma at a final concentration of 10 µM for two hours prior to the addition of pNPP substrate. Dephosphorylated product was measured by its specific absorbance at 405 nm as a readout for PTPsigma activity. Relative activity expressed as a percent (normalized to DMSO) is plotted for each compound. A threshold of 60% inhibition distinguished 4 leads from the 66 screened. Only the 19 compounds which inhibited PTPsigma in any degree are shown**. (B)** The chemical structures of the 4 lead compounds – 4, 46, 48, and 49- are highlighted. **(C-F)** The D1 active site of PTPsigma docked with each of the 4 leads is shown (C-6; D-46; E-48; F-49). Surface resonance of the active site is displayed with negatively (red) and positively (blue) charged residues shown and compounds drawn in ball-and-stick form. All docking and poses were completed with ICM software (MolSoft).

Figure 3.3 (cont'd)

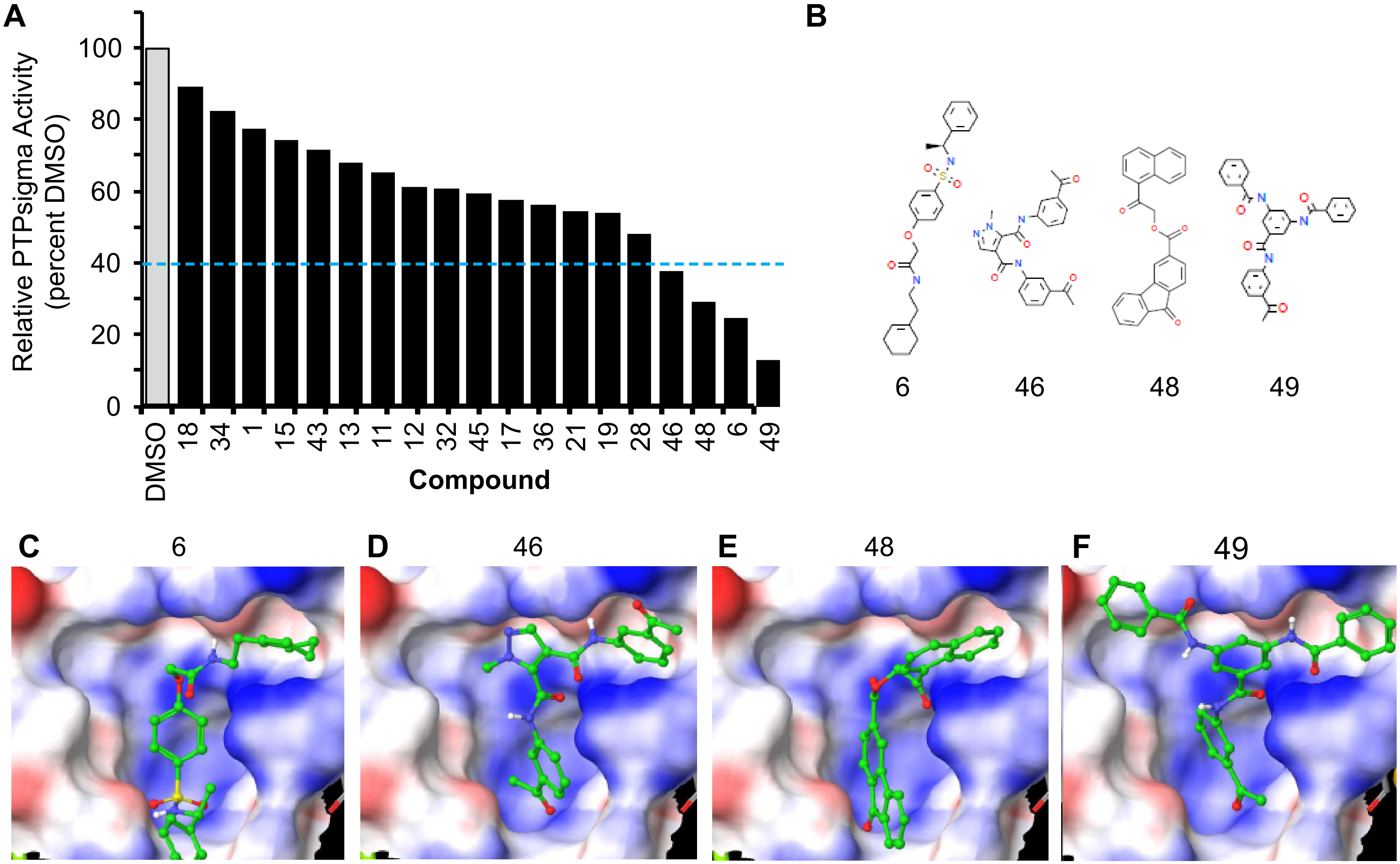

Figure 3.4. In vitro screen of additional compounds with structural similarities to the 4 leads. (A-D) 88 compounds were identified by a substructure search of ChemBridge compounds for structural features relating to the 4 leads (A- similar to 6; B- similar to 46; C- similar to 48; D- similar to 49). These were tested for potency of inhibition of PTPsigma activity as described in Figure 3.3 with the following modifications: compounds were used at a final concentration of 100 µM and pre-incubated with PTPsigma for only 30 minutes. Sodium orthovanadate (Na3VO4) is a pan inhibitor of PTPs and was included as a positive control. Original scaffolds are indicated with asterisks.

Figure 3.4 (cont'd)

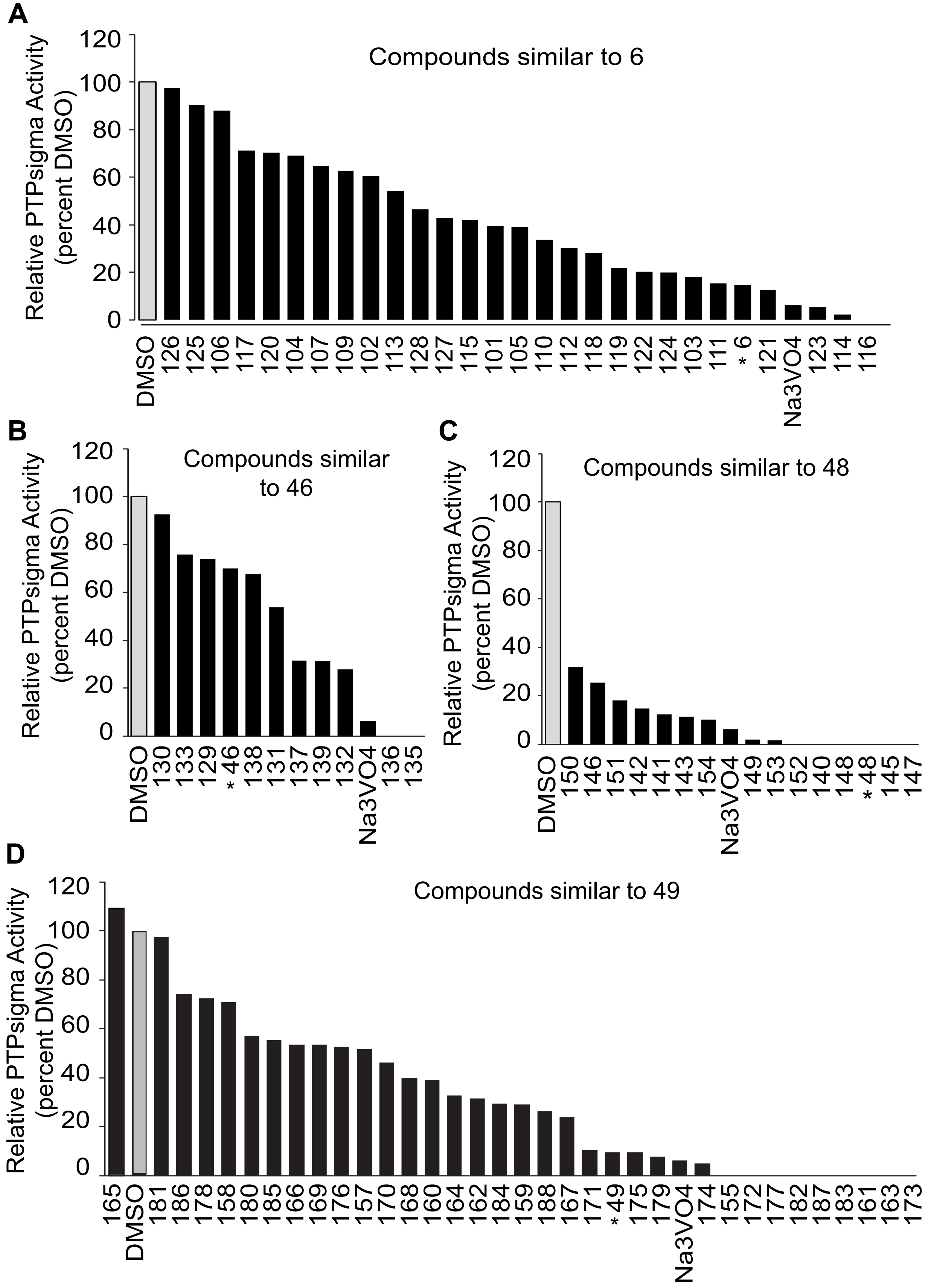

Figure 3.5. Optimization of *in vitro* screening conditions for selectivity analysis. (A-C) Analysis of the enzymatic properties of PTPsigma. (A) The linear formation of product by various quantities of recombinant GST-PTPsigma was observed through time-course reactions. pNPP-phosphatase assays were completed as described in Materials and Methods. A saturating dose of 1 mM pNPP was used and background-corrected absorbances of dephosphorylated product are plotted by time of reaction. Each plot stems from the legend-indicated quantities of PTPsigma. (B) 2 µg enzyme was chosen from (A) for analysis of activity with varying doses of pNPP substrate. Each plot represents a unique dose of pNPP (indicated in the legend). Background-corrected absorbance values of dephosphorylated product are plotted by time of reaction. (C) From the slopes of the lines of (B), initial velocities (Y-axis) were calculated for PTPsigma phosphatase activity at each of the indicated substrate concentrations (X-axis). From this, an approximate Km of 250 µM is observed. **(D-F)** The analyses outlined in (A-C) were repeated with recombinant GST-PTP1B. (**G**). 20 µg purified proteins (GST-PTPsigma-CTF or full length GST-PTP1B) were resolved by SDS-PAGE and stained with coomassie blue. Purity of products is shown with free GST in the fractions seen at ~26 kDa.

Figure 3.5 (cont'd)

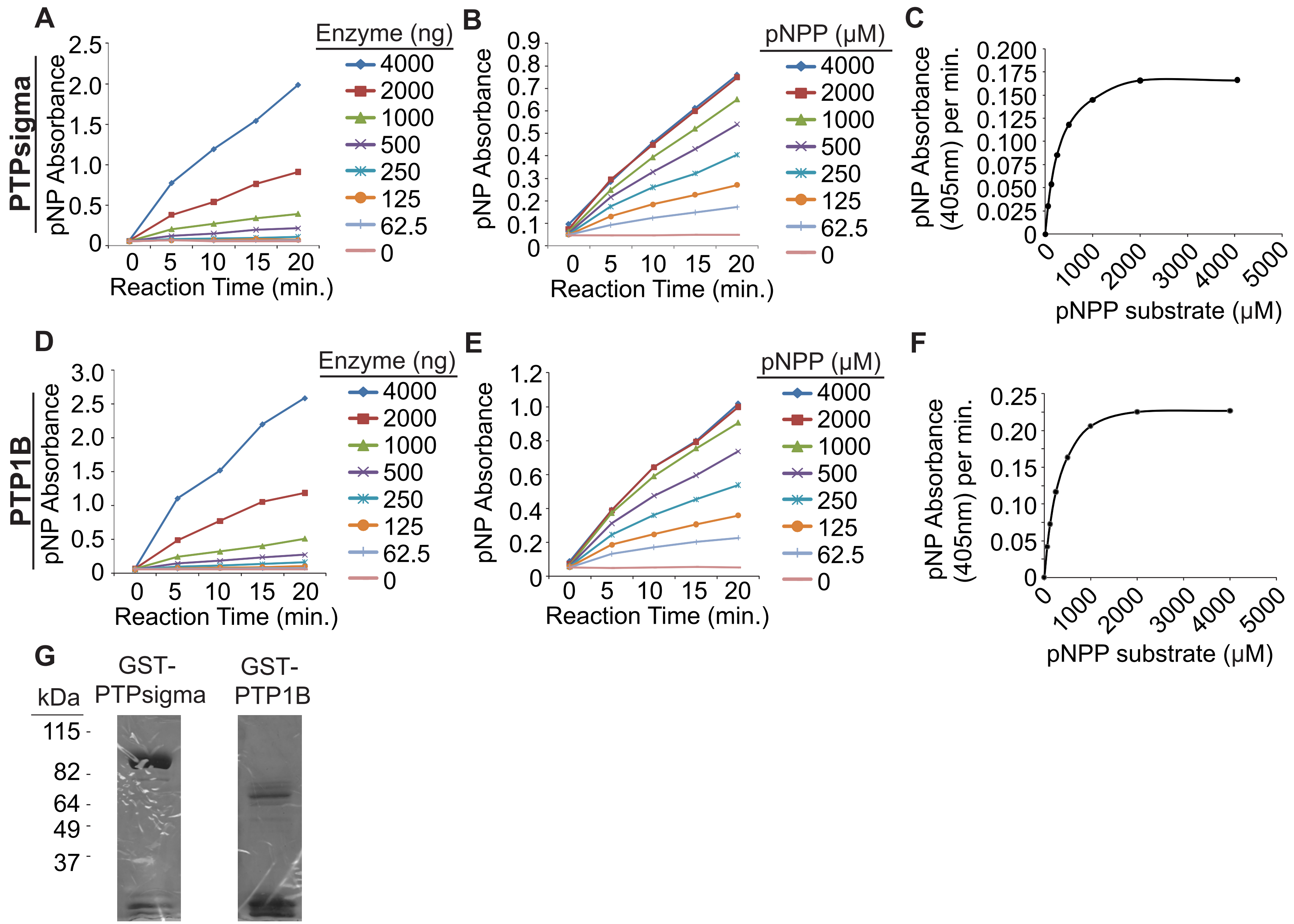

Figure 3.6. Relative inhibitions of PTPsigma and PTP1B by lead compounds. (A-D) As an initial assay, the inhibition of PTPsigma and PTP1B phosphatase activity was measured using the pan PTP inhibitor, sodium orthovanadate (A), and the three most potent original leads (B-6; C-48; D-49) by standard pNPP assay outlined in Materials and Methods. Briefly, 2 µg recombinant PTPsigma (block squares) or PTP1B (gray circles) was incubated with the doses of compound shown for 30 min at 37°C. Then, 200 µM pNPP was added for a 10 (PTPsigma) or 25 (PTP1B) min reaction at 37°C (reaction time monitored to yield sufficient signal-to-background ratio while still linear). Dephosphorylated product was measured and relative PTP activity (percent of DMSO vehicle control) is plotted. Approximate IC_{50} values can be derived from the plots and are discussed in Results. **(E)** PTPsigma activity towards pNPP was measured in the presence of DMSO vehicle, compound 48, or compound 49 as described previously. Bovine liver catalase (50 units per reaction) was included (+) to degrade hydrogen peroxide. Relative PTPsigma activity was plotted (percent of activity in DMSO without catalase). **(F)** The original 66 VLS-identified scaffolds were re-screened *in vitro* under conditions which minimized the possibility of hydrogen peroxide generation and non-specific inhibition. Here, 10 µM compound was pre-incubated for 10 min at room temperature followed by a 15 min reaction with pNPP. Compounds 36 and 38 inhibited PTPsigma by >40% (dotted line threshold), more than sodium orthovanadate at the same dose. Relative activity (percent DMSO) was plotted by all compounds tested. **(G-J)** Dose response-inhibition of PTPsigma (black square) and PTP1B (gray circles) was measured for compounds 36 and 38 using a 10 min room temperature pre-incubation period and 15 min 37°C reaction time with 200 µM pNPP. Relative activity (percent DMSO) was plotted by the indicated concentrations.

Figure 3.6 (cont'd)

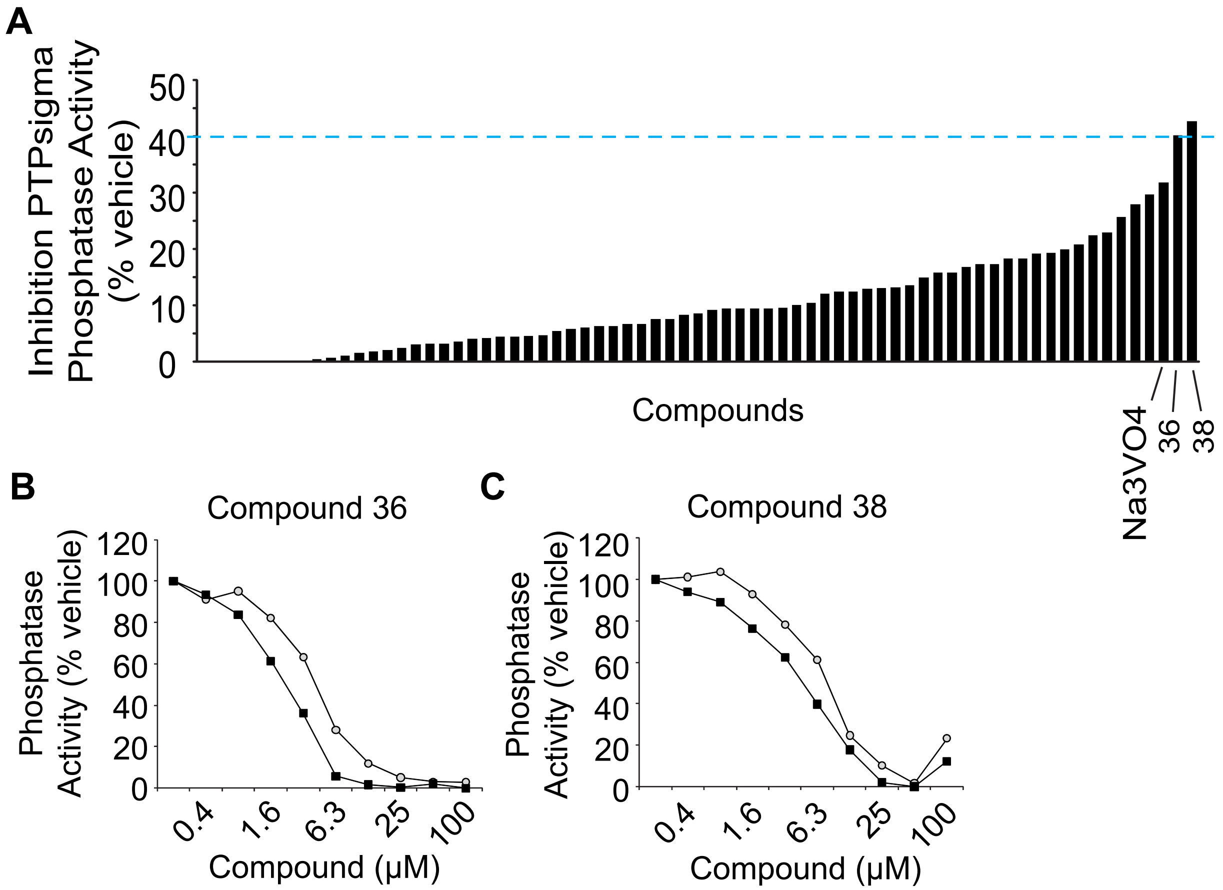

Figure 3.7. Methods for building specificity to small molecule inhibitors of PTPsigma. (A) Using the crystal structure of PTPsigma (PDB 2FH7), SiteFinder (MOE) was used to predict the D1 binding pocket. 23 residues were found and are highlighted in yellow. PTPsigma (sequence (1)) and PTP1B (1SUG; sequence (2)) were aligned based on their structures (using MOE). Residues which differ between the two are highlighted in green. The binding pocket is made up of highly conserved PTP motifs: (1) the p-Tyr recognition (KNRY) motif; (2) the least conserved region spanning two conserved hydrophobic motifs; (3) WPD loop; (4) cysteine-based catalytic site (for sequence reference, the yellow cysteine within this motif corresponds to residue 1589 in PTPsigma); (5) water/Q-loop. **(B)** The PTPsigma-D1 and PTP1B structures were aligned to highlight their structural conservation. Structures are depicted in a ribbon diagram (PTPsigma: turquoise; PTP1B: purple). A pTyr peptide docked into the active site is depicted by the red and gray spheres.

Figure 3.7 (cont'd)

A

```
1   MLSHPPIPIADMAEHTERLKANDSLKLSQEYESIDPGQQFTWEHSNLEVNKPKNRYANVI
2   ----------EMEKEFEQIDKS-GSWAAIYQDIRHEASDFPCRVAKLPKNKNRNRYRDVS

1   AYDHSRVILQPIEGIMGSDYINANYVDGYRRQNAYIATQGPLPETFGDFWRMVWEQRSAT
2   PFDHSRIKLHQED----NDYINASLIKMEEAQRSYILTQGPLPNTCGHFWEMVWEQKSRG

1   IVMMTRLEEKSRIKCDQYWPNRG--TETY--GFIQVTLLDTIELATFCVRTFSLHKNGSS
2   VVMLNRVMEKGSLKCAQYWPQKEEKEMIFEDTNLKLTLISEDIKSYYTVRQLELENLTTQ

1   EKREVRQFQFTAWPDHGVPEYPTPFLAFLRRVKTCNP--PDAGPIVVHCSAGVGRTGCFI
2   ETREILHFHYTTWPDFGVPESPASFLNFLFKVRESGSLSPEHGPVVVHCSAGIGRSGTFC

1   VIDAMLERIKPEK---TVDVYGHVTLMRSQRNYMVQTEDQYSFIHEALLEAVGCG-----
2   LADTCLLLMDKRKDPSSVDIKKVLLEMRKFRMGLIQTADQLRFSYLAVIEGAKFIMGDSS

1   -------------
2   VQDQWKELSHEDL
```

B

CHAPTER 4

Mathematical modeling of autophagic vesicle dynamics

Martin KR, Barua D, Chaudhury S, Sinitsyn N, Stites E, Posner R, Hlavacek W, MacKeigan JP
(2011). Mathematical modeling of autophagic vesicle dynamics.

Prepared for submission to *PLOS Biology*

INTRODUCTION

Macroautophagy (autophagy) is an evolutionary conserved cellular recycling program whereby cytosolic contents are sequestered in double-membrane vesicles and delivered to the lysosome for degradation (Klionsky 2007). The breakdown of autophagic cargo generates basic biochemical building blocks, such as fatty acids and amino acids, which can be exported back to the cytosol for reuse. This process is utilized by the cell to rid itself of long-lived or damaged proteins and organelles in an effort to maintain homeostasis. In addition, autophagy is dramatically upregulated during bouts of stress or starvation where it serves to generate an internal nutrient pool, an energetically favorable alternative to *de novo* synthesis.

Autophagy is executed in four stages: initiation, nucleation, maturation, and completion (Figure 4.1A). Nutrient-activated mTORC1 (mammalian target of rapamycin complex 1) controls autophagy induction by inhibiting the gatekeeper complex, ULK1-mAtg13-FIP200 (Ganley, Lam du et al. 2009; Hosokawa, Hara et al. 2009; Jung, Jun et al. 2009). When mTORC1 activity is low (i.e. during starvation), ULK1 is functional and permits the nucleation of an isolation membrane, or phagophore. The synthesis of this cup-shaped double-membrane structure is promoted in large part by Vps34, a lipid kinase which incorporates PI(3)P onto autophagic membranes, and Atg9, a transmembrane protein and putative lipid-carrier involved in membrane growth (Young, Chan et al. 2006; Webber and Tooze 2010). Expansion of the phagophore and eventual closure into a mature autophagosome is executed by two ubiquitin-like conjugation systems involving Atg5-Atg12-Atg16L and LC3 (Atg8 in yeast) (Ohsumi and Mizushima 2004). The completion of this process is marked by the fusion of the autophagosome with a lysosome (or endocytic compartment destined for the lysosome) and degradation of sequestered material (Dunn 1990; Berg, Fengsrud et al. 1998; Klionsky 2007).

Despite its initial discovery 50 years ago, essential questions about autophagy remain unanswered (Chen and Klionsky 2011). Elegant studies in yeast and mammalian systems have identified over 30 proteins required for autophagy, however, their molecular mechanisms and regulation are generally uncharacterized. Further, autophagy contributes to cell fate in a complicated manner that is incompletely understood. In a fundamental sense, it functions as a survival mechanism to delay or prevent apoptosis in response to stress, however, it can also participate in cell death when activated in excess or for prolonged periods (Codogno and Meijer 2005). Disregulated autophagy has been found to contribute to the pathology of several diseases, namely cancer and neurodegeneration (Rosenfeldt and Ryan 2009; Wong and Cuervo 2010). Therefore, greater knowledge of the regulation, molecular underpinnings, and cellular consequences of autophagy is critical not only for an understanding of normal physiology but also for the comprehension of disease etiology and the rational design of therapeutics.

An effective strategy for studying complicated cellular processes, such as autophagy, involves the construction of computational or mathematical models. These models, developed and refined from experimental knowledge, can serve as tools used to interrogate signaling pathways, formulate novel hypotheses about a system, and make predictions about cell signaling changes induced by specific interventions (i.e. genetic changes, treatment with targeted compounds) (Hopkins 2008). Here, we present the development of a novel mathematical model describing autophagic vesicle dynamics in a mammalian system. We utilized live-cell kinetic microscopy to quantify the synthesis and turnover of autophagic vesicles in response to various perturbations in single cells. The stochastically simulated model was tested by both chemical and genetic modulation of autophagic machinery and found to accurately predict vesicle dynamics observed experimentally. Further, the model predicted a positive correlation of LC3 concentration and vesicle size which has been previously reported in publications from independent groups. Taken together, we believe this model to be useful and accurate and as such, it will serve as the foundation for a more comprehensive model of autophagy in the future.

RESULTS

Construction of a conventional model of autophagic vesicle synthesis and turnover

As an initial attempt at modeling autophagy, we chose to construct a relatively simple model which described autophagic vesicle dynamics from formation to turnover (Figure 4.1B). Using knowledge of molecules integral for this process, we outlined a system which began with Vps34-catalyzed PI(3)P production. Input to autophagy triggers the activation of Vps34 (activated form depicted as Vps34*, below). The activation occurs through a step-wise function with unique rate-constants representing times prior to 0 ($t < 0$; $K_{act}\, I_1$) and times after 0 ($t \geq 0$; $K_{act}\, I_2$) (1-2). This distinction allows for a controlled pre-incubation of cells experimentally followed by exposure to specific autophagy-relevant conditions at time 0. Vps34 can also be deactivated by a first-order process (3). Active Vps34 catalyzes phosphorylation of PtdIns to form PI(3)P (PI3P, below) (4).

$$\mathrm{Vps34} \xrightarrow{I(t)} \mathrm{Vps34^*} \tag{1}$$

$$I(t) = k_{act}\, I_1 \quad t < 0;\ k_{act}\, I_2 \quad t \geq 0 \tag{2}$$

$$\mathrm{Vps34^*} \rightarrow \mathrm{Vps34} \tag{3}$$

$$\mathrm{Vps34^*} + \mathrm{PtdIns} \rightleftharpoons (\mathrm{Vps34^*} \cdot \mathrm{PtdIns}) \rightarrow \mathrm{Vps34^*} + \mathrm{PI3P} \tag{4}$$

A PI(3)P-phosphatase was included to counterbalance Vps34 activity as there have been multiple reports providing evidence for the existence of such an enzyme functioning in autophagy (5) (Vergne, Roberts et al. 2009; Taguchi-Atarashi, Hamasaki et al. 2010).

$$\mathrm{PI3P} \rightarrow \mathrm{PtdIns} \qquad (5)$$

PI(3)P functions as a second messenger which recruits lipid-binding proteins to specific subcellular compartments, in this case the isolation membrane (IM). We included WIPI (there are two isoforms in mammals, WIPI-1 and WIPI-2), a mammalian protein which reversibly binds PI(3)P during autophagy, to serve as a PI(3)P effector in our model with the complex represented by (WIPI · PI3P) (6) (Proikas-Cezanne, Waddell et al. 2004; Polson, de Lartigue et al. 2010).

$$\mathrm{WIPI} + \mathrm{PI3P} \rightleftharpoons (\mathrm{WIPI} \cdot \mathrm{PI3P}) \qquad (6)$$

The cycling of Atg9, that is its movement from peripheral locations to the isolation membrane assembly site, is important for membrane growth at this stage and it is hypothesized that Atg9 functions as a lipid-carrier (Webber and Tooze 2010). Although the mechanism is not known, it has been shown that in mammals, Atg9 cycling is dependent upon Vps34 activity, and in yeast, Atg9 function requires Atg18, a PI(3)P-binding protein (Reggiori, Tucker et al. 2004; Young, Chan et al. 2006). Further, Atg5 fails to be recruited to the IM in yeast void of Atg9 (Suzuki, Kirisako et al. 2001). Accordingly, we placed Atg9 downstream of PI(3)P formation and as a requisite for IM synthesis. Atg9 has been shown to self-oligomerize and was also detected in an asymmetric distribution on autophagic membranes (He, Baba et al. 2008; Gao, Kang et al. 2010). Therefore, we included a multistep cascade whereby PI(3)P-activated WIPI engages Atg9 (7) and only after a threshold of this multimeric complex is reached (generated in (8)), is an IM formed and Atg9 deactivated (10). Below, X_0 represents the (Atg9·WIPI·PI3P) complex and X_i represents the complex modified *n* times. Because the IM is formed *de novo*, it is depicted as (Ø → IM) and is catalyzed by the complex at the required threshold, X_n (10). The complex can dissociate when Atg9 exits the complex (10).

$$\mathrm{Atg9} + (\mathrm{WIPI} \cdot \mathrm{PI3P}) \rightarrow X_0 \tag{7}$$

$$X_0 \rightarrow X_1 \rightarrow \cdots \rightarrow X_{n-1} \rightarrow X_n \tag{8}$$

$$X_i \rightarrow \mathrm{Atg9} + (\mathrm{WIPI} \cdot \mathrm{PI3P}),\ i = 0, \ldots, n \tag{9}$$

$$Ø \xrightarrow{X_n} \mathrm{IM},\ X_n \rightarrow X_0 \tag{10}$$

Once nucleated, the Atg5-Atg12-Atg16 complex (Atg5-12-16 below) at the IM catalyzes LC3-II formation from LC3-I (representing knowledge that the complex functions like an E3-like enzyme controlling LC3-II lipidation to autophagic membranes) (11) (Fujita, Itoh et al. 2008). The IM gives way to a freely diffusing autophagic vesicle (V_{free}) once LC3-II reaches a threshold on the membrane (12,13). Blinking of vesicles between visible and invisible accounts for system noise, discussed later (14)

$$\mathrm{Atg5\text{-}12\text{-}16} + \mathrm{LC3\text{-}I} \rightleftharpoons (\mathrm{Atg5\text{-}12\text{-}16} \cdot \mathrm{LC3\text{-}I}) \rightarrow \mathrm{Atg5\text{-}12\text{-}16} + \mathrm{LC3\text{-}II} \tag{11}$$

$$\mathrm{LC3\text{-}II}_0 \rightarrow \mathrm{LC3\text{-}II}_1 \rightarrow \cdots \rightarrow \mathrm{LC3\text{-}II}_{n-1} \rightarrow \mathrm{LC3\text{-}II}_n \tag{12}$$

$$\mathrm{IM} \xrightarrow{\mathrm{LC3\text{-}II}_n} V_{free} \tag{13}$$

$$V_{free} \rightleftharpoons V^*_{free} \tag{14}$$

Turnover is marked by the conversion of vesicles from free to lysosomal-deposited (V_{lyso}) (15).

$$V_{free} \rightarrow V_{lyso}, V^*_{free} \rightarrow V_{lyso}, \qquad (15)$$

Because this dynamical model was focused simply on key players involved in vesicle dynamics, we chose to solve using conventional mechanics. Specifically, we constructed a stochastic model which was best suited to reflect the large dynamic range of vesicle measurements observed experimentally using single cells.

Experimental design for measuring autophagic vesicle dynamics

We implemented a cell system which allowed us to monitor both the synthesis and turnover of positive autophagic vesicles (AVs). We generated a monoclonal U2OS cell line stably expressing LC3 fused to a fluorescent tag (U2OS-ptfLC3), similar to the line previously used by our laboratory (Kimura, Noda et al. 2007; Martin, Xu et al. 2011). While this reporter contains both an mRFP and GFP sensor, we utilized only the GFP dynamics for the purposes of this model. Accordingly, it is referred to as U2OS-GFP-LC3 from this point forward for simplicity. Subcellular GFP-positive punctae can be captured by fluorescent microscopy and serve as an accurate marker of LC3-positive AVs. We designed an image processing protocol, including deconvolution and intensity thresholding, which allowed for the accurate quantification of AVs from single cells using fluorescent images (Figure 4.2A).

GFP-LC3 has several properties which we exploited for measurement of vesicle formation and turnover rates. First, while LC3 incorporated on the outer membranes of AVs is recycled back to the cytosol, LC3 embedded on the inner membrane is carried into the lysosome and degraded along with vesicle cargo (Tanida, Minematsu-Ikeguchi et al. 2005; Klionsky, Abeliovich et al. 2008). Therefore, LC3 turnover is an effective measure of autophagic flux (Tanida, Minematsu-Ikeguchi et al. 2005). Specifically, the rate at which LC3 accumulates in response to lysosome inhibition, measured at either the level of protein or vesicle abundance, correlates with the rate of autophagy. Further, the GFP moiety of the GFP-LC3 fusion is pH-sensitive and quenched by the acidity of the lysosome. Thus, GFP-LC3 selectively labels autophagosomes, but not autolysosomes (Kimura, Noda et al. 2007).

We used this knowledge to construct a simple system for calculating rates of autophagic vesicle production (the synthesis of a newly observed GFP-LC3 vesicle) and turnover (that is, the deposition of a GFP-LC3 vesicle in the lysosome). When lysosomal function is uninterrupted, a GFP-LC3-positive punctae represents an AV at a discrete stage of maturation between production and degradation (an IM or mature autophagosome). In the absence of stress or starvation, this number is generally low and stable, representing the steady state of autophagy. When lysosomal fusion is blocked by treatment with bafilomycin A1, a lysosomal proton pump inhibitor, the turnover of vesicles in the lysosome is prevented. Because their production continues unimpeded, vesicles then accumulate at a rate that corresponds to the level of autophagic flux (Figure 4.2B). Over a two hour time-course, we observed a substantial increase in vesicle abundance when lysosomes were inhibited, but not when they were active (Figure 4.2C,D).

With this concept in place, we sought to parameterize a simple model of autophagy. We imaged and quantified vesicle dynamics in cells cultured in full nutrient media (to determine the level of basal autophagy) and in cells treated with the autophagy-inducing mTOR inhibitor, rapamycin (to measure the level of induced autophagy). Again, we observed an increase in vesicle abundance upon lysosomal inhibition and found that this increase was exacerbated with rapamycin treatment (Figure 4.3A-D).

In order to calculate rates of vesicle synthesis and turnover from these experiments, we implemented several simple equations. First, the number of vesicles synthesized (V_{syn}) from time *t* to *t+1* was calculated using the following equation, where $V_{li(t)}$ = the vesicle count at time *t* in the presence of lysosome inhibition (bafilomycin treatment) and $V_{li(t+1)}$ = the vesicle count at time *t+1* in the presence of lysosome inhibition (16).

$$V_{syn} = V_{li(t+1)} - V_{li(t)} \qquad (16)$$

Second, the number of vesicles turned over during that same time span was calculated by coupling the formulation above with vesicle measurements obtained in cells with active lysosomes (vehicle-treated). Here, the number of vesicles turned over (V_{deg}) from time *t* to *t+1* can be calculated using the equation below where $V_{la(t)}$ is the number of vesicles at time *t* in the presence of active lysosomes (i.e. vehicle treatment) and $V_{la(t+1)}$ is the number of vesicles at time *t+1* in the presence of active lysosomes (i.e. vehicle treatment) (17). An example is illustrated in Figure 4.2B. There, by observing cells with inhibited lysosomes, we can determine that 4 vesicles were formed during the time interval captured (from 0 min to 8 min). However, in cells with active lysosomes, we saw no change in vesicle number during that time interval, indicating that 4 vesicles were normally turned over.

$$V_{deg} = V_{syn} - [V_{la(t+1)} - V_{la(t)}] \qquad (17)$$

Employing these calculations, we plotted the total number of vesicles synthesized or turned over with time basally or upon rapamycin treatment (Figure 4.3E,F). From the slopes of these lines, we determined the mean rate of vesicle synthesis during basal autophagy was 0.43 vesicles per minute while vesicles were turned over at a rate of 0.38 per minute. Rapamycin increased both vesicle synthesis and turnover to 0.68 and 0.66 vesicles per minute, respectively (Figure 4.3E,F).

Initial parameterization of the model

To begin parameterization of the model, we made estimates for starting concentrations of molecules which were consistent with levels measured in a gene expression dataset obtained from U2OS cells (Jeff Kiefer, unpublished data). Next, we used experimentally-derived vesicle counts and dynamic rates from the rapamycin and nutrient data sets collected under lysosomal inhibition to fit the model (Figure 4.4A,B). We tuned the adjustable parameters of the model so that theory curves, generated from the average of many stochastic simulations, matched the experimentally derived data (Figure 4.4A; solid and dotted lines). As one example of model tuning, we introduced positive feedback such that as the number of free vesicles (V_{free}) increases, so does the rate of turnover ($V_{free} \rightarrow V_{lyso}$). This was in response to our observation that when lysosomes are active, vesicle counts always remain relatively small, even during rapamycin-induced autophagy. This indicates that when vesicles are produced, they are efficiently turned over, a feature of the system then incorporated into the model specification.

Reassuringly, the simulated curve for the pre-incubation period (time -90 to 0 minutes) closely matched that of the experimental data, which was not used to tune the model (Figure 4.4C). To further support accuracy of the model, we uncovered experimental data curves from individual cells which closely matched theory curves generated from individual stochastic simulations (Figure 4.4D-G).

During our analysis of the experimental data, we observed fluctuations in the vesicle counts that could not be explained biologically given our experimental assumptions. For example, during bafilomycin A1-induced lysosomal inhibition, the vesicle count should never drop from one time point to the next as that would indicate vesicle degradation; however, oscillations in the data, including such drops, were observed (see curves in Figure 4.3D).We hypothesized that this noise stems from imperfections of the image analysis procedure as multiple vesicles observed juxtaposed to one another could incorrectly be counted as a single object. Additionally, it is possible for a vesicle to be hidden from view during image capture (i.e. in the perinuclear region where the cell is thicker) then reappear in a later image at a new visible cellular location. With relatively small observed vesicle counts, these occurrences could result in noticeable data fluctuations. To account for this noise, regardless of the ultimate source, we parameterized the model to include randomness generated by the ability of a freely diffusing vesicle (V_{free}) to merge with another, then split (captured in vesicle blinking; reaction (14)). Taking this noise into account, we could extrapolate true vesicle counts from visible (experimentally measured) vesicle counts (Figure 4.5A-D).

After the model was tuned, it predicted a relatively low abundance of true isolation membranes (IMs) compared to freely diffusing vesicles (V_{free}). To provide data to support this low number of IMs in our cell system, we immunostained cells using antibodies targeting Atg12, a marker of nascent IMs, and quantified on average 0.2 Atg12-punctae per cell in full nutrients, and roughly 2.0 Atg12-punctae per cell following rapamycin treatment ((Figure 4.4E; (Mizushima, Yamamoto et al. 2001)).

In sum, the tuned model produced simulated data in close alignment with experimentally-derived measurements. Thus, we next aimed to test the model by making logical predictions about the requirement for key autophagic machinery specified in the model.

The model accurately predicts output of genetic and chemical modulation of autophagic machinery

As Vps34 is required to produce PI(3)P for IM and vesicle formation, outlined in the model reactions, the model predicted that reduction of Vps34 would substantially reduce the formation and turnover of vesicles from control cells (Figure 4.5F). To test this prediction, we treated cells with wortmannin, a potent pan PI3K inhibitor which ablates Vps34 activity (Figure 4.6A). In agreement with the model prediction, we found that wortmannin treatment reduced the abundance of vesicles in the presence of active lysosomes and also reduced their accumulation upon lysosomal inhibition (Figure 4.6B,C). Employing formulas (16) and (17), we determined that wortmannin reduced vesicle synthesis and turnover rates to approximately 27% and 29% that of vehicle-treated cells, respectively (Figure 4.6D,E).

Next, we sought to formulize and test a prediction about Atg9, whose precise function and requirement in autophagy, especially in this cell type, is less clear than that of Vps34. Again, the model predicted that a 90% reduction in Atg9 content would cause a substantial reduction in vesicle synthesis and turnover, owing to its requirement outlined in the model reactions (Figure 4.7F). To test this experimentally, we transfected U2OS-GFP-LC3 cells with siRNAs targeting Atg9 for 48 hours prior to analysis and live cell imaging. Similar to Vps34 inhibition, we determined that loss of Atg9 substantially augmented vesicle synthesis and turnover rates to approximately one-third that of wild-type cells (Figure 4.7A-E).

The model predicts a positive correlation of LC3 concentration and autophagic vesicle size

Finally, we used simulations from the tuned model to form the hypothesis that levels of LC3 would positively correlate with autophagic vesicle size. When input parameters were modulated to incrementally increase LC3 concentrations, the model predicted a concurrent increase in the mean vesicle size (Figure 4.8). The small nature of autophagic structures and the resolution of objects which can be achieved by conventional fluorescent microscopy prevented us from accurately testing this prediction in our model system. However, we found reports in the literature by independent groups which supported this phenomenon. In studies in both yeast and mammalian cells, it has been observed that increased LC3 levels correlated with increased size of autophagic vesicles (Nakagawa, Amano et al. 2004; Xie, Nair et al. 2008).

DISCUSSION

In summary, we have generated a mathematical model which accurately simulates autophagic vesicle dynamics, including synthesis and turnover, under conditions of both basal and induced autophagy. Model predictions of Vps34 and Atg9 depletion were confirmed with experimental data and the model was further tuned to reflect these results.

Intriguingly, our model revealed that, at least in our cell system, once an autophagic vesicle forms, it is efficiently turned over. That is, during rapamycin-induced autophagy, we observed increased vesicle synthesis as measured kinetically during lysosomal inhibition. However, we did not see a significant rise in the number of GFP-LC3 vesicles present in cells with active lysosomes (vehicle/DMSO treatment), suggesting that those vesicles being synthesized were normally efficiently turned over. This indicates a short half-life of autophagic vesicles in this experimental system, although, because our sensor is GFP-LC3, a vesicle is no longer detected upon entry to the acidic lysosome (due to GFP fluorochrome quenching) (Kimura, Noda et al. 2007). Therefore, tracing autophagic vesicles with a more stable marker, such as endogenous LC3 or RFP-LC3, would allow insight into the entire lifespan of an autophagic vesicle from nucleation to complete degradation inside the lysosome.

We chose to model autophagy using stochastic specification given the considerable dynamic range of biological data captured from single cells. Discrete stochastic models are an ideal choice when randomness, or noise, is present in a system. In addition to detection of a wide range of raw vesicle counts and dynamic rates of synthesis and turnover across the population of cells studied, we observed fluctuations of vesicle dynamics within single cells over time. The variability observed in our system may have a number of underlying explanations from variations in cell-cycle status (our cell populations were asynchronous) to differences in genetic makeup or protein concentrations (Spencer and Sorger 2011). Regardless of the source, this dynamic variability may be a physiologically important feature of autophagy signaling within a larger network (i.e. a population of cells). In the absence of single-cell measurements, this heterogeneity would not be been observed and thus, our results contribute to accumulating evidence that resolution at the level of single cells is critical for a complete understanding of cellular processes (Spiller, Wood et al. 2010; Tay, Hughey et al. 2010; Spencer and Sorger 2011).

Experimentally captured data agreed well with model predictions of decreased vesicle production and turnover upon loss of the key autophagy proteins, Vps34 and Atg9. Further, the model led us to generate the hypothesis that LC3 concentrations correlated with increased size of autophagic vesicles. While we did not directly test this prediction, we found evidence from other published reports which supports this hypothesis. Studies from both yeast and mammalian cells have reported that increased LC3 levels correlate with increased size of autophagic vesicles, consistent with a proposed function for LC3 in phagophore elongation (Nakagawa, Amano et al. 2004; Xie, Nair et al. 2008).

The model presented here, while accurate and useful, is simple and includes only minimal molecular details. To comprehensively model autophagy, an expansion of this framework is required. Models which recognize and elucidate the vast inputs to autophagy, including contributions that feed downstream through mTORC1 and also inducers that function independent of mTOR (e.g. IP_3 depletion), will be important (Sarkar, Floto et al. 2005). Additionally, models built on a slow time scale will be useful for understanding the consequences of autophagy on cell fate. Resolution of the apparent dichotomy whereby autophagy can confer a survival advantage to cells under stress yet also contribute to cell death will be aided by an informative computational model. Finally, a model based on the one presented here, will be improved with the inclusion of all known molecular machinery involved in vesicle dynamics. The increased complexity of such a model will necessitate the use of rule-based mechanics, a modeling approach optimized for reaction networks comprising large numbers of proteins with complicated interactions, activities, and post-translational modifications (Hlavacek, Faeder et al. 2006). This rule-based model, driven experimentally through the measurement of several key nodes along the pathway, will be the focus of our future efforts.

Arguably the most important feature of a mathematical model is that it be predictive, allowing the generation of novel hypotheses which can be explored experimentally. Our model of autophagy vesicle dynamics, presented here, proved to be predictive through a series of tests, and its accuracy and utility demonstrate that it can serve as the solid foundation of a more comprehensive model of autophagy in the future.

MATERIALS AND METHODS

Experimental design and live-cell imaging

A monoclonal U2OS cell line was generated which displayed moderate expression (easily detected fluorescent punctae without saturation of signal) of ptfLC3 plasmid (Addgene plasmid 21074) (Kimura, Noda et al. 2007). Although this construct expresses both an mRFP and GFP tag fused to LC3, we only measured GFP-LC3 dynamics and thus, for simplicity, we refer to GFP-LC3 and U2OS-GFP-LC3 cells within the text.

U2OS-GFP-LC3 cells were at a density of 150,000 cells on 35 mm dishes with a number 1.5 coverglass bottom in 2 ml normal cell maintenance media (McCoy’s 5A (Invitrogen) supplemented with 10% fetal bovine serum (FBS) (CellGro)). 24 to 48 hours later, cells were switched to fresh insulin-containing media (McCoy’s 5A supplemented with 20 mM HEPES (to buffer the pH; Invitrogen) and 100 nM insulin (Invitrogen)) for 1 to 3 hours prior to treatments (henceforth called “full nutrient media”). Cells were subjected to a 90 min pre-incubation period with 2ml full nutrient media and either 125 nM bafilomycin A1 (BafA1; A.G. Scientific) or an equivalent amount of vehicle (DMSO at 1.25 µl per 2 ml; Sigma). Data from these two pre-incubation periods was captured only once with cells imaged every 4 min for 90 min (see below).

For remaining experiments, the pre-incubation period was completed in an incubator and not imaged. Following, cells were removed from the incubator, media aspirated, and replenished with the desired condition media with BafA1 (for inhibited lysosomes) or DMSO (for active lysosomes). Treatments included full nutrient media (DMSO or BafA1), 50 nM rapamycin

(Calbiochem) in full nutrient media (DMSO or BafA1), and 100 nM wortmannin (Sigma-Aldrich) in full nutrient media (DMSO or BafA1).

For live-cell imaging, GFP-LC3 was imaged in the FITC channel using a 60x oil objective and a Nikon Ti Eclipse fluorescent microscope. Cells were imaged live by maintaining a humid environment at 37°C and 5% CO_2 in an environmental chamber fixed around the microscope stage. For imaging, ten fields of view were chosen for each experiment and software set to automatically image each position every 4 min using a perfect focus function to maintain the desired focal plane. Fields of view were chosen for their inclusion of healthy cells which were adherent, at the periphery of a cluster, and moderately expressing GFP-LC3. All representative images are of the FITC channel displayed in black-and-white for easier visualization of punctae.

siRNA-mediated Atg9 knockdown

U2OS-GFP-LC3 cells were seeded at a density of 75,000 cells on 35 mm dishes with a number 1.5 coverglass bottom in 2 ml normal cell maintenance media (McCoy's 5A with 10% FBS). The next day, cells were transfected with either control (non-targeting) siRNAs or a pool of four siRNAs targeting Atg9 (Atg9A: SI04364675, SI04162781; Atg9B: SI04364535, SI04309389) at a final concentration of 25 nM using 2 µl oligofectamine (Invitrogen) in 0.2 ml Optimem (Invitrogen) and 0.8 ml normal cell maintenance media. Image capture and quantification was completed 44 to 48 hours post-transfection. Knockdown was measured by qRT-PCR using Atg9A-specific primers and an endogenous GAPDH control. Delta delta Ct method was used to determine relative copy numbers from control and Atg9 siRNA samples.

Atg12 immunofluorescence

Atg12 immunofluorescence was performed as described previously and imaged with a 60x oil objective on a Nikon Eclipse Ti microscope (see Chapter 2 Section 1).

Image processing and vesicle quantification

To quantify, images were deconvolved using a 2D blind deconvolution with three iterations and settings of normal cell thickness and normal noise level. Following, regions of interest were drawn around the borders of each cell. If nuclei or the perinuclear region had high background fluorescence, this region was omitted from the region of interest. Intensity thresholds were set to include all pixels equal to and greater than 500 units of intensity above the mean background fluorescence from the cell (to control for background fluorescence and minor variation in fluorescent expression level). Objects were quantified using an automated object count function from this thresholded region and exported to excel. For this model, vesicle count was the most utilized parameter although other parameters (size and intensity) were collected.

Mathematical modeling

The model was first described as a series of reactions (outlined in Results). Starting concentrations of all molecules was set to 10^5 molecules per cell, consistent with standard values for signal transduction proteins. Log2 transformed gene expression (microarray) data from U2OS cells (Jeff Kiefer, unpublished data) confirmed this assumption to be fair. Most kinetic parameters were assumed to be constant (typical forward constants (k_f) =1 µM s-1 and reverse constants (k_r) = 0.1 µM s-1). Other system-specific parameters (e.g. IM nucleation rates, IM lifetimes, and vesicle synthesis and degradation rates) were constrained by fitting the model to experimental data. The model was coded and implemented using programming language C. All simulation results were obtained by applying a kinetic Monte Carlo algorithm. Mathematical modeling and simulations were completed by the joint efforts of William Hlavacek, Dipak Barua, Srabanti Chaudhury, Nikolai Sinitsyn, Ed Stites, and Richard Posner (of TGen and Los Alamos National Laboratory).

FIGURES

Figure 4.1. Overview of autophagy and key molecules involved in vesicle dynamics. (A) Standard cartoon depiction of the autophagy process. Autophagy is executed in four stages: 1) mTORC1 controls autophagy initiation through inhibition of the ULK1/Atg13/FIP200 complex; 2) ULK1 activity permits nucleation of the double-membrane phagophore which is largely executed by the Vps34 complex, PI(3)P-binding effectors (i.e. WIPI proteins), and the transmembrane protein, Atg9; 3) membrane maturation into an enclosed autophagosomes is accomplished by two ubiquitin-like conjugation events involving LC3 and Atg5-Atg12-Atg16; 4) autophagy is completed when the autophagosome fuses with a lysosome (or with an endocytic compartment destined for the lysosome) to form an autolysosome which leads to the degradation of sequestered cargo. **(B)** A simplified diagram depicting the steps and molecules comprising our model of autophagic vesicle dynamics. Vps34 catalyzes the production of PI(3)P while being counterbalanced by a PI(3)P-phosphatase. PI(3)P is bound by WIPI and together, they are engaged by Atg9. This complex undergoes *n* modifications (forming a multimer) to permit nucleation of the isolation membrane (IM). The Atg5-Atg12-Atg16 complex promotes LC3-I to LC3-II conversion. LC3-II at a threshold (depicted with n) triggers IM progression into a freely diffusing autophagic vesicle (V-free). Following, V-free fuses with the lysosome to generate a lysosome-deposited vesicle (V-lyso). Proteins and organelles are encased by rounded rectangles. Other species are in non-bordered text boxes. Double-headed arrows connect non-covalent binding partners. The PI3P-WIPI-Atg9 complex is encompassed with a thick-line rectangle and X_n indicates its multimeric modification. Open circles depict catalysis. Molecular species were diagrammed using OmniGraffle Pro (The Omni Group).

Figure 4.1 (cont'd)

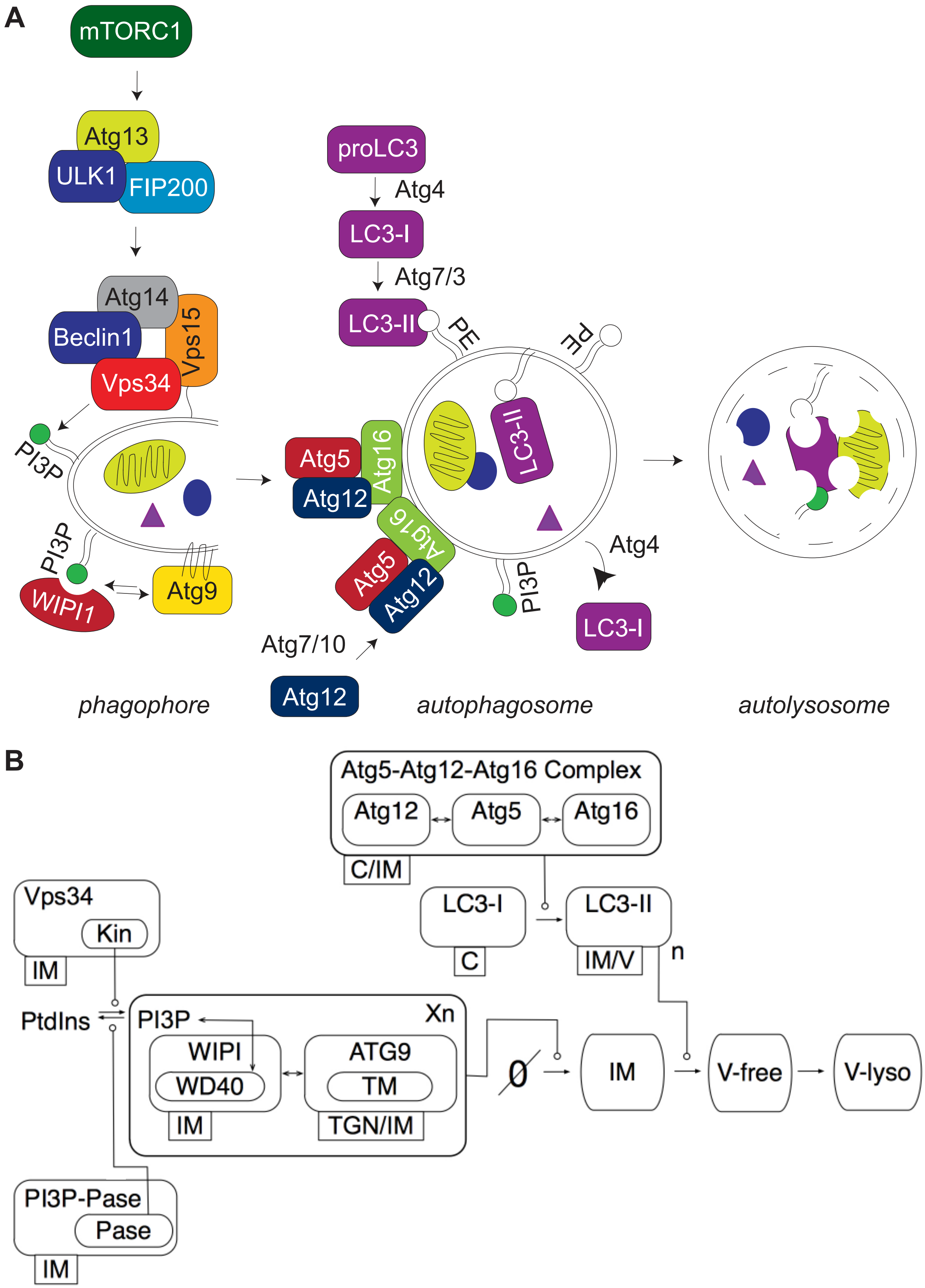

Figure 4.2. Experimental design for measuring GFP-LC3 vesicle dynamics. (A) GFP-LC3 vesicles were imaged in U2OS cells by fluorescent microscopy and subjected to an image processing protocol including deconvolution, intensity thresholding, and object quantification (see *Materials and Methods* for details). Cell shown was cropped from a 60x-captured image. **(B)** Simplified model of lysosomal inhibition. Cells treated with DMSO (vehicle control) have functional (active) lysosomes and GFP-LC3 vesicles are continually synthesized and turned over (fluorescence quenched) in the lysosome. Bafilomycin A1 treatment inhibits lysosome function to cause the accumulation of GFP-LC3 vesicles which are protected from fluorescent quenching. In this model, two vesicles form from 0’ to 4’ and two more form from 4’ to 8’. The fact that these vesicles were made but are not seen in DMSO-treated cells indicates 2 vesicles were also turned over during 0’ to 4’ and also from 4’ to 8’. **(C)** Example plots of GFP-LC3 vesicle counts from a single cell with each active (gray circles) and inhibited (black squares) lysosomes during a 120 min treatment period with full nutrient media. **(D)** Snapshots from areas imaged within single cells with active (top panels) and inhibited (bottom panels) lysosomes at 20 min intervals for 120 min treatments. Insets are from deconvolved 60x-captured images.

Figure 4.2 (cont'd)

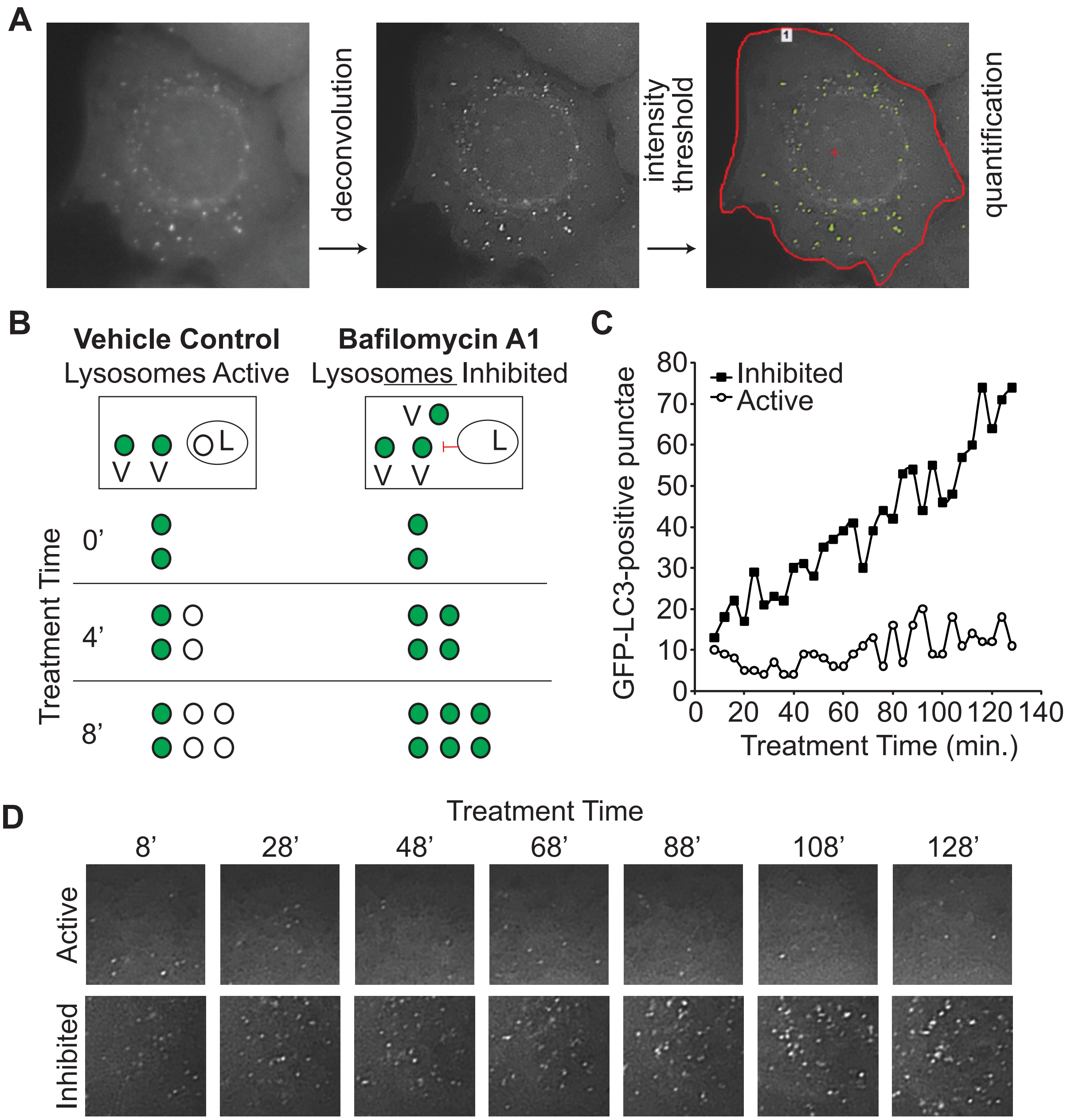

Figure 4.3. Initial GFP-LC3 data collection. (A-B) GFP-LC3 vesicle dynamics in full nutrient media (basal autophagy) and rapamycin media (induced autophagy). Following 90 min pre-incubation period with full nutrient media containing DMSO (top panels, active lysosomes) or BafA1 (bottom panels, inhibited lysosomes), U2OS-GFP-LC3 cells were treated for 120 min in fresh media of the same composition (A) or supplemented with 50 nM rapamycin (B). Cells were imaged and quantified every 4 min. An image of several cells at 0 min and 120 min is shown. Insets are 2x magnifications of boxed regions. Note the accumulation of vesicles upon lysosomal inhibition. **(C-D)** Single cell traces of GFP-LC3 vesicle counts from full nutrient media cells with active (C) or inhibited (D) lysosomes. Each line represents a single cell. **(E-F)** Total GFP-LC3 vesicles synthesized (gray circles) and turned over (black squares) in full nutrient media (E) and rapamycin media (F) from time 0 shown. Vesicle synthesis and turnover calculated using formulas (16) and (17) described in the text. Note, lines largely overlap so synthesis plot sometimes hidden by turnover plot. Bars represent standard deviation from synthesis rate calculations.

Figure 4.3 (cont'd)

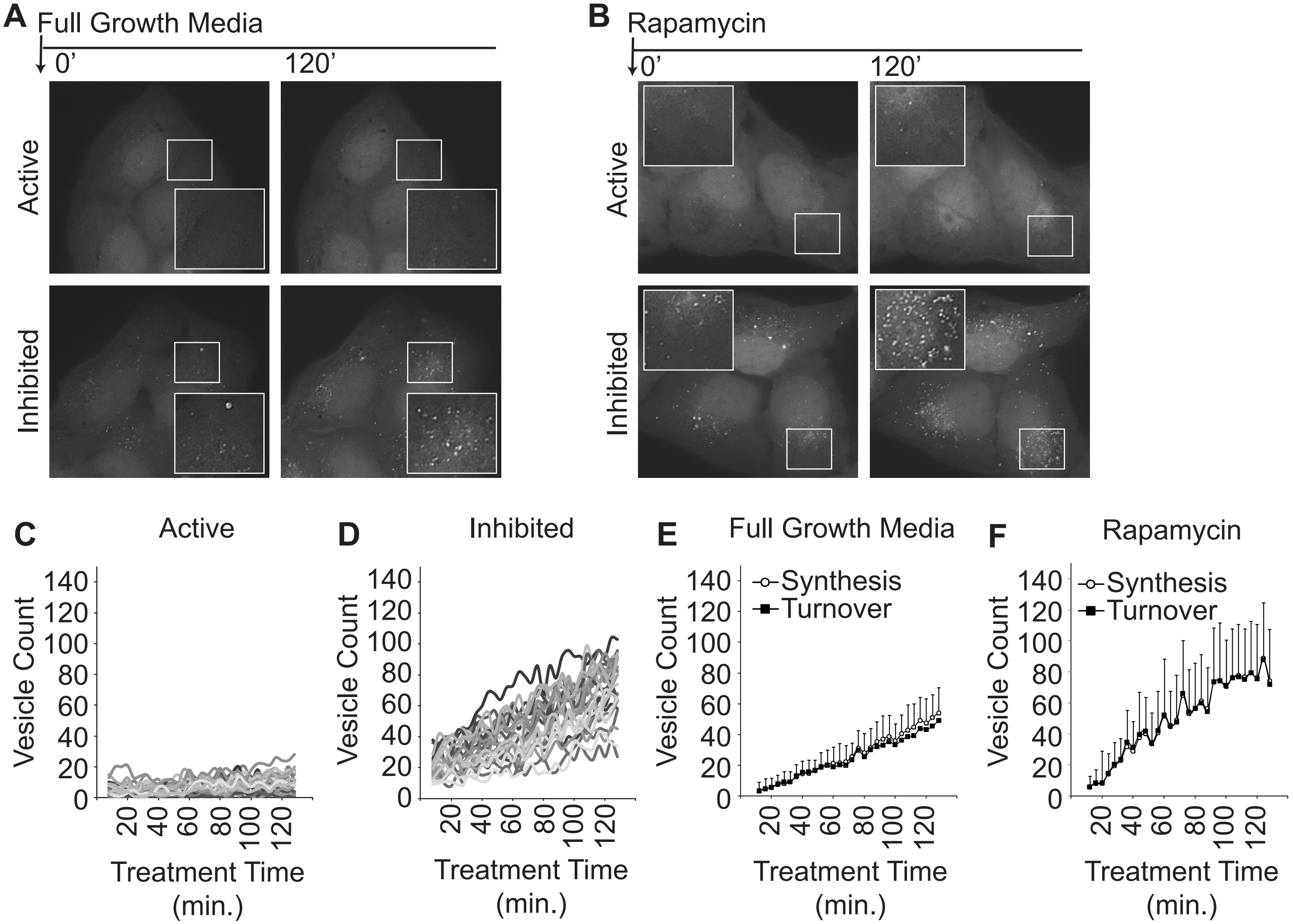

Figure 4.4. Model simulations after fitting of experimental data. (A-B) Average plots of experimental GFP-LC3 vesicle counts measured from cells during the 90 min pre-incubation period in full nutrient media with lysosomes inhibited (open squares, -90 min to 0 min) and the 120 min treatment with rapamycin media and inhibited lysosomes (black circles, 0 min to 120 min). Bars represent standard deviation. The dotted curve in (A) was generated to have the same slope as the best-fit line going through averaged data from a 120 min treatment with full nutrient media and inhibited lysosomes in (B). A theory curve (solid line) was generated for the rapamycin media condition as the average of many stochastic simulation runs. **(C)** Averaged plots of GFP-LC3 vesicle counts from cells during the 90 min pre-incubation period with full nutrient media and active lysosomes (open triangles, -90 min to 0 min) and 120 min treatment with rapamycin media (black diamonds, 0 min to 120 min). Bars represent standard deviation. A theory curve (solid line) was generated from the model tuned with parameters from (A) and (B) but not experimental value from (C). Note the agreement of experimental data with model simulation. **(D-G)** Single stochastic traces generated from the model with no parameter-tuning matched single cell GFP-LC3 vesicle traces found within the data sets. GFP-LC3 vesicle counts shown from cells under the following conditions: (D) 90 min pre-incubation period with full nutrient media and lysosomes inhibited, (E) 120 min treatment with full nutrient media and lysosomes inhibited, (F) 120 min treatment with rapamycin media and active lysosomes, (G) 120 min treatment with rapamycin media and inhibited lysosomes. These traces do not represent mean or average data but were actively selected from highly variable experimental and stochastic simulation datasets to demonstrate that single simulations match actual cell measurements.

Figure 4.4 (cont'd)

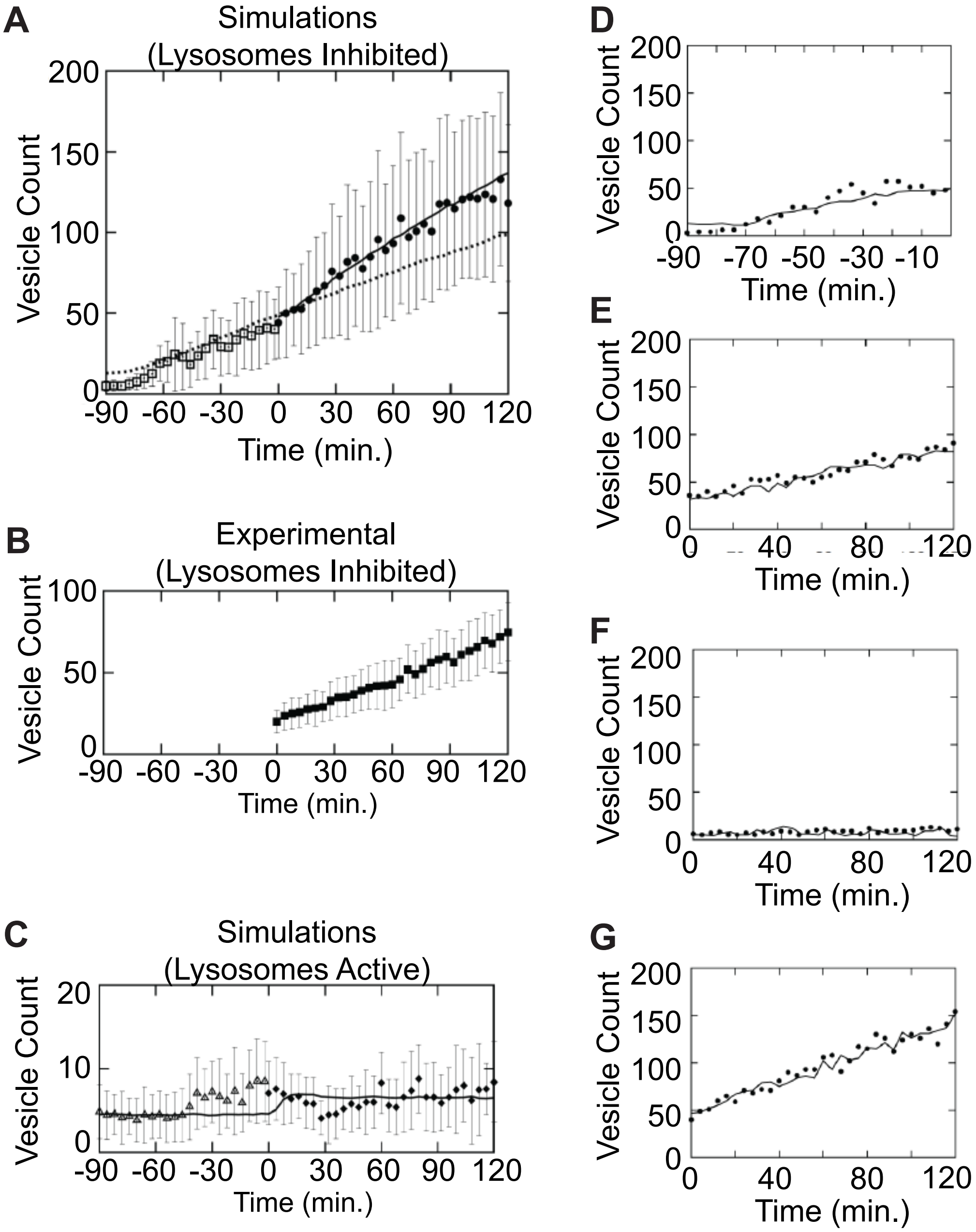

Figure 4.5. Simulations take into account observed system noise. (A-D) Theory curves generated from the tuned model are depicted for 120 min treatment periods with full nutrient media (A-B) or rapamycin media (C-D) and inhibited (A, C) or active (B, D) lysosomes. Fluctuations were observed in the experimental data and this noise was accounted for by fitting model parameters to account for visible and invisible vesicle states (see reaction (12) in text). This accounts for vesicle aggregates being miscounted as a single vesicle or vesicles disappearing from the focal plane. Resulting total vesicle counts are in red while visible vesicle counts are in black. Blue lines depict isolation membranes (IMs). Parameters were tuned to assume few IMs compared to large free vesicle numbers. **(E)** Wild-type U2OS cells were immunostained for endogenous Atg12, a marker of IMs which dissociates from the free vesicle, and supported the assumption of few IMs compared to free vesicles. AF488-conjugated secondary antibodies were to detect primary Atg12 staining and images captured at 60x. Inset represents a 2x magnification of the boxed region.

Figure 4.5 (cont'd)

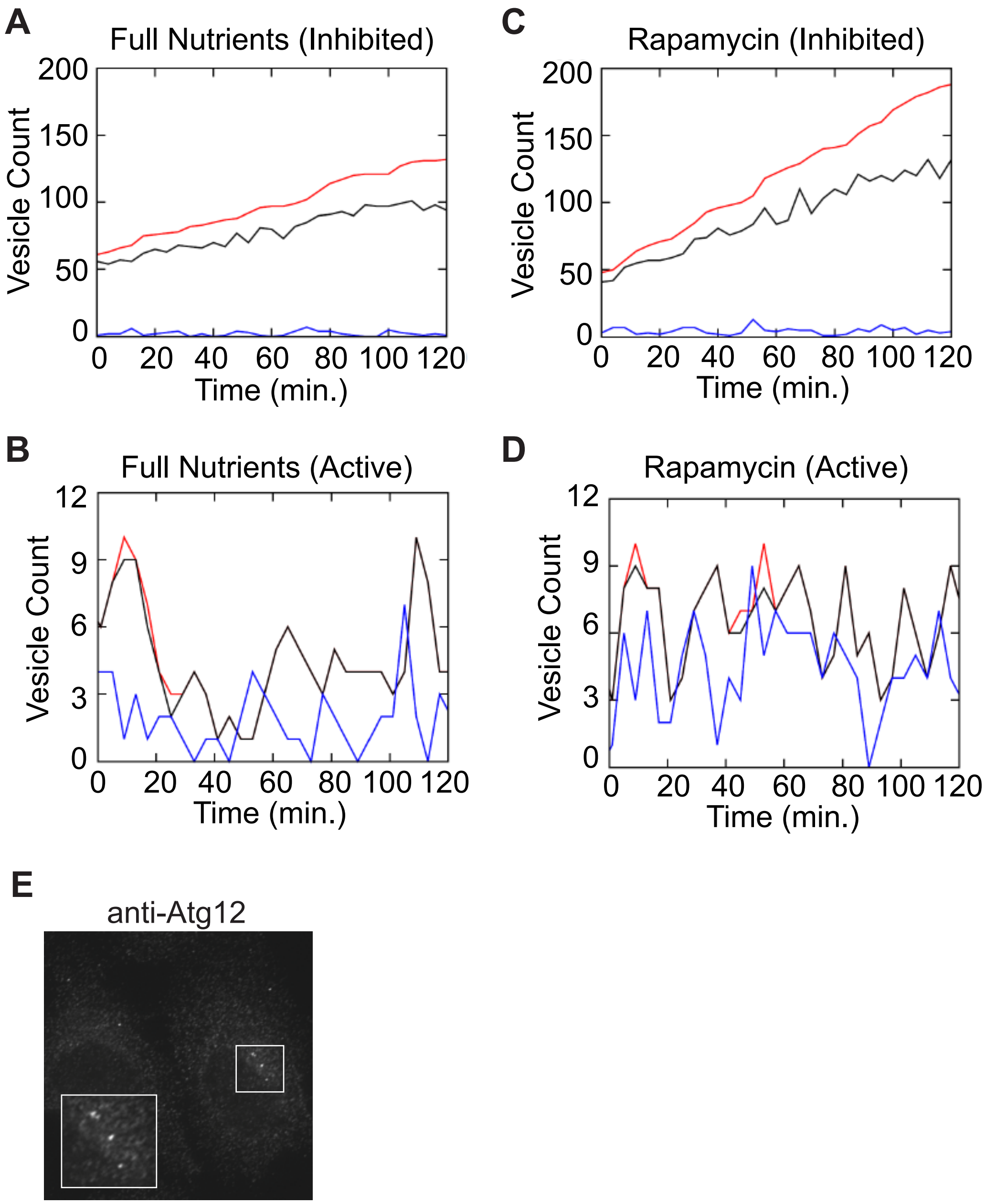

Figure 4.6. Model prediction and test: Vps34 inhibition. (A) The PI3K inhibitor, wortmannin, inhibits Vps34 activity. U2OS cells stably expressing an EGFP-2xFYVE construct which specifically binds PI(3)P show an absence of PI(3)P-positive vesicles following 30 min treatment with 100 nM wortmannin (bottom) compared to vehicle-treated cells (top). **(B-C)** Following 90 min pre-incubation period with full nutrient media containing DMSO (top panels, active lysosomes) or BafA1 (bottom panels, inhibited lysosomes), U2OS-GFP-LC3 cells were treated for 120 min in fresh media of the same composition but supplemented with 100 nM wortmannin. Images captured and quantified every 4 min. An image of several cells at 0 min and 120 min is shown in (B). Insets are 2x magnifications of boxed regions. Note the lack of accumulation of vesicles upon lysosomal inhibition. Mean vesicle counts from cells with inhibited (gray circles) or active (black squares) lysosomes are plotted in (C). Bars represent s.d.m. **(D-E)** Wortmannin reduces GFP-LC3 vesicle synthesis and turnover rates as calculated from experimental data using formulas (16) and (17) (see text). Total vesicles synthesized (gray circles) and turned over (black squares) beginning at time 0 shown. (D) Average rates of synthesis and turnover (in mean GFP-LC3 vesicles per min) during the 120 min treatments were derived from linear lines-of-best fit of the plots for wortmannin in (C) and full nutrient media in Figure 4.3E. Black bars = synthesis, gray bars = turnover. **(F)** Model-predicted simulation of 90% Vps34 inhibition when lysosomes are inhibited (solid line) or active (dotted line).

Figure 4.6 (cont'd)

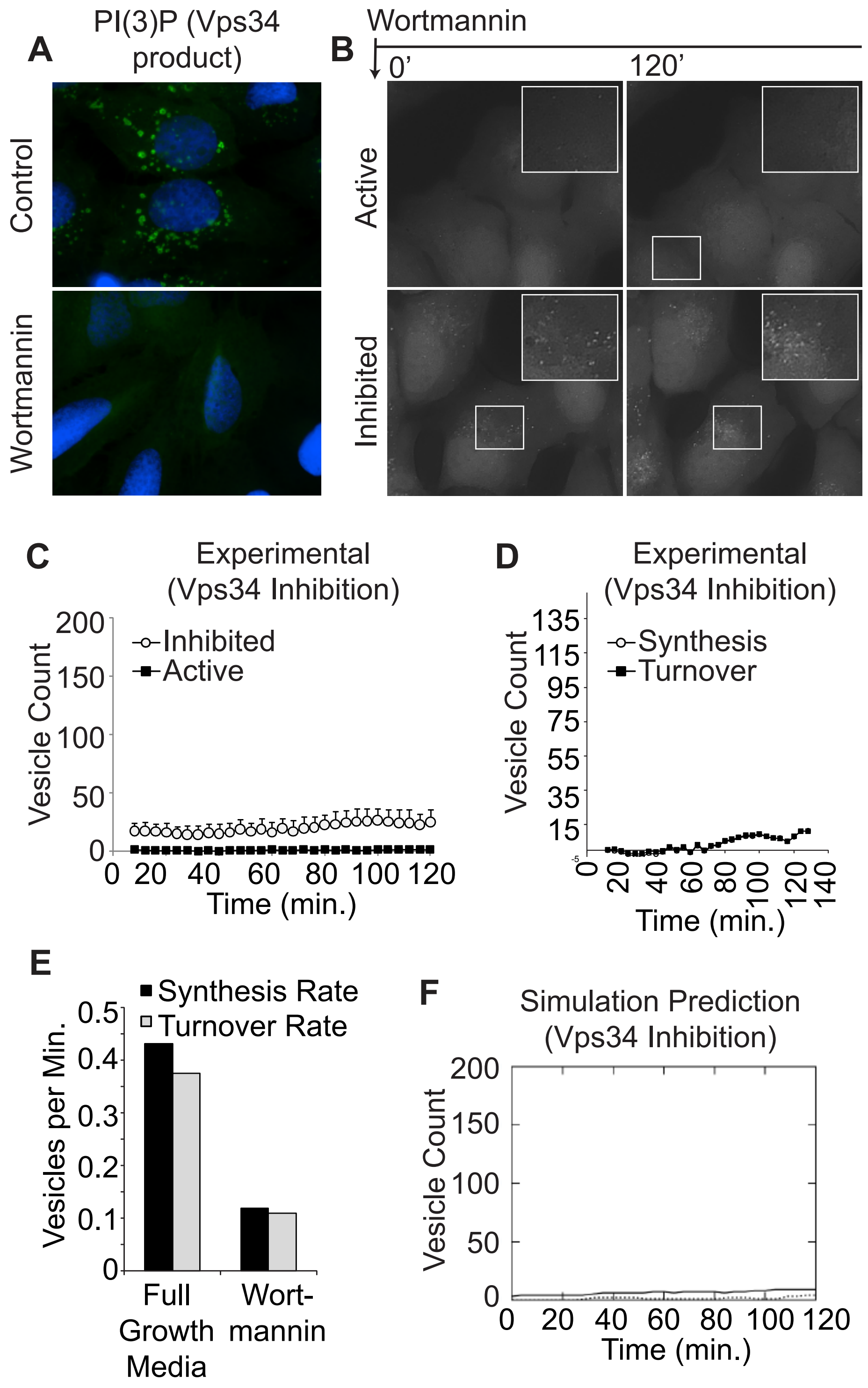

Figure 4.7. Model prediction and test: Atg9 depletion. (A-B) 48 hours prior to imaging and quantification, U2OS-GFP-LC3 cells were transfected with siRNAs targeting Atg9. Following 90 min pre-incubation period with full nutrient media containing DMSO (top panels, active lysosomes) or BafA1 (bottom panels, inhibited lysosomes), cells were treated for 120 min in fresh media of the same composition. Images captured and quantified every 4 min. Images of several cells at 0 min and 120 min are shown in (A). Insets are 2x magnifications of boxed regions. Note the lack of accumulation of vesicles upon lysosomal inhibition (and lack of efficacy of the pre-incubation because Atg9 is knocked down for the entire experiment). 120 min panels from Figure 4.3A are shown as a reference for wild-type cells dynamics. Mean vesicle counts from cells with inhibited (gray circles) or active (black squares) lysosomes are plotted in (B). Bars represent s.d.m. **(C-E)** Atg9 siRNA-mediated knockdown reduces GFP-LC3 vesicle synthesis and turnover rates as calculated from experimental data using formulas (14) and (15) (see text). (B) Total vesicles synthesized (gray circles) and turned over (black squares) beginning at time 0 shown. (C) Average rates of synthesis and turnover (expressed as mean GFP-LC3 vesicles per min) during the 120 min treatments were derived from linear lines-of-best fit of the plots for Atg9 knockdown in (B) and full nutrient media in Figure 4.3E. Black bars = synthesis, gray bars = turnover. (D) Quantitative real-time PCR (qRT-PCR) using Atg9A-specific primers demonstrated 89% knockdown of mRNA with Atg9 siRNAs versus control (non-targeting) siRNAs. **(F)** Model-predicted simulation of 90% Atg9 depletion when lysosomes are inhibited (solid line) or active (dotted line).

Figure 4.7 (cont'd)

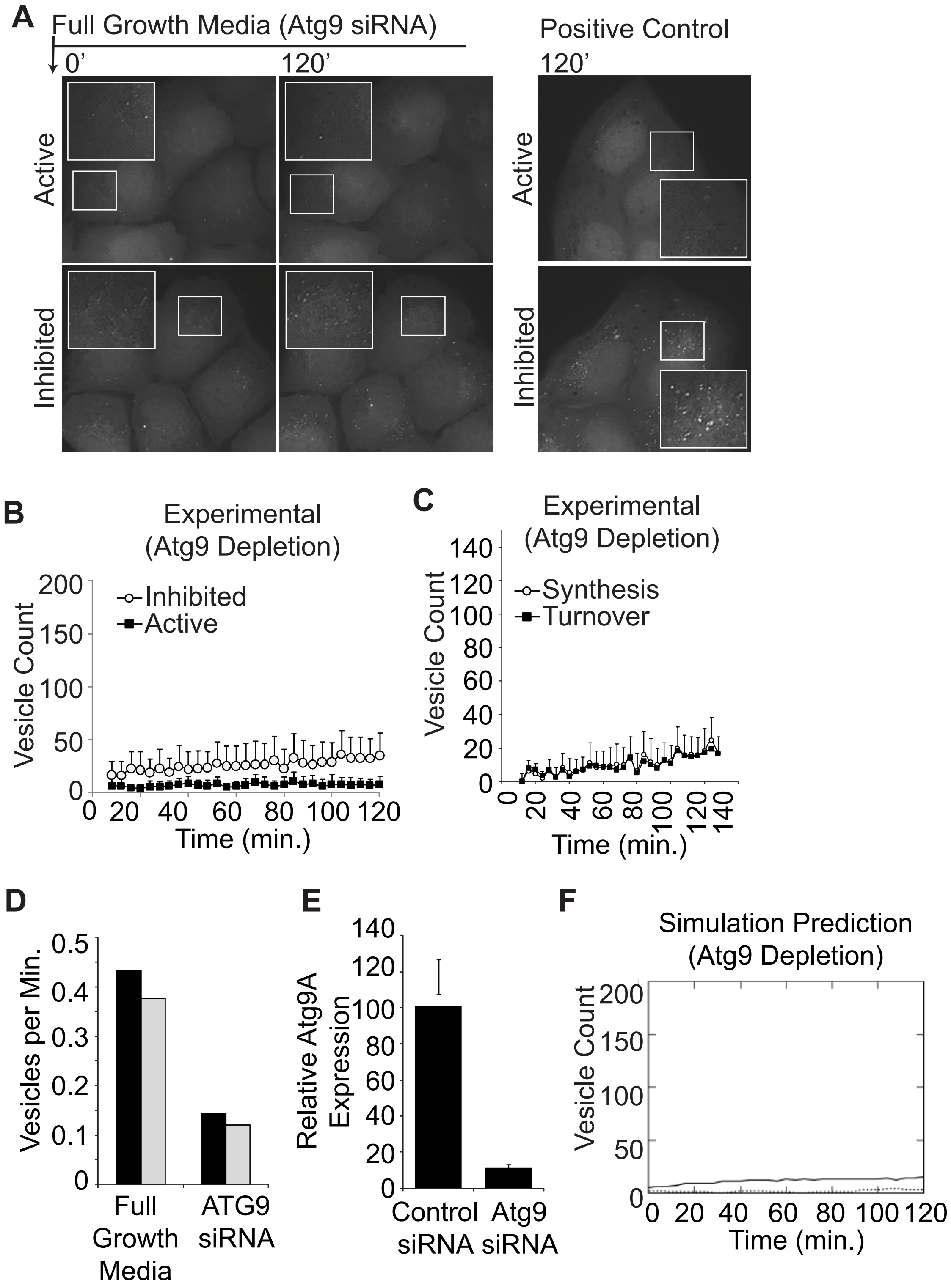

Figure 4.8. Model prediction: LC3 concentration and vesicle size. The model was used to generate predictions for several hypothetical LC3 concentrations and resulting outputs of autophagic vesicle size (in average units). Simulated conditions are 120 min of full nutrient media with active lysosomes. Each data point represents vesicle size with respect to time of treatment. LC3 concentrations correspond to 10^4/cell (red diamonds), 10^5/cell (default value used in the model) (black circles), 10^6/cell (blue triangles), and 10^7/cell (magenta squares).

Figure 4.8 (cont'd)

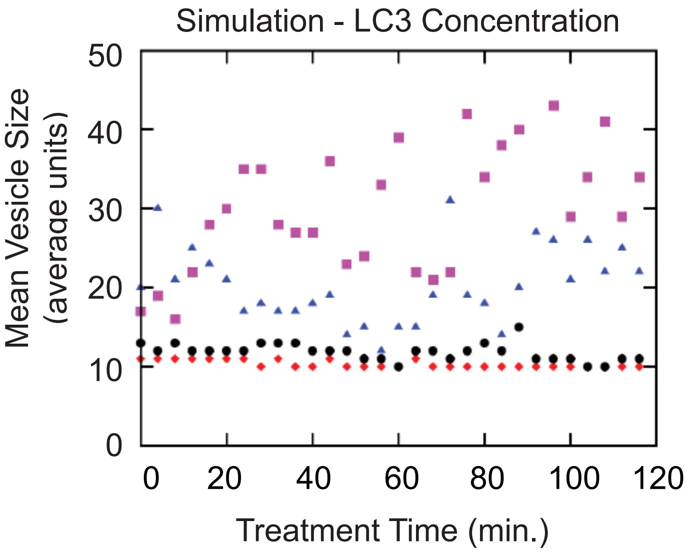

CHAPTER 5

Summary and Future Directions

SUMMARY AND FUTURE DIRECTIONS

PTPsigma as a new effector of Vps34-PI(3)P signaling

The foundation for this entire body of work was an interest in Vps34-PI(3)P signaling and the aim of identifying novel phosphatases which control PI(3)P signaling. At the time this project originated, Vps34 had been extensively characterized for its role in endocytosis, beginning with its identification in yeast and followed with a detailed mammalian characterization (Herman and Emr 1990; Schu, Takegawa et al. 1993; Stack, Herman et al. 1993; Simonsen, Lippe et al. 1998; Christoforidis, Miaczynska et al. 1999; Futter, Collinson et al. 2001).

More recently, publications had suggested that Vps34-PI(3)P signaling was also important for two additional cell processes, mTOR signaling and autophagy (Petiot, Ogier-Denis et al. 2000; Kihara, Noda et al. 2001; Byfield, Murray et al. 2005; Nobukuni, Joaquin et al. 2005). While the role in mTOR signaling has not been well substantiated in the time since, it has becoming increasingly evident that Vps34-PI(3)P signaling is essential for autophagy (Itakura, Kishi et al. 2008; Juhasz, Hill et al. 2008; Obara, Noda et al. 2008);(Proikas-Cezanne, Waddell et al. 2004). Given the pivotal role of autophagy in cell survival and its implications in the etiology of several diseases, it was the role of PI(3)P in this process that was, and continues to be, our primary interest.

We hypothesize that phosphatases exist which regulate Vps34-PI(3)P signaling during autophagy. In support of this notion, two myotubularin phosphatases have been functionalized as direct PI(3)P phosphatases with important roles in autophagy regulation (Vergne, Roberts et al. 2009; Taguchi-Atarashi, Hamasaki et al. 2010). Given the complexity of autophagy execution and the number of proteins involved in the Vps34 complexes alone, we believed it likely that additional protein phosphatases exist to control Vps34-PI(3)P signaling. Accordingly, we designed and implemented a cell-based RNA interference screen where we monitored PI(3)P dynamics following loss of expression of individual phosphatase genes. We uncovered a number of interesting phenotypes and ultimately chose to focus primarily on one, that of PTPsigma, as the PI(3)P phenotype elicited by knockdown closely matched that observed in autophagic cells.

This PTPsigma loss-of-function phenotype was intriguing because there was no clear precedence for PTPsigma in PI(3)P signaling. As a receptor-like molecule highly expressed in neurons, PTPsigma has been characterized for its role in mammalian development and the control of neurite outgrowth and regeneration. These functions likely stem from interactions of its ectodomains with other cells and the extracellular environment (Shen, Tenney et al. 2009; Fry, Chagnon et al. 2010). In agreement with this, N-Cadherin and neutrophin receptors (TrkA, TrkB, TrkC), proteins involved in cell adhesion and neurite outgrowth, are the only substrates demonstrated to be directly dephosphorylated by PTPsigma and also supported *in vivo* (Faux, Hawadle et al. 2007; Siu, Fladd et al. 2007).

There are, however, several interesting potential connections of the PTPsigma neuronal phenotype with autophagy. First, over half of PTPsigma knockout mice die within two days of birth (Elchebly, Wagner et al. 1999; Wallace, Batt et al. 1999). Autophagy has been shown to be upregulated during this neonatal period to allow the newborn to survive removal from the maternal-supplied nutrient source (Kuma, Hatano et al. 2004). In support of this, a similar pattern of neonatal death has been reported in murine knockout models of Atg5 and Atg7, two important components of the autophagy machinery (Kuma, Hatano et al. 2004; Komatsu, Waguri et al. 2005). Given the balanced level of autophagy required for homeostasis, it is possible that defective autophagy, as in Atg5$^{-/-}$or Atg7$^{-/-}$ mice, as well as hyperactive autophagy, as in PTPsigma$^{-/-}$ mice, could both be detrimental during the neonatal period.

A second feature of PTPsigma neuronal function with potential implications for autophagy concerns its role in nerve regeneration. PTPsigma knockout mice have been well characterized for their enhanced regeneration in models of neuronal injury (McLean, Batt et al. 2002; Thompson, Uetani et al. 2003; Sapieha, Duplan et al. 2005). Autophagy has been implicated as a survival program in response to axon injury and thus, it is possible that PTPsigma loss promotes nerve regeneration by enhancing survival following insult (Matthews 1973; Rubinsztein, DiFiglia et al. 2005; Sternberg, Benchimol et al. 2010)

As outlined in Chapter 2 Section 1, we proceeded to assign a role for PTPsigma in autophagy, largely through characterization of the loss-of-function phenotype. In addition to abundant PI(3)P-positive vesicles, we found that knockdown increased the presence of vesicles positive for endogenous Atg12 and LC3B, two specific markers of autophagic vesicles, but did not significantly change the abundance of EEA1-positive early endosomes. This suggested that cells lacking PTPsigma had enhanced autophagy including a stage of vesicle positive for PI(3)P. We verified that autophagy was functional in these cells using lysosomal inhibitors to gauge autophagic flux, suggesting that the abundance of vesicles was not the product of a trafficking defect.

To determine if there was a potential for PTPsigma to directly regulate PI(3)P, we established its subcellular localization by tracking the D1-phosphatase domain by immunofluorescence. We uncovered that not only was PTPsigma distributed on abundant intracellular membranes, these membranes were also frequently positive for PI(3)P. When we induced autophagy in cells by amino acid starvation, we found that the numerous peripheral

PI(3)P vesicles which form, presumably of autophagic origin, were also positive for PTPsigma. In part, this close spatial association of PTPsigma and PI(3)P led us to hypothesize that PTPsigma may function as a direct PI(3)P-phosphatase.

To explore this hypothesis, we first utilized an *in silico* approach. Elegant comparative studies using crystallography and molecular docking have uncovered that the conformation of a PTP active site is a key determinant of substrate specificity (Begley, Taylor et al. 2006). The catalytic cleft of a lipid phosphatase must be uniquely deep and wide to accommodate bulky lipid head groups. In particular, the active site of a phosphoinositide phosphatase must be not only large enough to bind the hexameric inositol ring, but also wide enough to accommodate the 1′ phosphate that links the ring to a glycerol moiety (Begley, Taylor et al. 2006). To determine if the conformation of either PTPsigma active site would allow PI(3)P binding, we performed a structural docking experiment in which a PI(3)P molecule was inserted into the crystal structure of the PTPsigma catalytic domains. We discovered that the membrane-proximal D1 domain accommodated PI(3)P favorably, similar to a phosphotyrosine peptide (data not shown).

Fueled by this crystal structure revelation, we devoted considerable effort to testing the catalytic activity of PTPsigma towards PI(3)P *in vitro.* While activity could be detected at times in specific assays, we did not feel it was substantial or consistent enough to consider PTPsigma a *bona fide* lipid phosphatase. However, given the ability of the D1 active site to virtually dock PI(3)P, we cannot exclude the possibility that PTPsigma may function as a PI(3)P phosphatase *in vivo.*

Given an apparent lack of PI(3)P-phosphatase activity *in vitro* but an active site which apparently supports PI(3)P binding, we hypothesized that the active site may contribute to the targeting of PTPsigma to PI(3)P-enriched membranes via protein-lipid binding. To test this, we monitored PTPsigma localization in cells treated with wortmannin, a potent pan PI3K inhibitor which effectively depletes PI(3)P from cells. We found that the vesicular presence of PTPsigma and even its redistribution to abundant vesicles during autophagy was unaffected by wortmannin treatment. This suggests that PI(3)P presence on membranes is not required for PTPsigma targeting.

Lacking support for a PTPsigma-PI(3)P interaction, we chose to explore alternative hypotheses that PTPsigma may function in autophagy through protein-mediated mechanisms. Given the robust PI(3)P phenotype, we felt this point of regulation was likely to be close to PI(3)P. A search of a public repository of post-translational modifications revealed that several potentially phosphorylated tyrosine residues exist within Vps34 and its associated proteins. Thus, we developed a new working hypothesis that PTPsigma regulates PI(3)P by functioning as an effector of a Vps34 complex.

In support of this, we detected an interaction between PTPsigma and Vps34 as well as Rubicon, a Vps34 binding partner functioning on endocytic compartments. The subcellular localization of PTPsigma and Rubicon also largely overlapped. Upon PTPsigma knockdown, a distinct band near 100 kDa was observed to be tyrosine-phosphorylated (not so in control cells) which precipitated with the Vps34 core complex (Vps34-Vps15-Beclin1). A similar band was observed in whole cell lysates, independently of Vps34 immunoprecipitation. It is an exciting possibility that this protein may represent a phosphosubstrate of PTPsigma relevant to PI(3)P signaling. In particular, Rubicon has at least one reported phosphotyrosine site and has a predicted molecular weight of 109 kDa. Given that PTPsigma and Rubicon are capable of interacting in cells, reside primarily at the same subcellular compartments, and display very similar loss-of-function phenotypes, we generated a working model in which PTPsigma may control Vps34-PI(3)P signaling through a mechanism involving Rubicon (Figure 5.1). Here, we envision PTPsigma and Rubicon as cooperative partners functioning from the endocytic compartment as a brake pedal or checkpoint of Vps34 function. In this manner, they quench PI(3)P signaling to ensure it proceeds to a degree which is conducive to homeostasis and cell viability.

Mass spectrometry is required to identify the phosphorylated protein(s) observed in our experiments. Following, whether that substrate is Rubicon or another protein not yet considered, a detailed characterization will be required to establish this new mechanism. Potentially phosphorylated residues can be mutated by site-directed-mutagenesis in order to determine which sites are regulated by PTPsigma and importantly, are relevant to autophagy.

Proteolytic processing of PTPsigma as it relates to an autophagy function

Aside from the identification of phosphosubstrates, much work remains to elucidate the processing which controls PTPsigma and its internalization. In Chapter 2 Section 2, we determined that PTPsigma is processed by extracellular metalloproteases to a C-terminal fragment (CTF) which is targeted to and turned over within the lysosome. This CTF processing occurs in a relatively constitutive manner although, based on observations from multiple experiments, there may be a cell-density contribution to the extent of processing (data not shown). Because the PTPsigma knockdown phenotype manifests in the presence of full nutrient growth conditions and the membrane-bound CTF is most likely trafficked along the endocytic pathway, it is plausible that this CTF functions in the regulation of autophagy. From an endocytic compartment, PTPsigma could elicit control of autophagy at the point of convergence of autophagosomes and endosomes. It has been determined that this convergence, which results in the generation of hybrid organelles called amphisomes, is a frequent and important feature involved in the efficient maturation of autophagic vesicles (Fader and Colombo 2009). In agreement with this model, Rubicon knockdown was shown to elevate autophagosome abundance and autophagic (and endocytic) flux and it functions in these processes from a location on endocytic membranes (Matsunaga, Saitoh et al. 2009; Zhong, Wang et al. 2009; Sun, Westphal et al. 2010).

Intriguingly, co-immunoprecipitation experiments revealed that the interaction between PTPsigma and Vps34 is possible for not only the CTF, but the pro-protein and P-subunit as well. This interaction may simply reflect an affinity detected in the cell lysate or could reflect a more complex association of these proteins. Although less intuitive than a CTF-mediated interaction, it is possible that PTPsigma in other forms could encounter Vps34. As a type I transmembrane protein, PTPsigma is translated as a pro-protein in the ER with its phosphatase domains facing the cytosol. Given recent evidence that at least a portion of autophagic vesicles originate from PI(3)P-enriched microdomains cradled by the ER, it is possible that PTPsigma interacts with Vps34 from the ER in its pro-protein form. Also, internalization of PTPsigma without prior ectodomain shedding and CTF formation was reported and thus, PTPsigma could potentially be in proximity of Vps34 on endomembranes in full-length or P-subunit form (Aicher, Lerch et al. 1997).

In addition to the basally produced CTF, we also observed a second smaller fragment produced only during starvation-induced autophagy which did not appear to be a target of the lysosome. We previously showed that PTPsigma redistributes to a pool of abundant peripheral PI(3)P vesicles during starvation so it is possible that this unique processing accompanies the targeting of PTPsigma to this location. Identification of the fragment, be it a typical ICD or more unusual processing product, could lead to an understanding of PTPsigma activity during starvation. A combination of chemical inhibition (i.e. inhibition of metalloproteases and gamma secretase) and site-directed mutagenesis of potential sites of processing will aid in the characterization of these processing events. Of note, we attempted to mutagenize at least three sites of potential cleavage of PTPsigma and although the cloning effort was successful, we could not detect significant alterations in PTPsigma processing (data not shown). The primary difficulty in this approach is that cleavage sites are often large and not explicitly defined for PTPsigma. Thus, an improvement of this mutagenesis strategy will need to be employed and will likely require more complicated mutagenesis for efficient inhibition of processing.

Finally, identification of the signals which induce PTPsigma internalization and function in autophagy will be important. While nutrient availability regulates autophagy induction, precise mechanisms of amino acid sensing are lacking. The fact that PTPsigma knockdown cells generally mimic cells starved of amino acids in terms of autophagic phenotype could suggest a defect involving amino acid sensing. This is a relatively attractive hypothesis given PTPsigma presence at the cell surface, the interface of extracellular nutrients and cellular import (Goberdhan, Ogmundsdottir et al. 2009). However, mTOR signaling, which requires amino acids for full activation, is fully functional in these cells (data not shown). Thus, if there is a defect in amino acid sensing in the absence of PTPsigma, it would have to be impinging at more direct point in the autophagy pathway, downstream or independent of mTOR. Alternatively, as is common for receptor molecules, PTPsigma has been shown to be internalized at high cell densities, a condition reported to activate autophagy (Kisen, Tessitore et al. 1993; Wu, Yang et al. 2006). With respect to this, its regulation may involve the sensing of cell adhesion, extracellular signals, or cell-to-cell contacts. This is a reasonable potential mechanism of regulation given the large ectodomain of adhesion motifs which constitutes the E-subunit of PTPsigma.

PTPsigma in cell survival

PTPsigma has been implicated in two cancer paradigms, chemoresistance and metastatic disease. First, RNAi-mediated knockdown of PTPsigma in cultured cancer cells was reported to confer resistance to several chemotherapeutics (MacKeigan, Murphy et al. 2005). Additionally, loss of PTPsigma expression in metastatic prostate cancer was uncovered in a study of laser-captured patient tissues encompassing progressive stages of prostate malignancy (Tomlins, Mehra et al. 2007). Given the autophagic phenotype we established in the absence of PTPsigma, we hypothesized that hyperactive autophagy following its loss may provide an intracellular mechanism by which cells evade chemotherapeutic insult. In metastatic prostate cancer, this autophagic proficiency may contribute to the survival of cancer cells and ultimate progression to advanced therapy-refractory disease.

Autophagy has been shown to promote survival during stress and contribute to chemoresistance (Amaravadi, Yu et al. 2007; Carew, Nawrocki et al. 2007; Wu, Chang et al. 2010). The microenvironment of a tumor, rapidly outgrowing its blood supply, is void of nutrients and often hypoxic and this stress is exacerbated during chemotherapy. Cancer cells uniquely proficient in autophagy are able to thrive despite this cytotoxic insult. Reports have demonstrated that chemoresistant cell lines dependent upon autophagy for survival can be sensitized to death when chemotherapeutic agents are supplemented with autophagy inhibitors (Amaravadi, Yu et al. 2007; Carew, Nawrocki et al. 2007; Wu, Chang et al. 2010).

We attempted to support this model in a number of cell systems and contexts but unexpectedly, could not (data not shown). Despite clearly activated autophagy, we could not detect enhanced viability in U2OS cells transfected with PTPsigma siRNAs. Further, using HeLa cells, the model established for assaying chemoresistance, we could not demonstrate that PTPsigma knockdown favored survival in response to therapeutics. Further, using a combination of chemotherapeutics and autophagy inhibitors, we could not provide evidence to support a role for autophagy in the survival of these cells. We tested the kinetics of chemotherapeutic and autophagy inhibitor dosing but could not detect a survival advantage under any circumstance.

These findings were unexpected but do not yet negate the model put forth. Given the pivotal but bimodal function of autophagy in cell fate, this process must be exquisitely controlled to provide the most benefit to a cell. While a cell incapable of undergoing autophagy is rendered susceptible to stress and starvation -induced cell death, excessive autophagy can also contribute to cell death through the detrimental degradation of cytosolic content (Levine 2007). Given this, there is likely a tightly regulated threshold of autophagy which promotes survival versus contributes to death. This threshold may be difficult to measure and given the considerable activation of autophagy seen in PTPsigma knockdown cells, the cells may be so proficient in autophagy that a survival advantage is difficult to capture. Further, the role of PTPsigma *in vivo* with respect to autophagy signaling in a larger tissue or network is likely much more complicated than seen in our *in vitro* cell model but may be the most physiologically relevant means to testing this hypothesis. This concept is the focus of a new project in the lab and the global role of autophagy in chemoresistance and cancer progression will be explored using mouse models.

Small molecule inhibitors of PTPsigma

Although PTPsigma knockdown did not confer a survival advantage in our cell models, we undertook a project to identify small molecule inhibitors of PTPsigma nonetheless and outlined the results in Chapter 3. We felt it was useful to develop such inhibitors for several reasons. First, it has been well established, primarily through knockout animal studies, that loss of PTPsigma expression enhances neurite outgrowth and regeneration following injury (McLean, Batt et al. 2002; Thompson, Uetani et al. 2003; Sapieha, Duplan et al. 2005). Notably, it was recently found that loss of PTPsigma promotes neural regeneration following spinal cord injury (SCI), owing to the interaction of its ectodomain with chondroitin sulfate proteoglycans (CSPGs) (Shen, Tenney et al. 2009; Fry, Chagnon et al. 2010). Thus, inhibition of PTPsigma could provide a therapeutic outlet for SCI by promoting bypass of barriers normally encountered in axon regeneration. In addition, because neurodegenerative diseases are often hallmarked by the formation of toxic aggregates which can be cleared by autophagy, reducing PTPsigma activity could potentially be of use in these diseases as well (Hara, Nakamura et al. 2006; Komatsu, Waguri et al. 2006). Along these lines, PTPsigma is highly expressed in the brain, making PTPsigma an attractive central nervous system target (Pulido, Serra-Pages et al. 1995).

We coupled an *in silico* virtual ligand screening (VLS) approach with *in vitro* phosphatase assays to identify a number of small molecules which favorably bind the PTPsigma D1 active site and inhibit PTPsigma activity. Given the unique conformation of the PTPsigma active site, described above, we were surprised to find that these compounds offered no selectivity for PTPsigma when tested for inhibition of another classic PTP, PTP1B. This issue with non-selectivity is a setback commonly encountered in phosphatase drug discovery projects (Tautz, Pellecchia et al. 2006). Here, we proposed plans for a refined VLS approach which we believe will lead to the identification of PTPsigma inhibitors with selectivity. This modified method involves screening compounds *in silico* for both favorable binding to PTPsigma and negligible binding to PTP1B. This should produce a lead compound shortlist to test *in vitro* which offers an improved likelihood for selectivity.

It is possible that a selective inhibitor will not be identified easily through simple VLS alone. Instead, we may need to utilize a detailed analysis of the PTPsigma crystal structure to identify and exploit key residues involved in substrate, and inhibitor, binding. The high degree of conservation of PTPs may necessitate this approach and will likely help drive the identification of a selective compound. It may also be required that an inhibitor be directed to regions outside the PTPsigma active site. For instance, effective and selective inhibitors of PTP1B have been developed which target both the active site and an adjacent, less conserved, binding pocket (Shen, Keng et al. 2001; Zhang 2002; Sun, Fedorov et al. 2003). It is possible that similar adjacent regions exist within PTPsigma and could be exploited in the development of an inhibitor.

Mathematical models of autophagy

The third aim of this project, and focus of Chapter 4 of this thesis, has undergone considerable evolution since its origins as a mere thought-process. In fact, the plausibility that this modeling effort would generate a useful and relevant framework for studying autophagy seemed remote at times. Because the field of Systems Biology, founded on the acquisition of comprehensive datasets and computation models to analyze such data, is still in its infancy, efforts within this discipline are not always straightforward. Setbacks in this project, if only mental, are reflected in the following quote from Hiroaki Kitano, a pioneer in Systems Biology:

"'The toughness of systems approaches has constrained the field's growth,' says Kitano… 'Genomics exploded, because if you buy a sequencing machine, anyone can do it,' he says. 'But having to combine good biology with good mathematical modeling isn't easy" (Macilwain 2011).

Our primary aim was to develop a model which was driven largely from data collected experimentally. That is, instead of constructing a model based on data selectively chosen from the literature and based entirely on assumptions, we aimed to build a model built and refined using reliable cell-based data. While we initially envisioned a large rule-based model which would encompass mTOR/PI3K/Akt pathway signaling and all known PI(3)P-dependent processes, utilizing data captured from several pathway nodes, we quickly realized that this was an impractical starting point. Instead, we chose to focus on our central interest, autophagic vesicle dynamics, and drive the model with high-quality kinetic measurements of GFP-LC3 dynamics. Because this model was smaller than originally intended, we described it using a set of chemical reactions and stochastic simulation instead of rule-based specification, which is optimal for larger signaling networks.

This initial model of autophagy dynamics, captured with single cell resolution and across a number of cellular conditions, accurately predicted responses to both Atg9 knockdown and Vps34 inhibition. Further, the model produced a novel hypothesis that LC3 concentrations positively correlate with autophagic vesicle size. While we did not test this prediction experimentally, we found evidence in its support from both yeast and mammalian systems (Nakagawa, Amano et al. 2004; Xie, Nair et al. 2008). This highlights the accuracy and potential utility of this model outside our isolated cell system.

We intend to expand upon this simple model through generation of a more comprehensive autophagy network framework. This model will include all known molecules involved in autophagy, including more than 30 autophagy genes and numerous other molecules involved in its function. The model will depict regulation upstream, including mTORC1, as well as describe molecular details underlying vesicle dynamics (for example, the multiple processing steps required to prime and process LC3 for vesicle conjugation). Inclusion of these details may reveal features of the model not observed in its earlier version. With this goal in mind, we have already constructed a contact map, a diagrammatic depiction of the entire autophagy process with model features (e.g. proteins, complexes, modifiable residues, activations) drawn using universally defined format (portion of the map shown in Figure 5.2).

A comprehensive model of autophagy dynamics which is predictive will have considerable utility. As autophagy is an essential regulator of cell fate, contributing to both cell survival during stress and participating in cell death in certain contexts, it is of great interest to disease-centric translation research. In particular, being able to predict how a specific genetic alteration (e.g. an oncogenic mutation defining a cancer subtype) or selective enzyme inhibition will affect this process will be informative for the design of molecularly targeted therapies (Hopkins 2008).

FIGURES

Figure 5.1. Working model of PTPsigma function. Given data presented here, we present a potential model of PTPsigma function in PI(3)P signaling. Support for this concept includes 1) co-immunoprecipitation of PTPsigma with Vps34 and Rubicon, 2) similar vesicular localization pattern of PTPsigma and Rubicon, 3) similar loss-of-function phenotypes of PTPsigma and Rubicon, and 4) and altered phosphorylation associated with the Vps34 complex in the absence of PTPsigma. The Vps34 complex associated with Rubicon may include other binding partners (Vps15, Rab5, Beclin1, UVRAG, Rubicon) although the inclusion of Beclin1 at the endosome has not been established. The interactions between Beclin1, Vps34, Rubicon, and UVRAG which participate in endocytosis and autophagy are dynamic and only beginning to be elucidated. Evidence supports a model whereby PTPsigma is processed into a C-terminal fragment (CTF) in the presence of nutrients and targeted to the lysosome. As the CTF is membrane tethered, it presumably travels along endocytic vesicles where it can encounter the Vps34 complex (dashed lines indicate evidence that exogenous PTPsigma can interact with Vps34 and Rubicon via co-immunoprecipitation experiments) and PI(3)P , be it at the endosome or amphisome (fusion of an endosome and autophagosome), where it functions the regulation of this signaling axis. Proteins with evidence of tyrosine phosphorylation are indicated with asterisks (outlined in Table 2.2).

Figure 5.1 (cont'd)

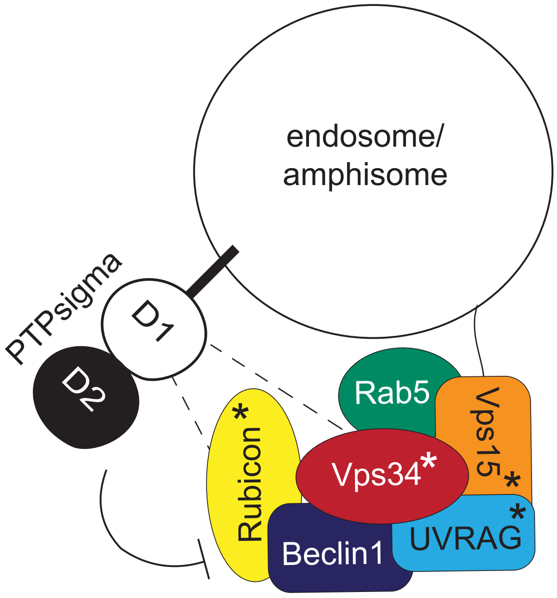

Figure 5.2. Contact map of the mammalian autophagy network. Figure depicts a portion of the complete contact map of all molecules and interactions included in a rule-based model of autophagy signaling. Specifically, this portion includes the mTORC1 and ULK1 complexes. Double arrowed lines indicate noncovalent binding, open circles point to targets of catalysis (phosphorylation or nucleotide exchange; a slash indicates dephosphorylation), and small squares indicate residues which can be modified within molecules [amino acids that can be phosphorylated (tyrosine, threonine and serine), mutated, or used for covalent attachment]. “pS/T(a)” indicates activating phosphorylation of a serine or threonine residue; “pS/T(i)” indicates inhibitory phosphorylation of a serine or threonine residue. Cellular locations are indicated by squares attached to molecules: C = diffusing in cytoplasm, L = lysosome.

Figure 5.2 (cont'd)

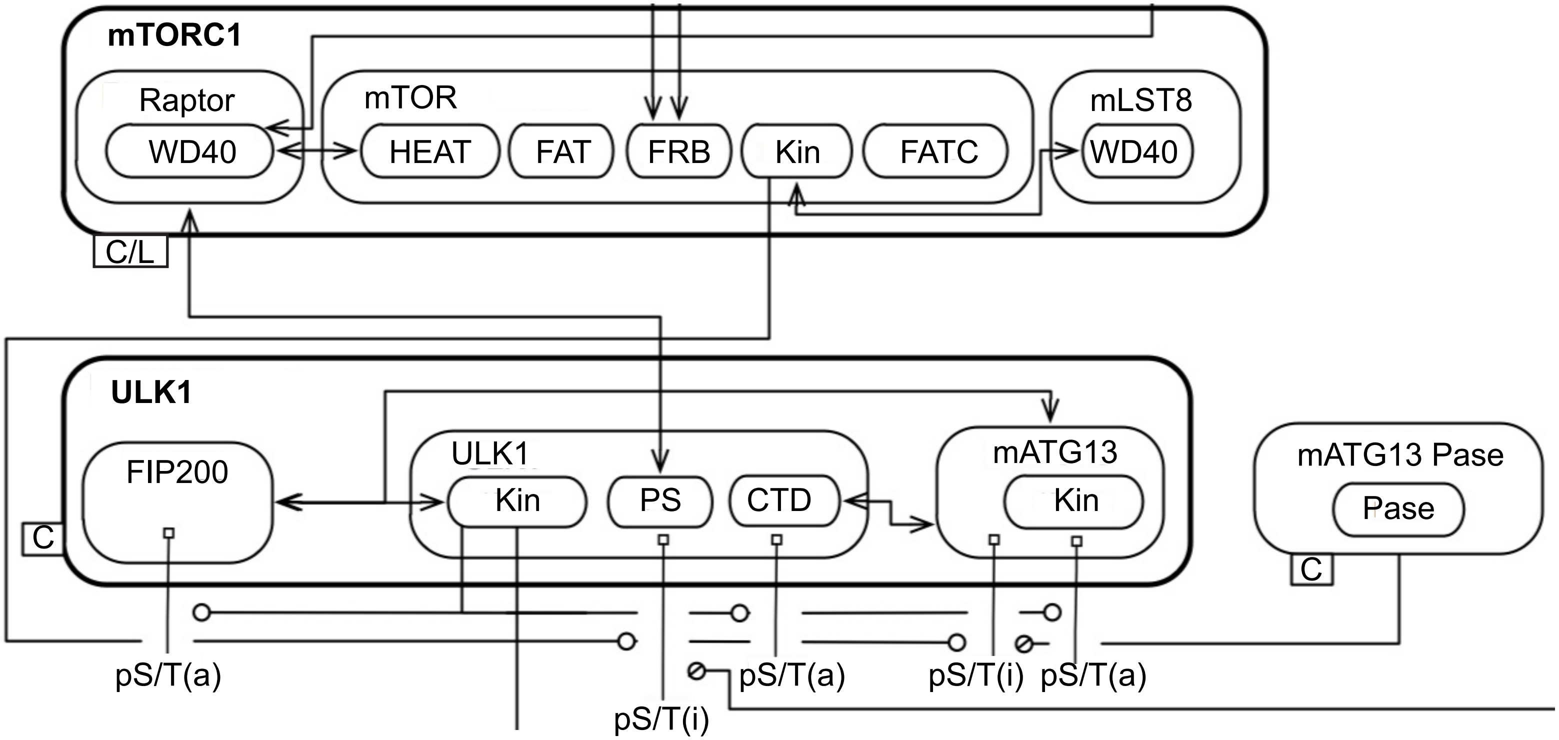

REFERENCES

REFERENCES

Abaan, O. D. and J. A. Toretsky (2008). "PTPL1: a large phosphatase with a split personality." Cancer Metastasis Rev **27**(2): 205-214.

Aicher, B., M. M. Lerch, et al. (1997). "Cellular redistribution of protein tyrosine phosphatases LAR and PTPsigma by inducible proteolytic processing." J Cell Biol **138**(3): 681-696.

Almo, S. C., J. B. Bonanno, et al. (2007). "Structural genomics of protein phosphatases." J Struct Funct Genomics **8**(2-3): 121-140.

Amaravadi, R. K., D. Yu, et al. (2007). "Autophagy inhibition enhances therapy-induced apoptosis in a Myc-induced model of lymphoma." J Clin Invest **117**(2): 326-336.

Andersen, J. N., O. H. Mortensen, et al. (2001). "Structural and evolutionary relationships among protein tyrosine phosphatase domains." Mol Cell Biol **21**(21): 7117-7136.

Araki, T., M. G. Mohi, et al. (2004). "Mouse model of Noonan syndrome reveals cell type- and gene dosage-dependent effects of Ptpn11 mutation." Nat Med **10**(8): 849-857.

Aricescu, A. R., I. W. McKinnell, et al. (2002). "Heparan sulfate proteoglycans are ligands for receptor protein tyrosine phosphatase sigma." Mol Cell Biol **22**(6): 1881-1892.

Axe, E. L., S. A. Walker, et al. (2008). "Autophagosome formation from membrane compartments enriched in phosphatidylinositol 3-phosphate and dynamically connected to the endoplasmic reticulum." J Cell Biol **182**(4): 685-701.

Backer, J. M. (2008). "The regulation and function of Class III PI3Ks: novel roles for Vps34." Biochem J **410**(1): 1-17.

Begley, M. J., G. S. Taylor, et al. (2006). "Molecular basis for substrate recognition by MTMR2, a myotubularin family phosphoinositide phosphatase." Proc Natl Acad Sci U S A **103**(4): 927-932.

Berg, T. O., M. Fengsrud, et al. (1998). "Isolation and characterization of rat liver amphisomes. Evidence for fusion of autophagosomes with both early and late endosomes." J Biol Chem **273**(34): 21883-21892.

Bird, I. M. (1994). "Analysis of cellular phosphoinositides and phosphoinositols by extraction and simple analytical procedures." Methods Mol Biol **27**: 227-248.

Blinov, M. L., J. R. Faeder, et al. (2004). "BioNetGen: software for rule-based modeling of signal transduction based on the interactions of molecular domains." Bioinformatics **20**(17): 3289-3291.

Blinov, M. L., J. R. Faeder, et al. (2006). "A network model of early events in epidermal growth factor receptor signaling that accounts for combinatorial complexity." Biosystems **83**(2-3): 136-151.

Blondeau, F., J. Laporte, et al. (2000). "Myotubularin, a phosphatase deficient in myotubular myopathy, acts on phosphatidylinositol 3-kinase and phosphatidylinositol 3-phosphate pathway." Hum Mol Genet **9**(15): 2223-2229.

Bova, M. P., M. N. Mattson, et al. (2004). "The oxidative mechanism of action of ortho-quinone inhibitors of protein-tyrosine phosphatase alpha is mediated by hydrogen peroxide." Arch Biochem Biophys **429**(1): 30-41.

Byfield, M. P., J. T. Murray, et al. (2005). "hVps34 is a nutrient-regulated lipid kinase required for activation of p70 S6 kinase." J Biol Chem **280**(38): 33076-33082.

Carew, J. S., S. T. Nawrocki, et al. (2007). "Modulating autophagy for therapeutic benefit." Autophagy **3**(5): 464-467.

Chan, G., D. Kalaitzidis, et al. (2008). "The tyrosine phosphatase Shp2 (PTPN11) in cancer." Cancer Metastasis Rev **27**(2): 179-192.

Chang, Y. Y. and T. P. Neufeld (2009). "An Atg1/Atg13 complex with multiple roles in TOR-mediated autophagy regulation." Mol Biol Cell **20**(7): 2004-2014.

Christoforidis, S., M. Miaczynska, et al. (1999). "Phosphatidylinositol-3-OH kinases are Rab5 effectors." Nat Cell Biol **1**(4): 249-252.

Codogno, P. and A. J. Meijer (2005). "Autophagy and signaling: their role in cell survival and cell death." Cell Death Differ **12 Suppl 2**: 1509-1518.

Domin, J., F. Pages, et al. (1997). "Cloning of a human phosphoinositide 3-kinase with a C2 domain that displays reduced sensitivity to the inhibitor wortmannin." Biochem J **326 (Pt 1)**: 139-147.

Dromard, M., G. Bompard, et al. (2007). "The putative tumor suppressor gene PTPN13/PTPL1 induces apoptosis through insulin receptor substrate-1 dephosphorylation." Cancer Res **67**(14): 6806-6813.

Dunn, W. A., Jr. (1990). "Studies on the mechanisms of autophagy: maturation of the autophagic vacuole." J Cell Biol **110**(6): 1935-1945.

Elchebly, M., J. Wagner, et al. (1999). "Neuroendocrine dysplasia in mice lacking protein tyrosine phosphatase sigma." Nat Genet **21**(3): 330-333.

Endy, D. and R. Brent (2001). "Modelling cellular behaviour." Nature **409**(6818): 391-395.

Fader, C. M. and M. I. Colombo (2009). "Autophagy and multivesicular bodies: two closely related partners." Cell Death Differ **16**(1): 70-78.

Faeder, J. R., M. L. Blinov, et al. (2005). "Combinatorial complexity and dynamical restriction of network flows in signal transduction." Syst Biol (Stevenage) **2**(1): 5-15.

Fan, W., A. Nassiri, et al. (2011). "Autophagosome targeting and membrane curvature sensing by Barkor/Atg14(L)." Proc Natl Acad Sci U S A **108**(19): 7769-7774.

Faux, C., M. Hawadle, et al. (2007). "PTPsigma binds and dephosphorylates neurotrophin receptors and can suppress NGF-dependent neurite outgrowth from sensory neurons." Biochim Biophys Acta **1773**(11): 1689-1700.

Fry, E. J., M. J. Chagnon, et al. (2010). "Corticospinal tract regeneration after spinal cord injury in receptor protein tyrosine phosphatase sigma deficient mice." Glia **58**(4): 423-433.

Fujita, N., T. Itoh, et al. (2008). "The Atg16L complex specifies the site of LC3 lipidation for membrane biogenesis in autophagy." Mol Biol Cell **19**(5): 2092-2100.

Funderburk, S. F., Q. J. Wang, et al. (2010). "The Beclin 1-VPS34 complex--at the crossroads of autophagy and beyond." Trends Cell Biol **20**(6): 355-362.

Futter, C. E., L. M. Collinson, et al. (2001). "Human VPS34 is required for internal vesicle formation within multivesicular endosomes." J Cell Biol **155**(7): 1251-1264.

Ganley, I. G., H. Lam du, et al. (2009). "ULK1.ATG13.FIP200 complex mediates mTOR signaling and is essential for autophagy." J Biol Chem **284**(18): 12297-12305.

Gao, W., J. H. Kang, et al. (2010). "Biochemical isolation and characterization of the tubulovesicular LC3-positive autophagosomal compartment." J Biol Chem **285**(2): 1371-1383.

Gaullier, J. M., A. Simonsen, et al. (1998). "FYVE fingers bind PtdIns(3)P." Nature **394**(6692): 432-433.

Gillooly, D. J., I. C. Morrow, et al. (2000). "Localization of phosphatidylinositol 3-phosphate in yeast and mammalian cells." EMBO J **19**(17): 4577-4588.

Goberdhan, D. C., M. H. Ogmundsdottir, et al. (2009). "Amino acid sensing and mTOR regulation: inside or out?" Biochem Soc Trans **37**(Pt 1): 248-252.

Goldstein, B., J. R. Faeder, et al. (2004). "Mathematical and computational models of immune-receptor signalling." Nat Rev Immunol **4**(6): 445-456.

Guan, K. L. and J. E. Dixon (1991). "Eukaryotic proteins expressed in Escherichia coli: an improved thrombin cleavage and purification procedure of fusion proteins with glutathione S-transferase." Anal Biochem **192**(2): 262-267.

Gupta-Rossi, N., E. Six, et al. (2004). "Monoubiquitination and endocytosis direct gamma-secretase cleavage of activated Notch receptor." J Cell Biol **166**(1): 73-83.

Haapasalo, A., D. Y. Kim, et al. (2007). "Presenilin/gamma-secretase-mediated cleavage regulates association of leukocyte-common antigen-related (LAR) receptor tyrosine phosphatase with beta-catenin." J Biol Chem **282**(12): 9063-9072.

Hanada, T., N. N. Noda, et al. (2007). "The Atg12-Atg5 conjugate has a novel E3-like activity for protein lipidation in autophagy." J Biol Chem **282**(52): 37298-37302.

Hara, T., K. Nakamura, et al. (2006). "Suppression of basal autophagy in neural cells causes neurodegenerative disease in mice." Nature **441**(7095): 885-889.

Hayashi-Nishino, M., N. Fujita, et al. (2009). "A subdomain of the endoplasmic reticulum forms a cradle for autophagosome formation." Nat Cell Biol **11**(12): 1433-1437.

He, C., M. Baba, et al. (2008). "Self-interaction is critical for Atg9 transport and function at the phagophore assembly site during autophagy." Mol Biol Cell **19**(12): 5506-5516.

Herman, P. K. and S. D. Emr (1990). "Characterization of VPS34, a gene required for vacuolar protein sorting and vacuole segregation in Saccharomyces cerevisiae." Mol Cell Biol **10**(12): 6742-6754.

Hlavacek, W. S., J. R. Faeder, et al. (2006). "Rules for modeling signal-transduction systems." Sci STKE **2006**(344): re6.

Hopkins, A. L. (2008). "Network pharmacology: the next paradigm in drug discovery." Nat Chem Biol **4**(11): 682-690.

Hosokawa, N., T. Hara, et al. (2009). "Nutrient-dependent mTORC1 association with the ULK1-Atg13-FIP200 complex required for autophagy." Mol Biol Cell **20**(7): 1981-1991.

Ichimura, Y., T. Kirisako, et al. (2000). "A ubiquitin-like system mediates protein lipidation." Nature **408**(6811): 488-492.

Imami, K., N. Sugiyama, et al. (2008). "Automated phosphoproteome analysis for cultured cancer cells by two-dimensional nanoLC-MS using a calcined titania/C18 biphasic column." Anal Sci **24**(1): 161-166.

Irwin, J. J. and B. K. Shoichet (2005). "ZINC--a free database of commercially available compounds for virtual screening." J Chem Inf Model **45**(1): 177-182.

Itakura, E., C. Kishi, et al. (2008). "Beclin 1 forms two distinct phosphatidylinositol 3-kinase complexes with mammalian Atg14 and UVRAG." Mol Biol Cell **19**(12): 5360-5372.

Janes, K. A. and M. B. Yaffe (2006). "Data-driven modelling of signal-transduction networks." Nat Rev Mol Cell Biol **7**(11): 820-828.

Juhasz, G., J. H. Hill, et al. (2008). "The class III PI(3)K Vps34 promotes autophagy and endocytosis but not TOR signaling in Drosophila." J Cell Biol **181**(4): 655-666.

Jung, C. H., C. B. Jun, et al. (2009). "ULK-Atg13-FIP200 complexes mediate mTOR signaling to the autophagy machinery." Mol Biol Cell **20**(7): 1992-2003.

Kabeya, Y., N. Mizushima, et al. (2000). "LC3, a mammalian homologue of yeast Apg8p, is localized in autophagosome membranes after processing." EMBO J **19**(21): 5720-5728.

Kholodenko, B. N., O. V. Demin, et al. (1999). "Quantification of short term signaling by the epidermal growth factor receptor." J Biol Chem **274**(42): 30169-30181.

Kholodenko, B. N., J. F. Hancock, et al. (2010). "Signalling ballet in space and time." Nat Rev Mol Cell Biol **11**(6): 414-426.

Kihara, A., T. Noda, et al. (2001). "Two distinct Vps34 phosphatidylinositol 3-kinase complexes function in autophagy and carboxypeptidase Y sorting in Saccharomyces cerevisiae." J Cell Biol **152**(3): 519-530.

Kimura, S., T. Noda, et al. (2007). "Dissection of the autophagosome maturation process by a novel reporter protein, tandem fluorescent-tagged LC3." Autophagy **3**(5): 452-460.

Kirisako, T., Y. Ichimura, et al. (2000). "The reversible modification regulates the membrane-binding state of Apg8/Aut7 essential for autophagy and the cytoplasm to vacuole targeting pathway." J Cell Biol **151**(2): 263-276.

Kirschner, M. W. (2005). "The meaning of systems biology." Cell **121**(4): 503-504.

Kisen, G. O., L. Tessitore, et al. (1993). "Reduced autophagic activity in primary rat hepatocellular carcinoma and ascites hepatoma cells." Carcinogenesis **14**(12): 2501-2505.

Kitano, H. (2002). "Computational systems biology." Nature **420**(6912): 206-210.

Kitano, H. (2002). "Systems biology: a brief overview." Science **295**(5560): 1662-1664.

Kitchen, D. B., H. Decornez, et al. (2004). "Docking and scoring in virtual screening for drug discovery: methods and applications." Nat Rev Drug Discov **3**(11): 935-949.

Klionsky, D. J. (2007). "Autophagy: from phenomenology to molecular understanding in less than a decade." Nat Rev Mol Cell Biol **8**(11): 931-937.

Klionsky, D. J., H. Abeliovich, et al. (2008). "Guidelines for the use and interpretation of assays for monitoring autophagy in higher eukaryotes." Autophagy **4**(2): 151-175.

Komatsu, M., S. Waguri, et al. (2006). "Loss of autophagy in the central nervous system causes neurodegeneration in mice." Nature **441**(7095): 880-884.

Komatsu, M., S. Waguri, et al. (2005). "Impairment of starvation-induced and constitutive autophagy in Atg7-deficient mice." J Cell Biol **169**(3): 425-434.

Kontaridis, M. I., K. D. Swanson, et al. (2006). "PTPN11 (Shp2) mutations in LEOPARD syndrome have dominant negative, not activating, effects." J Biol Chem **281**(10): 6785-6792.

Krueger, N. X., D. Van Vactor, et al. (1996). "The transmembrane tyrosine phosphatase DLAR controls motor axon guidance in Drosophila." Cell **84**(4): 611-622.

Kuma, A., M. Hatano, et al. (2004). "The role of autophagy during the early neonatal starvation period." Nature **432**(7020): 1032-1036.

Lahiry, P., A. Torkamani, et al. (2010). "Kinase mutations in human disease: interpreting genotype-phenotype relationships." Nat Rev Genet **11**(1): 60-74.

Ledig, M. M., F. Haj, et al. (1999). "The receptor tyrosine phosphatase CRYPalpha promotes intraretinal axon growth." J Cell Biol **147**(2): 375-388.

Levine, B. (2007). "Cell biology: autophagy and cancer." Nature **446**(7137): 745-747.

Li, H., Z. Ren, et al. (2009). "Identification of tyrosine-phosphorylated proteins associated with metastasis and functional analysis of FER in human hepatocellular carcinoma cells." BMC Cancer **9**: 366.

Liang, C., P. Feng, et al. (2006). "Autophagic and tumour suppressor activity of a novel Beclin1-binding protein UVRAG." Nat Cell Biol **8**(7): 688-699.

Liang, C., J. S. Lee, et al. (2008). "Beclin1-binding UVRAG targets the class C Vps complex to coordinate autophagosome maturation and endocytic trafficking." Nat Cell Biol **10**(7): 776-787.

Lorenzo, O., S. Urbe, et al. (2006). "Systematic analysis of myotubularins: heteromeric interactions, subcellular localisation and endosome related functions." J Cell Sci **119**(Pt 14): 2953-2959.

Macilwain, C. (2011). "Systems biology: evolving into the mainstream." Cell **144**(6): 839-841.

MacKeigan, J. P., L. O. Murphy, et al. (2005). "Sensitized RNAi screen of human kinases and phosphatases identifies new regulators of apoptosis and chemoresistance." Nat Cell Biol **7**(6): 591-600.

Manning, B. D. and L. C. Cantley (2007). "AKT/PKB signaling: navigating downstream." Cell **129**(7): 1261-1274.

Martin, K. R., Y. Xu, et al. (2011). "Identification of PTPsigma as an autophagic phosphatase." J Cell Sci **124**(Pt 5): 812-819.

Matsunaga, K., T. Saitoh, et al. (2009). "Two Beclin 1-binding proteins, Atg14L and Rubicon, reciprocally regulate autophagy at different stages." Nat Cell Biol **11**(4): 385-396.

Matthews, M. R. (1973). "An ultrastructural study of axonal changes following constriction of postganglionic branches of the superior cervical ganglion in the rat." Philos Trans R Soc Lond B Biol Sci **264**(866): 479-505.

Mattila, E. and J. Ivaska (2011). "High-throughput methods in identification of protein tyrosine phosphatase inhibitors and activators." Anticancer Agents Med Chem **11**(1): 141-150.

McLean, J., J. Batt, et al. (2002). "Enhanced rate of nerve regeneration and directional errors after sciatic nerve injury in receptor protein tyrosine phosphatase sigma knock-out mice." J Neurosci **22**(13): 5481-5491.

Meijer, A. J. and P. Codogno (2004). "Regulation and role of autophagy in mammalian cells." Int J Biochem Cell Biol **36**(12): 2445-2462.

Mizushima, N., T. Noda, et al. (1998). "A protein conjugation system essential for autophagy." Nature **395**(6700): 395-398.

Mizushima, N., A. Yamamoto, et al. (2001). "Dissection of autophagosome formation using Apg5-deficient mouse embryonic stem cells." J Cell Biol **152**(4): 657-668.

Mohi, M. G. and B. G. Neel (2007). "The role of Shp2 (PTPN11) in cancer." Curr Opin Genet Dev **17**(1): 23-30.

Mohi, M. G., I. R. Williams, et al. (2005). "Prognostic, therapeutic, and mechanistic implications of a mouse model of leukemia evoked by Shp2 (PTPN11) mutations." Cancer Cell **7**(2): 179-191.

Murray, J. T., C. Panaretou, et al. (2002). "Role of Rab5 in the recruitment of hVps34/p150 to the early endosome." Traffic **3**(6): 416-427.

Nakagawa, I., A. Amano, et al. (2004). "Autophagy defends cells against invading group A Streptococcus." Science **306**(5698): 1037-1040.

Nobukuni, T., M. Joaquin, et al. (2005). "Amino acids mediate mTOR/raptor signaling through activation of class 3 phosphatidylinositol 3OH-kinase." Proc Natl Acad Sci U S A **102**(40): 14238-14243.

Obara, K., T. Noda, et al. (2008). "Transport of phosphatidylinositol 3-phosphate into the vacuole via autophagic membranes in Saccharomyces cerevisiae." Genes Cells **13**(6): 537-547.

Obara, K., T. Sekito, et al. (2008). "The Atg18-Atg2 complex is recruited to autophagic membranes via phosphatidylinositol 3-phosphate and exerts an essential function." J Biol Chem **283**(35): 23972-23980.

Ohsumi, Y. and N. Mizushima (2004). "Two ubiquitin-like conjugation systems essential for autophagy." Semin Cell Dev Biol **15**(2): 231-236.

Petiot, A., E. Ogier-Denis, et al. (2000). "Distinct classes of phosphatidylinositol 3'-kinases are involved in signaling pathways that control macroautophagy in HT-29 cells." J Biol Chem **275**(2): 992-998.

Polson, H. E., J. de Lartigue, et al. (2010). "Mammalian Atg18 (WIPI2) localizes to omegasome-anchored phagophores and positively regulates LC3 lipidation." Autophagy **6**(4).

Proikas-Cezanne, T., S. Ruckerbauer, et al. (2007). "Human WIPI-1 puncta-formation: a novel assay to assess mammalian autophagy." FEBS Lett **581**(18): 3396-3404.

Proikas-Cezanne, T., S. Waddell, et al. (2004). "WIPI-1alpha (WIPI49), a member of the novel 7-bladed WIPI protein family, is aberrantly expressed in human cancer and is linked to starvation-induced autophagy." Oncogene **23**(58): 9314-9325.

Pulido, R., C. Serra-Pages, et al. (1995). "The LAR/PTP delta/PTP sigma subfamily of transmembrane protein-tyrosine-phosphatases: multiple human LAR, PTP delta, and PTP sigma isoforms are expressed in a tissue-specific manner and associate with the LAR-interacting protein LIP.1." Proc Natl Acad Sci U S A **92**(25): 11686-11690.

Rashid-Doubell, F., I. McKinnell, et al. (2002). "Chick PTPsigma regulates the targeting of retinal axons within the optic tectum." J Neurosci **22**(12): 5024-5033.

Reggiori, F., K. A. Tucker, et al. (2004). "The Atg1-Atg13 complex regulates Atg9 and Atg23 retrieval transport from the pre-autophagosomal structure." Dev Cell **6**(1): 79-90.

Rubinsztein, D. C., M. DiFiglia, et al. (2005). "Autophagy and its possible roles in nervous system diseases, damage and repair." Autophagy **1**(1): 11-22.

Ruhe, J. E., S. Streit, et al. (2006). "EGFR signaling leads to downregulation of PTP-LAR via TACE-mediated proteolytic processing." Cell Signal **18**(9): 1515-1527.

Rutherford, A. C., C. Traer, et al. (2006). "The mammalian phosphatidylinositol 3-phosphate 5-kinase (PIKfyve) regulates endosome-to-TGN retrograde transport." J Cell Sci **119**(Pt 19): 3944-3957.

Sajnani, G., A. R. Aricescu, et al. (2005). "PTPsigma promotes retinal neurite outgrowth non-cell-autonomously." J Neurobiol **65**(1): 59-71.

Salmeen, A., J. N. Andersen, et al. (2003). "Redox regulation of protein tyrosine phosphatase 1B involves a sulphenyl-amide intermediate." Nature **423**(6941): 769-773.

Samuels, Y., Z. Wang, et al. (2004). "High frequency of mutations of the PIK3CA gene in human cancers." Science **304**(5670): 554.

Sapieha, P. S., L. Duplan, et al. (2005). "Receptor protein tyrosine phosphatase sigma inhibits axon regrowth in the adult injured CNS." Mol Cell Neurosci **28**(4): 625-635.

Sarkar, S., R. A. Floto, et al. (2005). "Lithium induces autophagy by inhibiting inositol monophosphatase." J Cell Biol **170**(7): 1101-1111.

Schu, P. V., K. Takegawa, et al. (1993). "Phosphatidylinositol 3-kinase encoded by yeast VPS34 gene essential for protein sorting." Science **260**(5104): 88-91.

Shen, K., Y. F. Keng, et al. (2001). "Acquisition of a specific and potent PTP1B inhibitor from a novel combinatorial library and screening procedure." J Biol Chem **276**(50): 47311-47319.

Shen, Y., A. P. Tenney, et al. (2009). "PTPsigma is a receptor for chondroitin sulfate proteoglycan, an inhibitor of neural regeneration." Science **326**(5952): 592-596.

Simonsen, A., R. Lippe, et al. (1998). "EEA1 links PI(3)K function to Rab5 regulation of endosome fusion." Nature **394**(6692): 494-498.

Siu, R., C. Fladd, et al. (2007). "N-cadherin is an in vivo substrate for protein tyrosine phosphatase sigma (PTPsigma) and participates in PTPsigma-mediated inhibition of axon growth." Mol Cell Biol **27**(1): 208-219.

Spencer, S. L. and P. K. Sorger (2011). "Measuring and modeling apoptosis in single cells." Cell **144**(6): 926-939.

Spiller, D. G., C. D. Wood, et al. (2010). "Measurement of single-cell dynamics." Nature **465**(7299): 736-745.

Stack, J. H., P. K. Herman, et al. (1993). "A membrane-associated complex containing the Vps15 protein kinase and the Vps34 PI 3-kinase is essential for protein sorting to the yeast lysosome-like vacuole." EMBO J **12**(5): 2195-2204.

Sternberg, C., M. Benchimol, et al. (2010). "Caspase dependence of the death of neonatal retinal ganglion cells induced by axon damage and induction of autophagy as a survival mechanism." Braz J Med Biol Res **43**(10): 950-956.

Sun, J. P., A. A. Fedorov, et al. (2003). "Crystal structure of PTP1B complexed with a potent and selective bidentate inhibitor." J Biol Chem **278**(14): 12406-12414.

Sun, Q., W. Fan, et al. (2008). "Identification of Barkor as a mammalian autophagy-specific factor for Beclin 1 and class III phosphatidylinositol 3-kinase." Proc Natl Acad Sci U S A **105**(49): 19211-19216.

Sun, Q., W. Westphal, et al. (2010). "Rubicon controls endosome maturation as a Rab7 effector." Proc Natl Acad Sci U S A **107**(45): 19338-19343.

Sun, Q., J. Zhang, et al. (2011). "The RUN domain of rubicon is important for hVps34 binding, lipid kinase inhibition, and autophagy suppression." J Biol Chem **286**(1): 185-191.

Suzuki, K., T. Kirisako, et al. (2001). "The pre-autophagosomal structure organized by concerted functions of APG genes is essential for autophagosome formation." EMBO J **20**(21): 5971-5981.

Taguchi-Atarashi, N., M. Hamasaki, et al. (2010). "Modulation of local PtdIns3P levels by the PI phosphatase MTMR3 regulates constitutive autophagy." Traffic **11**(4): 468-478.

Tanida, I., N. Minematsu-Ikeguchi, et al. (2005). "Lysosomal turnover, but not a cellular level, of endogenous LC3 is a marker for autophagy." Autophagy **1**(2): 84-91.

Tautz, L. and T. Mustelin (2007). "Strategies for developing protein tyrosine phosphatase inhibitors." Methods **42**(3): 250-260.

Tautz, L., M. Pellecchia, et al. (2006). "Targeting the PTPome in human disease." Expert Opin Ther Targets **10**(1): 157-177.

Tay, S., J. J. Hughey, et al. (2010). "Single-cell NF-kappaB dynamics reveal digital activation and analogue information processing." Nature **466**(7303): 267-271.

Thompson, K. M., N. Uetani, et al. (2003). "Receptor protein tyrosine phosphatase sigma inhibits axonal regeneration and the rate of axon extension." Mol Cell Neurosci **23**(4): 681-692.

Tierno, M. B., P. A. Johnston, et al. (2007). "Development and optimization of high-throughput in vitro protein phosphatase screening assays." Nat Protoc **2**(5): 1134-1144.

Tomlins, S. A., R. Mehra, et al. (2007). "Integrative molecular concept modeling of prostate cancer progression." Nat Genet **39**(1): 41-51.

Tonks, N. K. (2005). "Redox redux: revisiting PTPs and the control of cell signaling." Cell **121**(5): 667-670.

Tonks, N. K. (2006). "Protein tyrosine phosphatases: from genes, to function, to disease." Nat Rev Mol Cell Biol **7**(11): 833-846.

Uetani, N., M. J. Chagnon, et al. (2006). "Mammalian motoneuron axon targeting requires receptor protein tyrosine phosphatases sigma and delta." J Neurosci **26**(22): 5872-5880.

Uetani, N., K. Kato, et al. (2000). "Impaired learning with enhanced hippocampal long-term potentiation in PTPdelta-deficient mice." EMBO J **19**(12): 2775-2785.

Urbanek, R. A., S. J. Suchard, et al. (2001). "Potent reversible inhibitors of the protein tyrosine phosphatase CD45." J Med Chem **44**(11): 1777-1793.

Van Lieshout, E. M., I. Van der Heijden, et al. (2001). "A decrease in size and number of basal forebrain cholinergic neurons is paralleled by diminished hippocampal cholinergic innervation in mice lacking leukocyte common antigen-related protein tyrosine phosphatase activity." Neuroscience **102**(4): 833-841.

Vergne, I., E. Roberts, et al. (2009). "Control of autophagy initiation by phosphoinositide 3-phosphatase jumpy." EMBO J **28**(15): 2244-2258.

Wallace, M. J., J. Batt, et al. (1999). "Neuronal defects and posterior pituitary hypoplasia in mice lacking the receptor tyrosine phosphatase PTPsigma." Nat Genet **21**(3): 334-338.

Walsh, J. P., K. K. Caldwell, et al. (1991). "Formation of phosphatidylinositol 3-phosphate by isomerization from phosphatidylinositol 4-phosphate." Proc Natl Acad Sci U S A **88**(20): 9184-9187.

Webber, J. L. and S. A. Tooze (2010). "New insights into the function of Atg9." FEBS Lett **584**(7): 1319-1326.

Wiley, H. S., S. Y. Shvartsman, et al. (2003). "Computational modeling of the EGF-receptor system: a paradigm for systems biology." Trends Cell Biol **13**(1): 43-50.

Wu, H., J. M. Yang, et al. (2006). "Elongation factor-2 kinase regulates autophagy in human glioblastoma cells." Cancer Res **66**(6): 3015-3023.

Wu, Z., P. C. Chang, et al. (2010). "Autophagy Blockade Sensitizes Prostate Cancer Cells towards Src Family Kinase Inhibitors." Genes Cancer **1**(1): 40-49.

Xie, Z., U. Nair, et al. (2008). "Atg8 controls phagophore expansion during autophagosome formation." Mol Biol Cell **19**(8): 3290-3298.

Yeo, T. T., T. Yang, et al. (1997). "Deficient LAR expression decreases basal forebrain cholinergic neuronal size and hippocampal cholinergic innervation." J Neurosci Res **47**(3): 348-360.

Young, A. R., E. Y. Chan, et al. (2006). "Starvation and ULK1-dependent cycling of mammalian Atg9 between the TGN and endosomes." J Cell Sci **119**(Pt 18): 3888-3900.

Zeng, X., J. H. Overmeyer, et al. (2006). "Functional specificity of the mammalian Beclin-Vps34 PI 3-kinase complex in macroautophagy versus endocytosis and lysosomal enzyme trafficking." J Cell Sci **119**(Pt 2): 259-270.

Zhang, Z. Y. (2002). "Protein tyrosine phosphatases: structure and function, substrate specificity, and inhibitor development." Annu Rev Pharmacol Toxicol **42**: 209-234.

Zhong, Y., Q. J. Wang, et al. (2009). "Distinct regulation of autophagic activity by Atg14L and Rubicon associated with Beclin 1-phosphatidylinositol-3-kinase complex." Nat Cell Biol **11**(4): 468-476.